

**ANALYSIS OF COMPLEX BURSTING PATTERNS IN
MULTIPLE TIMESCALE RESPIRATORY NEURON
MODELS**

by

Yangyang Wang

B.S., Applied Mathematics, Beijing Normal University, 2010

Submitted to the Graduate Faculty of
the Kenneth P. Dietrich School of Arts and Sciences in partial
fulfillment

of the requirements for the degree of

Doctor of Philosophy

University of Pittsburgh

2016

UNIVERSITY OF PITTSBURGH
DIETRICH SCHOOL OF ARTS AND SCIENCES

This dissertation was presented

by

Yangyang Wang

It was defended on

May 3rd 2016

and approved by

Jonathan E. Rubin, Department of Mathematics

G. Bard Ermentrout, Department of Mathematics

Brent Doiron, Department of Mathematics

David M. Jasnow, Department of Physics and Astronomy

Dissertation Director: Jonathan E. Rubin, Department of Mathematics

ANALYSIS OF COMPLEX BURSTING PATTERNS IN MULTIPLE TIMESCALE RESPIRATORY NEURON MODELS

Yangyang Wang, PhD

University of Pittsburgh, 2016

Many physical systems feature interacting components that evolve on disparate timescales. Significant insights about the dynamics of such systems have resulted from grouping timescales into two classes and exploiting the timescale separation between classes through the use of geometric singular perturbation theory. It is natural to expect, however, that some dynamic phenomena cannot be captured by a two timescale decomposition. One example is the mixed burst firing mode, observed in both recordings and model pre-Bötzinger neurons, which appears to involve at least three timescales based on its time course. With this motivation, we construct a model system consisting of a pair of Morris-Lecar systems coupled so that there are three timescales in the full system. We demonstrate that the approach previously developed in the context of geometric singular perturbation theory for the analysis of two timescale systems extends naturally to the three timescale setting. To elucidate which characteristics truly represent three timescale features, we investigate certain reductions to two timescales and the parameter dependence of solution features in the three timescale framework. Furthermore, these analyses and methods are extended and applied to understand multiple timescale bursting dynamics in a realistic single pre-Bötzinger complex neuron and a heterogeneous population of these neurons, both of which can generate a novel mixed bursting (MB) solution, also observed in pre-BötC neuron recordings. Rather surprisingly, we discover that a third timescale is not actually required to generate mixed bursting solution in the single neuron model, whereas at least three timescales should be involved in the latter model to yield a similar mixed bursting pattern. Through our analysis of timescales, we also elucidate how the single pre-BötC neuron model can be tuned to improve the robustness of the MB solution.

Keywords: fast-slow systems, multiple timescales, oscillations, geometric singular perturbation theory, bursting, respiratory neuron, persistent sodium, calcium.

TABLE OF CONTENTS

PREFACE	xiii
1.0 INTRODUCTION	1
1.1 Generation of respiratory rhythms	1
1.2 Models of respiratory rhythm generation in the pre-BötC	2
1.3 geometric singular perturbation theory: fast/slow analysis	4
1.4 Outline	8
2.0 UNDERSTANDING AND DISTINGUISHING THREE TIME SCALE OSCIL-	
LATIONS: CASE STUDY IN A COUPLED MORRIS-LECAR SYSTEM	11
2.1 Preliminaries	15
2.1.1 Singular limits: scalings and subsystems	17
2.1.2 Effect of coupling	24
2.2 Analysis of three timescale solutions	28
2.2.1 Case 1: $g_{syn}=1.0$	29
2.2.1.1 (v_1, w_1) driven by (v_2, w_2)	29
2.2.2 Case 2: $g_{syn}=4.1$	32
2.2.2.1 (v_1, w_1) driven by (v_2, w_2)	32
2.2.3 Case 3: $g_{syn}=5.1$	36
2.2.3.1 (v_1, w_1) driven by (v_2, w_2)	36
2.3 Identifying three timescale features	38
2.3.1 $g_{syn} = 1.0$: recruitment of a transient V_1 spike	39
2.3.2 $g_{syn} = 4.1$: transition from V_1 spikes of gradually decaying amplitude to V_1 spikes of constant amplitude	42

2.3.3	$g_{syn} = 5.1$: direct transition to a depolarized plateau	45
2.4	Discussion	47
3.0	MULTIPLE TIMESCALE MIXED BURSTING DYNAMICS IN A RESPIRATORY NEURON MODEL	52
3.1	Analysis of the mixed bursting model	56
3.1.1	Rescaling and simplification of timescales	58
3.1.2	Dynamics of the constant- τ model (3.5)	61
3.1.3	Finding the combination of timescales that supports MB solutions in the constant- τ model (3.5)	65
3.1.3.1	(C1) \Rightarrow Analysis of timescales of v and n	65
3.1.3.2	(C2) and (C3) \Rightarrow Analysis of timescales of h , v_2 and w	69
3.1.4	Dynamics of the mixed bursting model (3.1)	72
3.2	Robustness of the mixed bursting model	75
3.2.1	Robustness to $[IP_3]$	75
3.2.2	Robustness to g_{NaP}	79
3.3	Discussion	83
4.0	MULTIPLE TIMESCALE SIGH-LIKE BURSTING IN A SELF-COUPLED PRE-BÖTC NEURON	86
4.1	Analysis of sigh-like bursting	91
4.1.1	Mechanisms underlying regular bursting	95
4.1.2	Mechanisms underlying the transition from regular bursts to the sigh-like burst	97
4.2	Identifying timescales	105
4.3	Discussion	107
5.0	CONCLUSIONS	111
5.1	Summary	111
5.2	When do we need three timescales?	113
5.3	Analysis of 3 timescale systems	114
6.0	APPENDIX	117
6.1	Nondimensionalization of the coupled Morris-Lecar system	117
6.2	Adjusting timescales in the dendritic subsystem	118

6.3 Nondimensionalization of the mixed bursting model	119
6.4 Nondimensionalization of the Jasinski model	123
BIBLIOGRAPHY	125

LIST OF TABLES

2.1	The values of the parameters in the model given by (2.1) and (2.2).	13
2.2	Subsystems for (2.4).	22
3.1	The values of the parameters in the pre-BötC model given by equations (3.1) and (3.2)	54
3.2	Timescales for the constant- τ model (3.5)	72
3.3	Time Scales of n and h	74
4.1	Ionic currents and channel reversal potentials	88
4.2	Activation and inactivation variables	88
4.3	Activation and inactivation variables	89
5.1	Subsystems for 3 timescale system.	115
6.1	The timescales for the Jasinski model.	124

LIST OF FIGURES

1.1	Schematic diagram showing construction of a singular periodic orbit by concatenation of solution segments for singular limit systems.	7
1.2	Typical fast/slow analysis (with h slow and V fast) for square-wave bursting.	9
2.1	Baseline phase planes for the two ML systems without coupling.	14
2.2	Time series for attracting solutions of (2.1)-(2.2) with parameter values as in Table 2.1 and with the indicated values of g_{syn}	16
2.3	Nullclines for v_1 (red) and w_1 (cyan) for the v_2 -frozen system (2.19).	25
2.4	Bifurcation diagrams for (2.19) with v_2 as a parameter.	25
2.5	Bifurcation curves for (2.19) in (v_2, g_{syn}) parameter space.	26
2.6	Graph of $S(v_2)$ (blue) and locus of the v_2 -nullcline (black/red).	27
2.7	Attracting dynamics in (v_2, w_2) -space.	28
2.8	An attracting solution of (2.4) for $g_{syn} = 1.0$ (black curve) projected to the (v_1, w_1) plane.	30
2.9	The attracting trajectory from Figure 2.8 (black curve) projected onto the (w_1, v_2) plane.	31
2.10	An attracting solution of (2.4) for $g_{syn} = 4.1$, projected to (v_1, w_1) -space (black curve).	34
2.11	Projection to the (w_1, v_2) -plane illuminates several features of the periodic solution (black) for $g_{syn} = 4.1$	35
2.12	An attracting solution of (2.4) for $g_{syn} = 5.1$, projected to (v_1, w_1) -space (black curve), together with nullclines for (2.19). Colours of curves are as in Figure 2.10.	36

2.13 Projection to the (w_1, v_2) plane illuminates several features of the periodic solution (black) for $g_{syn} = 5.1$	37
2.14 Projections of solutions for $g_{syn} = 1.0$ onto (V_1, V_2, w_2) -space.	39
2.15 Time series of rescaled versions of (2.1) with $g_{syn} = 1.0$	40
2.16 Time series of (2.1) with $g_{syn} = 4.1$	42
2.17 Time courses of V_2 (red) and V_1 (black/blue/green)	43
2.18 Projection of the attracting solution (black curve) of the (3S, 1SS) system with $g_{syn} = 4.1$, $C_1 = 80$, $\phi_2 = 0.0001$ onto (V_1, V_2, w_2) -space. Red curves denote \mathcal{M}_{ss} , and blue and green circles mark two folds of \mathcal{M}_{ss}	45
2.19 Time series of (2.1) with $g_{syn} = 5.1$	46
3.1 Basic structures of the two subsystems (3.1a)-(3.1c) and (3.1d)-(3.1e) with parameter values as given in Table 3.1 but without coupling.	54
3.2 Time series for bursting solutions of the full system (3.1)-(3.2).	56
3.3 Attracting dynamics in $([Ca], l)$ -space.	57
3.4 Functions (A) $1/\tau_n(V)$ and (B) $1/\tau_h(V)$. Note the difference in vertical scales between panels.	59
3.5 Simulation of the MB solution generated by (3.5), together with corresponding bifurcation diagrams.	62
3.6 Bifurcation diagrams for the somatic subsystem for various τ_n values.	66
3.7 Bifurcation curves for the (v, n) subsystem of (3.5) for $c = 0$	69
3.8 Time series for attracting solutions of the constant- τ model and associated bifurcation diagrams when $R_v = 1$, $R_n = 5$, $R_c = 10$, and $R_l = 1000$	71
3.9 The graphs of the functions $1/\tau_n(v)$ and $1/\tau_h(v)$, with both default and new choices of σ_n, a_n, σ_h and a_h	73
3.10 The bifurcation diagrams of the somatic subsystem corresponding to the modified forms of $\tau_n(v)$ as shown in Figure 3.9A, along with the h -nullcline (cyan). The other color codings are the same as in Figure 3.9A.	74
3.11 Time series for attracting solutions of (3.4) and corresponding bifurcation diagrams.	76
3.12 Regions of MB solutions for the mixed bursting model.	77

3.13 Time series of (3.4) with $C_m = 21$, $K_{Ca} = 1.25 \times 10^{-4}$, $A = 0.001$, $\sigma_n = -5$, $a_n = 0.1$, $\sigma_h = 7$ and $a_h = 0.001$	77
3.14 Projection of the two MB solutions (black) from Figure 3.13 to (c, l) -space.	79
3.15 Bifurcations of the dendritic subsystem.	80
3.16 The zoomed view of two-parameter bifurcation diagrams of HC (red), LF (blue) and the trajectory (black) from Figure 3.13, projected into $(h, g_{CAN_{tot}})$ -space.	81
3.17 Two curves of HC bifurcations and two overlapping curves of LF bifurcations, in $(h, g_{CAN_{Tot}})$ parameter space.	81
3.18 Effect of variations in g_{NaP} on the behaviors of the somatic subsystem.	82
3.19 Spiking/bursting and bursting/plateauing boundaries of the somatic subsystem.	83
4.1 Mixed bursting solution (A) and sigh-like bursting solution (B) from [80] and [30], respectively.	87
4.2 Simulation of sigh-like rhythmic bursting of the Jasinski model.	91
4.3 Basic structures of the voltage subsystem (4.1a)-(4.1d) and the calcium subsystem (4.1e)-(4.1g).	94
4.4 Bifurcation diagrams of the Fast system (4.1a)-(4.1c) with the slow variables Na_i and Ca_i taken as static parameters.	96
4.5 Effect of variations in Ca_{tot} on the trajectories of the fast-slow subsystem (V, y, Ca_i, Na_i) for $l = 0.94$	99
4.6 Averaged phase planes, corresponding to (4.2), with superimposed trajectories of the Fast-Slow system, for $l = 0.94$ and three different values of Ca_{tot} as in Figure 4.5.	101
4.7 Bifurcation diagram of the average slow system (4.2) with respect to Ca_{tot} with l fixed at 0.94.	102
4.8 Simulation of the SB solution generated by the Jasinski model (4.1), together with the bifurcation diagrams.	104
4.9 Rescaled version of (4.1): (9F, 2SS) case, with $\beta = 100$, $\alpha_{Na} = 5 \times 10^{-3}$	107
4.10 Rescaled version of (4.1): (7F, 4SS) case, with $\beta = 0.1$, $\alpha_{Na} = 5 \times 10^{-6}$	108
5.1 Frequency-power plot for V in the MB solution (A) and the SB solution (B).	113

6.1 Time series for attracting solutions of the full model (3.1) as well as the bifurcation structure of the dendritic subsystem with parameter values as in Table 3.1. 120

PREFACE

First of all, I would like to express my deepest gratitude to my advisor Dr. Jonathan Rubin for giving me the opportunity to join these exciting research projects. It is you who lead me to this wonderful world of mathematical neuroscience, and support me to attend conferences and to meet with collaborators and fellow researchers from all over the world. Also, thank you for bringing me to New Zealand where I not only made breakthrough in my research but also had the most precious memories in my life. This work would never be completed without your wisdom, your patience and your invaluable guidance through these past 5 years.

Besides, I would also like to express my sincerest gratitude to Bard Ermentrout, Brent Doiron and David Jasnou for serving on my committee and your valuable criticism and advices on shaping this thesis project; to Hinke Osinga and Bernd Krauskopf for inviting me to visit the University of Auckland to engage in research discussions on collaborative work in the area of multiple timescale dynamical systems, which inspired the contents of Chapter 2 of this thesis; to Vivien Kirk and Pingyu Nan for the wonderful collaboration I have had during my visit to the University of Auckland. I will never forget our weekly meeting during my three months' stay and how we worked together on the project in Chapter 2; to Theodore Vo and Kerry-Lyn Roberts for teaching me how to compute bifurcations and averaged nullclines using AUTO.

To my family, thank you for your love and support whenever I feel lost. Without you, none of my goals would have been achieved. Thank my fiance, Changqing Wang, for your accompany, encouragement and love. I am so grateful to have you as my partner in my life.

1.0 INTRODUCTION

1.1 GENERATION OF RESPIRATORY RHYTHMS

Breathing is an essential behavior regulating the oxygen and carbon dioxide in mammals, required to sustain life. The role of the brain in respiration was accepted in the early nineteenth century [37], which sets the basis for the investigations into the sites and mechanisms underlying the generation of respiratory rhythm. One of the earliest results, a classical lesion study on adult cat by Lumsden (1923) [38], suggested that the neurons in pons are part of the network controlling breathing. In the 1990s, several studies have suggested that breathing is controlled by a neural central pattern generator (CPG) consisting of groups of neurons in both pons and medulla regions. Many ponto-medullary respiratory network models have been developed for understanding the respiratory brain stem and connectivity between different brainstem compartments [16, 49, 66, 60]. The respiratory rhythm results from the interactions of neuronal populations distributed within the ventrolateral respiratory column (VRC) as well as neural populations in other brainstem regions including the pontine respiratory group (PRG) [1, 62]. The output of the brainstem respiratory network is then transmitted to motoneurons that drive the respiratory pump muscles located at the spinal cord, e.g., motoneurons that contract diaphragm such that the lung expands during inspiration. Recent experiment by [20] on brainstem of goat suggested that there is a clear difference in the role for different sites but all play an essential role in the control of breathing. Even after all these years of intensive investigations of the neural network related to respiratory system, the underlying mechanisms for breathing are still not fully understood and require much effort in the future.

One of the main characteristics of respiration is rhythmicity, and identifying the mechanism for rhythm generation is a very fundamental step in understanding the neural control of breathing. In 1991, the pre-Bötzinger complex (pre-BötC), a subregion of the ventrolateral medulla of the brain-

stem, has been firstly discovered by Smith et al to be the primary neuronal kernel for respiratory rhythm generation [65]. Pacemaker neurons with intrinsic bursting properties have been identified in this region. In total, there exist two distinct types of intrinsically bursting cells in terms of different underlying ionic mechanisms in pre-BötC. The first is voltage-dependent [65] and based on the persistent (fast activating and slowly inactivating) Na^+ current (I_{NaP}) in neurons [7, 8]. The presence of I_{NaP} has been confirmed [44, 43, 22], and pharmacologically blocking I_{NaP} could silence the pre-BötC rhythmic activity in medullary slices from neonatal rats [61, 22]. Alternatively, another type of pacemaker has also been identified [72] and the underlying mechanism depends on a Ca^{2+} -activated nonspecific cationic current (I_{CAN}) [46].

The demonstration that respiratory-related rhythmic activity in the *in vitro* slice and *en bloc* preparations persists after the blockade of synaptic inhibition [11, 17, 50, 63] leads to the hypothesis that rhythmogenesis results from neurons with pacemaker-like properties. However, the respiratory CPG, the pre-BötC, still exhibits respiratory rhythmicity after stopping the bursting behaviour in both population of I_{NaP} and I_{CAN} pacemaker neurons simultaneously [45, 43, 16, 43]. It is therefore suggested that bursting-pacemaker neurons are not essential for respiratory rhythmogenesis. Alternatively, a group-pacemaker has been proposed as the fundamental unit for respiratory rhythmogenesis: burst rhythms originate from recurrent synaptic excitation that combine with neurons with intrinsic pacemaker properties [51].

1.2 MODELS OF RESPIRATORY RHYTHM GENERATION IN THE PRE-BÖTC

The rhythmic respiratory pattern is complex, even at single neuron level. To describe the behavior of individual respiratory neurons, Butera et al. [7, 8] developed and analyzed computational models for individual bursting pacemaker neurons in the pre-BötC as well as heterogeneous populations of these neurons with mutual excitatory synaptic connections. Two minimal models have been proposed using a Hodgkin-Huxley like formalism, and in the first one, the rhythmic bursting arises from the persistent (slowly inactivating) Na^+ current (I_{NaP}). This model matches many experimentally observed properties of pre-BötC neurons. For instance, it has various voltage-dependent activity states: quiescence at hyperpolarized membrane voltages when I_{NaP} is not activated, burst-

ing when I_{NaP} alternates between activation and inactivation, and tonic spiking activity at more depolarized voltages where I_{NaP} is essentially inactivated. This single cell neuron model has been widely adopted and used in extensive modeling studies investigating behavior of heterogeneous excitatory networks of intrinsically and non-intrinsically bursting neurons as a basic model for the pre-BötC excitatory network [7, 8, 42, 58, 49].

Recall that a Ca^{2+} -activated nonspecific cationic current (I_{CAN}) is also involved in bursting generated in the pre-BötC neurons. A computational model of bursting activity based on I_{CAN} was proposed by Rubin et al. [56] based on the group pacemaker hypothesis for inspiratory rhythm generation, as described before. The role of synaptic mechanisms and network interactions in generating emergent network rhythms (which cannot be generated by single neurons) has been emphasized. In this group pacemaker model, the activation of I_{CAN} due to Ca^{2+} accumulation triggered by recurrent synaptic excitation initiates a network-wide burst, the termination of which is relying on transient Na^+ current-dependent spike inactivation and the activation of outward currents, rather than on I_{NaP} inactivation.

By combining together these two intrinsic Na^+ - and Ca^{2+} -dependent mechanisms for single-neuron bursting, Toporikova and Butera [73] have proposed a two-compartment (somatic-dendritic) model (TB model) of an isolated pre-BötC neuron incorporating I_{NaP} and I_{CAN} as two independent bursting mechanisms. Bursting in the somatic compartment is produced by I_{NaP} as in Butera et al. model [7, 8], whereas bursting in the dendritic compartment is based on Ca^{2+} oscillations.

Intracellular Ca^{2+} in the TB model is confined to a dendritic compartment. Since neurons in the pre-BötC appear to be electronically compact [14], [42], and the model generates qualitatively similar dynamics when reduced to a single compartment, Park and Rubin [47] used such a reduction and studied a single-compartment model (PR model) of a pre-BötC inspiratory neuron featuring both NaP and CAN currents, as well as intracellular calcium oscillations that activate the CAN current.

In both TB and PR models, the two intrinsic bursting mechanisms could coexist and interact to generate a hybrid bursting pattern. Interestingly, a novel mixed bursting (MB) solution, which appears to involve at least three timescales based on its time course, results from the interaction of these two mechanisms [47]. Such irregular bursting patterns have also been observed in other realistic biological models and in recordings from respiratory CPG neurons as well as subthalamic

nucleus (STN) neurons in the basal ganglia (e.g. [3], [30], [14]). While [47] presented a mathematical analysis explaining relevant bursting mechanisms, based on the NaP current, the CAN current, or both currents working together, less analysis about mixed bursting patterns was provided and little consideration was given to identifying how many timescales are truly required to obtain these solutions or to their robustness. Similar MB solution patterns were also recently observed in a heterogeneous population of pre-BötC neurons by Jasinski et al. [30].

Many physical quantities have characteristic rates at which they tend to evolve. Identifying relevant timescales is a useful step in modeling physical systems using any sort of dynamic framework. In mathematical analysis in particular, the timescales in a system of differential equations are often grouped into a small number of classes, so that limits can be taken and the assumptions of certain mathematical techniques can be satisfied; the aim is to use knowledge of the limit system(s) to gain information about behaviour of the original system. Examples of this approach are ubiquitous in the literature, with ideas applicable to systems in which timescales can be grouped into two classes being particularly well developed. However, there have been fewer reported studies that analyze dynamics involving evolution on three distinct timescales. Even fewer works have examined decisions about how to group timescales (for example, whether to use two or three classes), a decision that can arise both in the mathematical treatment of model systems and in the development of mathematical models based on experimental observations. Our goal in this thesis is to do both of these things, with a focus on a certain minimal model system in Chapter 2, a single pre-BötC neuron model in Chapter 3, and an excitatory neural network of the pre-BötC neurons in Chapter 4.

1.3 GEOMETRIC SINGULAR PERTURBATION THEORY: FAST/SLOW ANALYSIS

We first review the regular bursting phenomenon from a mathematical viewpoint. The dynamics of bursting is characterized by the coexistence of oscillatory and non-oscillatory attractors, alternating between periods of rapid oscillations and slow silent phase of near steady state resting behavior. The underlying mathematical structures for bursting phenomena involving multiple timescales are dynamical systems that are often singularly perturbed [28, 33, 10]:

$$(1.1a) \quad \frac{dx}{dt} = f(x, y, \varepsilon)$$

$$(1.1b) \quad \frac{dy}{dt} = \varepsilon g(x, y, \varepsilon),$$

where $x \in \mathbb{R}^m$ is fast, $y \in \mathbb{R}^n$ is slow, t is the fast time, $0 < \varepsilon \ll 1$ is a small perturbation parameter. The functions f and g are both assumed to be sufficiently smooth.

One technique that has been used to deal with such fast/slow system with great success is geometric singular perturbation theory (GSPT) [19, 31], which is the main tool used in this thesis. Hence, we briefly review the theoretical framework of the geometric singular perturbations approach.

A time rescaling $t = \tau/\varepsilon$ gives an equivalent system

$$(1.2a) \quad \varepsilon \frac{dx}{d\tau} = f(x, y, \varepsilon)$$

$$(1.2b) \quad \frac{dy}{d\tau} = g(x, y, \varepsilon),$$

where τ is the slow time. (1.1) and (1.2) share the same trajectory paths except evolve at different rates. The system (1.1) can be decomposed into fast and slow subsystems by taking the singular limit $\varepsilon \rightarrow 0$ on the slow and fast timescales, respectively, because of which we also denote them as singular limit systems. The nature of oscillations in the full system can then be understood by concatenating solution segments of singular limit systems. Specifically, taking $\varepsilon \rightarrow 0$ in (1.1) gives the m -dimensional system called the *layer problem* (or *fast subsystem*)

$$(1.3a) \quad \frac{dx}{dt} = f(x, y, 0)$$

$$(1.3b) \quad \frac{dy}{dt} = 0,$$

where the variable x will vary over a fast timescale while y will remain constant. Alternatively, the singular limit $\varepsilon \rightarrow 0$ in (1.2) gives the n -dimensional differential-algebraic system called the *reduced system* (or *slow subsystem*)

$$(1.4a) \quad 0 = f(x, y, 0)$$

$$(1.4b) \quad \frac{dy}{d\tau} = g(x, y, \varepsilon),$$

in which the variable y evolves on a slow timescale subject to the constraint $f(x, y, 0) = 0$, the first equation in (1.4). The dynamics of the full system (1.1) can then be understood by studying the two lower-dimensional subproblems (1.3) and (1.4), which makes GSPT a powerful tool for analyzing high dimensional systems.

GSPT starts with a bifurcation analysis of the layer problem (1.3). The set of equilibria of the layer problem is usually referred to as the *critical manifold*

$$(1.5a) \quad \mathcal{M}_s := \{(x, y) \in \mathbb{R}^m \times \mathbb{R}^n : f(x, y, 0) = 0\}.$$

\mathcal{M}_s is, at least locally, an n -dimensional manifold since it is formed by solving m equations in \mathbb{R}^{m+n} . Indeed, it is natural to expect it to have a parametrization by the variable y . A subset \mathcal{M}_{s0} of \mathcal{M}_s is defined to be *normally hyperbolic* if all $(x, y) \in \mathcal{M}_{s0}$ are hyperbolic equilibria of the layer problem, i.e., the Jacobian matrix of f evaluated at each point in \mathcal{M}_{s0} ($D_x f|_{\mathcal{M}_{s0}}$) has no eigenvalues with zero real part. The stability of the normally hyperbolic subset contained in \mathcal{M}_s as equilibria of the layer problem is as following:

1. $\mathcal{M}_{sa} \subset \mathcal{M}_s$ is attracting if all eigenvalues of $D_x f$ have negative real part for $(x, y) \in \mathcal{M}_{sa}$;
2. $\mathcal{M}_{sr} \subset \mathcal{M}_s$ is repelling if all eigenvalues of $D_x f$ have positive real part for $(x, y) \in \mathcal{M}_{sr}$;
3. Otherwise, the subset of \mathcal{M}_s is of saddle type.

Fenichel theory [19, 31] guarantees that normally hyperbolic invariant manifolds of equilibria of the layer problem (1.3) perturb to a locally invariant slow manifold $\mathcal{M}_s^\varepsilon$ of the full system (1.1) for ε sufficiently small. The restriction of the flow to $\mathcal{M}_s^\varepsilon$ is an $O(\varepsilon)$ -perturbation of the slow flow along \mathcal{M}_s described by the reduced problem. Therefore, we can use reduced and layer flows to construct singular periodic orbits, which according to Fenichel theory, perturb to a nearby periodic orbit. To illustrate, we start with the construction of the simplest type of periodic solution: a relaxation oscillation. Within a two timescale setting and for a system with a cubic-shaped critical manifold, one might be able to construct a singular closed orbit by concatenating in order a solution of the (fast) layer problem, a solution of the (slow) reduced problem, a second solution of the layer problem, and a second solution of the reduced problem, as illustrated in Fig. 1.1. Then, depending on the details of the dynamics and the structure of the critical manifold where the connections between the slow and fast segments occur, such a singular oscillation will generically perturb, as

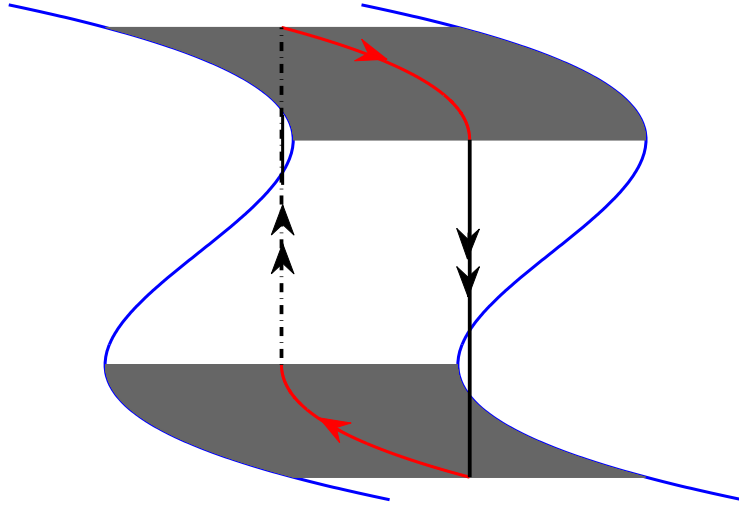


Figure 1.1: Schematic diagram showing construction of a singular periodic orbit by concatenation of solution segments for singular limit systems. The cubic-shaped surface is the critical manifold, \mathcal{M}_s . Solution segments shown in black, corresponding to the fast layer problem, jump between sheets of the critical manifold. Solution segments shown in red, coming from the slow reduced problem, lie on the critical manifold.

we move away from the singular limit, to a periodic solution of the full problem. In this manner, one is able to use the singular limit systems to understand the nature of oscillations in the full system. Further details of the method appear elsewhere (e.g., [31, 13]).

In this two timescale context, a crucial step in determining the nature of the solution that arises from a perturbation of a singular periodic orbit is to establish the type of points that occur at the transitions from slow to fast segments of the singular orbit when these occur on fold curves, where Fenichel theory breaks down due to the loss of normal hyperbolicity. Two types of point are commonly seen: *jump points* and *folded singularities* [13]. Singular orbits containing only jump points

perturb in a straightforward way to orbits that transition smoothly from slow to fast motion near the jump points, such as relaxation oscillations. However, singular orbits containing folded singularities may perturb to more complicated oscillations, including orbits with subthreshold oscillations such as mixed-mode oscillations [13].

The traditional implementation of GSPT in bursting models was pioneered by [52]. The dynamics of this perturbed problem (1.1) can be understood by considering the bifurcation structure of this fast subsystem as y varies slowly, a standard approach described, for example, [53, 57]. We also refer to such a GSPT approach as a *fast/slow* analysis. Different classes of burst patterns are distinguished by the mechanisms by which the bursting trajectories switch between the silent and active phase ([53, 26]). More specifically, the classification of bursting is determined by two crucial bifurcations of the fast subsystem associated with the initiation (resp., termination) of the active phase: the bifurcation of equilibria (resp., limit cycles) of (1.3) results in a transition behavior to oscillation branches (resp., steady state). Figure 1.2 shows the projection of the square-wave bursting onto the corresponding bifurcation diagram. This burst initiates at a saddle-node bifurcation (SN) and terminates at a homoclinic (HC) bifurcation.

1.4 OUTLINE

An important feature of most biological rhythms is that they evolve on different timescales. This thesis is mainly about understanding the genesis of complex patterns and rhythms involving multiple timescales in the neuronal systems, using tools from dynamical systems including GSPT, bifurcation analysis and phase plane analysis.

Applications of GSPT to analyze dynamical systems with two timescales are ubiquitous and well developed. However, there have been fewer reported studies that analyze dynamics involving evolution on three distinct timescales. It is natural to expect that some dynamic phenomena cannot be captured by a two timescale decomposition. One example is the mixed burst firing mode that we mentioned before. Therefore, our goals here are to generalize methods developed for two timescale systems to three timescale settings; to identify how many timescales are involved in solution features; and to improve the robustness of solutions of interest through our analysis of

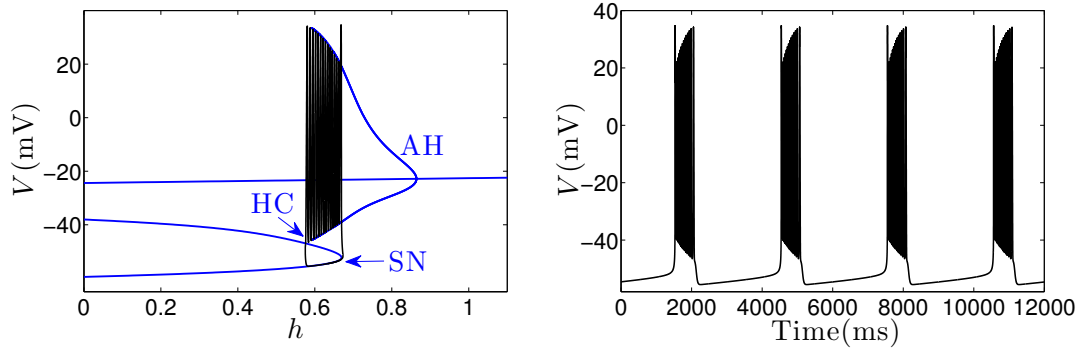


Figure 1.2: Typical fast/slow analysis (with h slow and V fast) for square-wave bursting. Left panel: The fast subsystem equilibria undergoes a supercritical Andronov-Hopf (AH) bifurcation. The family of periodics of (1.3) is formed in the AH bifurcation and terminated in a homoclinic (HC) bifurcation. The bursting, the active phase of which initiates at the lower fold (SN), closely follows stable limit cycles of (1.3) until the HC. Right panel: Time series for the square-wave bursting solution.

timescales.

The outline of the thesis is as follows: Motivated by efforts to understand irregular mixed bursting (MB) dynamics observed in both recordings and model pre-BötC neurons [47, 30, 14], in Chapter 2, we construct a minimal model system consisting of a pair of Morris-Lecar systems coupled so that there are three timescales in the full system. We generalize approaches previously developed in the context of geometric singular perturbation theory for the analysis of two timescale systems to the three timescale setting. By comparison with certain two timescale versions of the same system including solutions, bifurcations and phase planes, we investigate how many timescales are required for some solution properties. In Chapter 3, we extend the methods and analysis developed in Chapter 2 to understand the mechanisms underlying the MB pattern identified in [47]. Since a regular bursting solution requires at least two timescales, as discussed in Section 1.3, we then expect that MB solution involving a temporal progression of bursts might need a third timescale. We propose three conditions which together support mixed bursting solutions,

based on which we obtain a non-intuitive result that the MB solution is in fact, at its simplest, a two-timescale phenomenon rather than requiring three timescales. Through our analysis of timescale, we elucidate how the pre-BötC neuron model can be tuned to improve the robustness of the MB solution. In Chapter 4, we turn to sigh-like bursting (SB) solutions (with similar MB patterns) produced by a self-coupled preBötC neuron described by more detailed model in the pre-BötC [30], as a reduction of a coupled network. We investigate the possible roles of synaptic interactions, the two intrinsic bursting mechanisms (I_{CAN} -dependent, I_{NaP} -dependent), and the Na^+/K^+ pump (as suggested in [56]) in this network rhythmic bursting. In contrast to models studied in Chapter 2 and 3, the slow variable in the Jasiniski model receives input from V (fast) and hence exhibits small oscillations during the spiking phase of a burst, due to which averaging is required. We identify bifurcations corresponding to transitions between regular bursts and the long burst that corresponds to the sigh, and the onset of the slow jump in calcium concentration, respectively. Similarly as in the previous two chapters, an analysis about timescales is provided. We conclude in Chapter 5 with a summary and discussion of the main results of the thesis, and possible future directions.

2.0 UNDERSTANDING AND DISTINGUISHING THREE TIME SCALE OSCILLATIONS: CASE STUDY IN A COUPLED MORRIS-LECAR SYSTEM¹

This work was originally motivated by efforts to understand oscillatory dynamics in neurons. It is well established that neural processes can evolve over very different timescales. For instance, the membrane potential of a neuron typically oscillates with a period on the order of milliseconds in response to opening and closing of ion channels in the membrane [15]. The ion channels, in turn, may have conductances that are modulated by much slower variations in the concentration of cytoplasmic calcium (Ca^{2+}) ions. Typical simple models of membrane potential oscillations (ignoring conductance modulation by Ca^{2+}) have at least two timescales [27], as do typical simple models of oscillations in intracellular Ca^{2+} [33], and thus models that combine these two processes typically involve three or more timescales. These combined models can have highly complicated solutions [47], and one challenge is to determine the mathematical mechanisms underlying the dynamics. We are particularly interested in knowing how much of the complication results from the presence of three or more timescales in the model and how much is, rather, a reflection of the models being relatively high dimensional nonlinear systems with many parameters.

As a first step in addressing such issues, we adopt the approach of constructing and analysing a minimal model that has three timescales explicitly built into it. This approach shares some similarities with that taken in [9, 76, 35], but we focus on some different aspects of solutions and their timescale dependence; a detailed discussion of the similarities and differences is in §5. We start with two copies of the Morris-Lecar (ML) equations [40, 54] and couple them in a simple way. The ML equations are a two-dimensional system of ordinary differential equations often

¹THIS CHAPTER IS BASED ON PUBLISHED WORK: P. NAN, Y. WANG, V. KIRK, AND J. RUBIN, UNDERSTANDING AND DISTINGUISHING THREE TIMESCALE OSCILLATIONS, SIAM JOURNAL ON APPLIED DYNAMICAL SYSTEMS, 14(3), 1518-1557, 2015.

used as a simple qualitative model of membrane potential oscillations; one of the variables of the model represents the membrane potential and the other represents inactivation of a family of ion channels in the membrane. With typical parameter values, the model has two timescales, with the membrane potential evolving much faster than the state of the ion channels. We choose to couple two copies of the two-dimensional model, not because we believe that the system so obtained is a physiologically accurate model of neuronal dynamics, but because it gives us a model where we can easily control the timescales; since the dynamics of a single ML oscillator is relatively well understood [54, 74], we can use the coupled system to investigate which features of the dynamics arise directly from the timescale structure of the model.

Our coupled ML system takes the form

$$(2.1a) \quad C_1 \frac{dV_1}{dt} = I_1 - g_{Ca} m_\infty(V_1)(V_1 - V_{Ca}) - g_K w_1(V_1 - V_K) - g_L(V_1 - V_L) - g_{syn} S(V_2)(V_1 - V_{syn})$$

$$(2.1b) \quad \frac{dw_1}{dt} = \phi_1(w_\infty(V_1) - w_1)/\tau_w(V_1)$$

$$(2.1c) \quad C_2 \frac{dV_2}{dt} = I_2 - g_{Ca} m_\infty(V_2)(V_2 - V_{Ca}) - g_K w_2(V_2 - V_K) - g_L(V_2 - V_L)$$

$$(2.1d) \quad \frac{dw_2}{dt} = \phi_2(w_\infty(V_2) - w_2)/\tau_w(V_2),$$

with

$$(2.2a) \quad S(V_i) = \alpha(V_i)/(\alpha(V_i) + \beta)$$

$$(2.2b) \quad \alpha(V_i) = 1/(1 + \exp(-(V_i - \theta_s)/\sigma_s))$$

$$(2.2c) \quad m_\infty(V_i) = 0.5(1 + \tanh((V_i - K_1)/K_2))$$

$$(2.2d) \quad w_\infty(V_i) = 0.5(1 + \tanh((V_i - K_3)/K_4))$$

$$(2.2e) \quad \tau_w(V_i) = 1/\cosh((V_i - K_3)/2K_4),$$

where $i = 1, 2$. The parameter g_{syn} controls the coupling between the two oscillators, which we choose for simplicity to be unidirectional such that the dynamics of (V_2, w_2) affects the dynamics of (V_1, w_1) but not vice versa; we refer to $S(V_2)$ as the coupling function. Several values of g_{syn} , with units of mS/cm^2 , will be considered, while other parameters will be fixed at the values shown

Table 2.1: The values of the parameters in the model given by (2.1) and (2.2).

Parameter values					
C_1	$8 \mu\text{F}/\text{cm}^2$	I_1	$0 \mu\text{A}/\text{cm}^2$	ϕ_1	0.01
C_2	$100 \mu\text{F}/\text{cm}^2$	I_2	$60 \mu\text{A}/\text{cm}^2$	ϕ_2	0.001
V_{Ca}	120 mV	g_{Ca}	$4 \text{ mS}/\text{cm}^2$	K_1	-1.2 mV
V_{K}	-84 mV	g_{K}	$8 \text{ mS}/\text{cm}^2$	K_2	18 mV
V_{L}	-60 mV	g_{L}	$2 \text{ mS}/\text{cm}^2$	K_3	12 mV
V_{syn}	30 mV	θ_s	-20 mV	K_4	17.4 mV
β	0.5 ms^{-1}	σ_s	10 mV		

in Table 2.1, selected so that there is clear separation of timescales between V_i (fast) and w_i (slow) in each oscillator and so that w_1 and V_2 evolve at comparable rates. In a more biologically realistic model for calcium and voltage interactions, V_1 might represent membrane potential and V_2 intracellular calcium concentration, and the physical units of some parameters in Table 2.1 and details of some terms in the model would need to be altered correspondingly. We work with (2.1)-(2.2) and the units in Table 2.1 nonetheless, since they provide the appropriate minimal mathematical structure (cf. [9, 76]) and these are the traditional units for the ML system.

In the absence of coupling, each ML oscillator can be tuned to be excitable, with an attracting critical point at relatively low V , or oscillatory, with an attracting limit cycle solution. A transition between these states can be induced by increasing the parameter I_i in the V_i -equation and typically occurs through a saddle node on an invariant circle (SNIC) or an Andronov-Hopf (AH) bifurcation, respectively called a Type I or Type II transition [54]. The specific parameters in Table 2.1 would yield a Type I transition if I_1 or I_2 were varied, but we keep I_1 and I_2 fixed at values such that when $g_{\text{syn}} = 0$, the (V_1, w_1) system is excitable and the (V_2, w_2) system is oscillatory (Figure 2.1). In this regime, (2.1)-(2.2) has the structure of an intrinsic oscillator, such as intracellular calcium oscillations, driving a conditional oscillator, such as calcium-dependent neuronal membrane potential oscillations. A similar structure was considered in the context of neurosecretory dynamics in [35]. In that work, a slower relaxation oscillation also provided input to a faster conditional oscillator, switching it between excitable and oscillatory states. Importantly, however, the coupling term in that work appeared in the equation for the slow recovery variable (analogous to w_1 in our notation), a difference that results in some qualitatively different dynamical effects, as we will discuss further

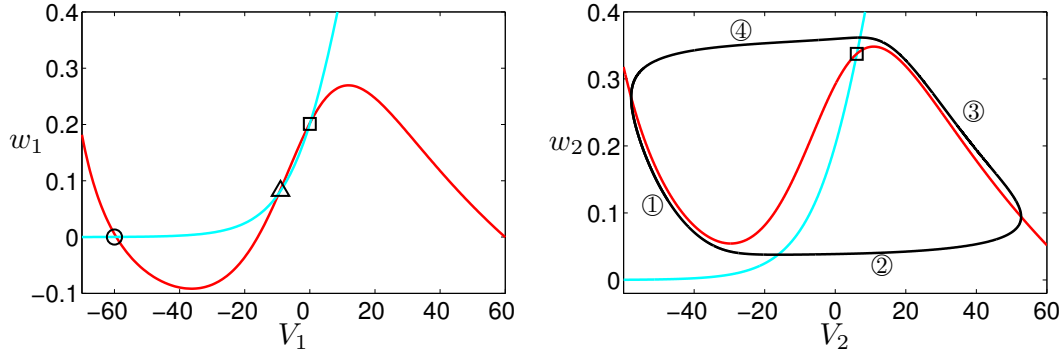


Figure 2.1: Baseline phase planes for the two ML systems without coupling. In each plot, the red curve is the V -nullcline and the cyan is the w -nullcline. The hollow circles, triangles, and squares denote equilibrium solutions of sink, saddle, and source type, respectively. The (V_1, w_1) system lacks a periodic solution, while the attracting periodic orbit for the (V_2, w_2) system is shown in black (with counterclockwise flow passing through the numbered regions in increasing order).

in §5.

The work in this chapter is part of a collaboration with V. Kirk and P. Nan [41]. We first explain the mechanisms underlying the dynamics of our model system. In doing so, we consider two viewpoints within the realm of geometric singular perturbation theory (GSPT). In one, we establish the roles of critical and superslow manifolds, within the four-dimensional model phase space, in shaping model dynamics, making heavy use of projections to three dimensions. In the other viewpoint, we link various two-dimensional projections, corresponding either to the phase plane of one ML system or to the slow subsystem of the model, as has often been useful in past studies of the dynamics of synaptically coupled neurons (e.g., [67, 71, 4, 57]). Notation and other preliminaries relating to these approaches are presented in Section 3.1.1 and the Appendix 6.1. The system that we study progresses through a variety of oscillatory solutions as the coupling strength g_{syn} is increased. We focus on certain key aspects appearing in the dynamics for three particular values of g_{syn} – the onset of oscillations in the conditional oscillator, the emergence of sustained oscillations, the modulation of oscillation amplitude, and the convergence to an elevated plateau –

such that patterns arising for other g_{syn} can be readily understood in terms of these components. The mechanisms underlying these phenomena are analyzed using our two approaches in Section 2.2. Next, in Section 2.3, we revisit the solution types and elucidate which characteristics truly represent three timescale features. This analysis involves consideration of certain reductions to two timescales as well as additional analysis of the parameter dependence of solution features in the three timescale framework. Our results in this area may be useful for characterizing, developing models of, and analyzing models of experimental data. Finally, Section 2.4 contains a discussion of our results.

2.1 PRELIMINARIES

Based on simulations of (2.1)-(2.2) over a range of g_{syn} values, we have selected three fundamental solution types on which to focus our analysis, specifically those obtained by setting g_{syn} to 1.0, 4.1 and 5.1. Time series for the attracting solutions at these values of g_{syn} are shown in Fig. 2.2. We shall see that the properties of these solutions are indicative of the presence of at least three timescales.

Our methods for analysis of the model will depend heavily on exploiting the presence of different timescales. As a first step in the analysis, therefore, it is helpful to rescale the variables so that the important timescales can be explicitly identified. To this end, we define new dimensionless variables (v_1, v_2, τ) , and voltage and timescales Q_v and Q_t , respectively, such that

$$(2.3) \quad V_1 = Q_v \cdot v_1, \quad V_2 = Q_v \cdot v_2, \quad t = Q_t \cdot \tau.$$

Note that w_1 and w_2 are already dimensionless in (2.1a-2.1d).

Details of the nondimensionalization procedure, including determination of appropriate values for Q_v and Q_t , are given in the Appendix. From this process, we obtain a dimensionless system of

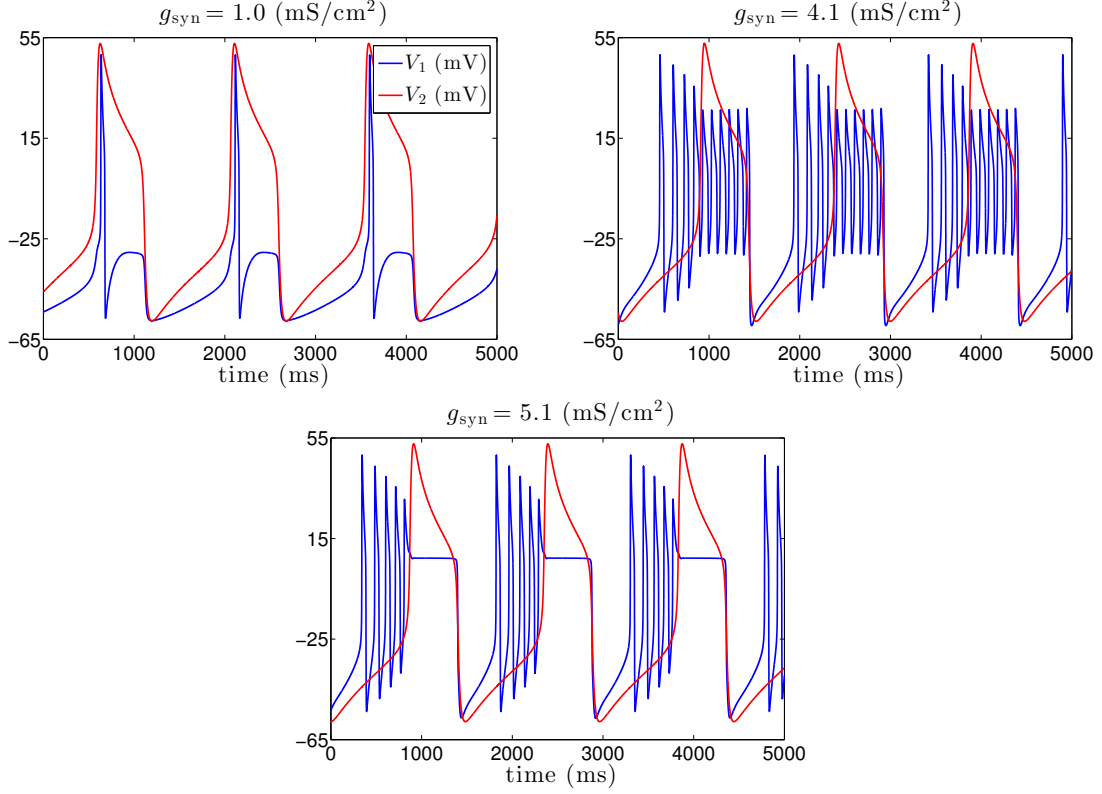


Figure 2.2: Time series for attracting solutions of (2.1)-(2.2) with parameter values as in Table 2.1 and with the indicated values of g_{syn} .

the form

$$(2.4a) \quad \varepsilon_1 \frac{dv_1}{d\tau} = f_1(v_1, v_2, w_1)$$

$$(2.4b) \quad \frac{dw_1}{d\tau} = g_1(v_1, w_1)$$

$$(2.4c) \quad \frac{dv_2}{d\tau} = f_2(v_2, w_2)$$

$$(2.4d) \quad \frac{dw_2}{d\tau} = \varepsilon_2 g_2(v_2, w_2),$$

with small parameters $\varepsilon_1, \varepsilon_2 \ll 1$, where the functions f_1, f_2, g_1 and g_2 are specified in (6.3) in the Appendix. The values of ε_1 and ε_2 can be varied by changing C_1 and ϕ_2 , respectively, as shown in (6.2a); the parameter values given in Table 2.1 yield $\varepsilon_1 = 0.1, \varepsilon_2 = 0.053$.

2.1.1 Singular limits: scalings and subsystems

Standard ideas from GSPT [18, 31, 32] are useful in our analysis, although they need to be adapted to allow for the presence of three timescales in our model. Rewriting the time variable τ as t_s , we see that (2.4) has the form

$$(2.5a) \quad \varepsilon_1 \frac{dv_1}{dt_s} = f_1(v_1, v_2, w_1)$$

$$(2.5b) \quad \frac{dw_1}{dt_s} = g_1(v_1, w_1)$$

$$(2.5c) \quad \frac{dv_2}{dt_s} = f_2(v_2, w_2)$$

$$(2.5d) \quad \frac{dw_2}{dt_s} = \varepsilon_2 g_2(v_2, w_2),$$

where f_1, g_1, f_2, g_2 are $O(1)$ functions and $\varepsilon_1, \varepsilon_2$ are small parameters. We refer to changes with respect to t_s as evolution on the *slow timescale*. Introducing a superslow time $t_{ss} = \varepsilon_2 t_s$, which changes slowly relative to t_s , we can derive the rescaled system

$$(2.6a) \quad \varepsilon_1 \varepsilon_2 \frac{dv_1}{dt_{ss}} = f_1(v_1, v_2, w_1)$$

$$(2.6b) \quad \varepsilon_2 \frac{dw_1}{dt_{ss}} = g_1(v_1, w_1)$$

$$(2.6c) \quad \varepsilon_2 \frac{dv_2}{dt_{ss}} = f_2(v_2, w_2)$$

$$(2.6d) \quad \frac{dw_2}{dt_{ss}} = g_2(v_2, w_2),$$

which evolves on the *superslow timescale*. Alternatively, defining a fast time $t_f = t_s/\varepsilon_1$, which changes quickly relative to t_s , we obtain the rescaled system

$$(2.7a) \quad \frac{dv_1}{dt_f} = f_1(v_1, v_2, w_1)$$

$$(2.7b) \quad \frac{dw_1}{dt_f} = \varepsilon_1 g_1(v_1, w_1)$$

$$(2.7c) \quad \frac{dv_2}{dt_f} = \varepsilon_1 f_2(v_2, w_2)$$

$$(2.7d) \quad \frac{dw_2}{dt_f} = \varepsilon_1 \varepsilon_2 g_2(v_2, w_2),$$

which evolves on the *fast timescale*.

There are several possible singular limits that can be taken in (2.5)-(2.7), yielding an array of subsystems. We will use the term *reduced problem* to refer to a subsystem that is exposed by a limit that eliminates dynamics faster than the baseline timescale. The phrase *layer problem* will refer to a system obtained by eliminating dynamics slower than the baseline. Since a reduced problem may have more than one timescale, we can define a layer problem for a reduced problem, and we will refer to the resulting system as a *reduced layer problem*. These terms will become clearer as we apply them to specific systems below.

Fixing $\varepsilon_2 > 0$ and taking $\varepsilon_1 \rightarrow 0$ in (2.7) yields a system that describes the dynamics of the fast variable, v_1 , for fixed values of the other variables,

$$(2.8) \quad \frac{dv_1}{dt_f} = f_1(v_1, w_1, v_2).$$

We call this limit the *fast layer problem*, and refer to the corresponding dynamics as the *fast flow*. We define the critical manifold \mathcal{M}_s to be the manifold of equilibrium points of the fast layer problem, i.e.,

$$(2.9) \quad \mathcal{M}_s := \{(v_1, v_2, w_1, w_2) : f_1(v_1, v_2, w_1) = 0\}.$$

Although \mathcal{M}_s is a three-dimensional manifold in (v_1, w_1, v_2, w_2) space, it does not depend on w_2 . We can solve $f_1(v_1, v_2, w_1) = 0$ for w_1 as a function of v_1 and v_2 and can therefore represent \mathcal{M}_s as

$$(2.10) \quad w_1 = F_1(v_1, v_2)$$

for a function F_1 . This relation allows us to readily visualize the projection of \mathcal{M}_s onto (v_1, v_2, w_1) -space. It is well known as we discussed in Chapter 1 [18] that, for sufficiently small $\varepsilon_1 > 0$, normally hyperbolic parts of \mathcal{M}_s each perturb to a locally invariant manifold called a *slow manifold*, on which w_1 is given by an $O(\varepsilon_1)$ -perturbation of F_1 ; we simply use \mathcal{M}_s as a convenient numerical approximation of these slow manifolds.

Taking the same limit, i.e., $\varepsilon_1 \rightarrow 0$ with $\varepsilon_2 > 0$, in (2.5) yields a system that describes the dynamics of w_1, v_2, w_2 restricted to the surface \mathcal{M}_s ,

$$(2.11a) \quad \frac{dw_1}{dt_s} = g_1(v_1, w_1),$$

$$(2.11b) \quad \frac{dv_2}{dt_s} = f_2(v_2, w_2),$$

$$(2.11c) \quad \frac{dw_2}{dt_s} = \varepsilon_2 g_2(v_2, w_2),$$

subject to the constraint $f_1(v_1, v_2, w_1) = 0$. Since it is obtained by eliminating the fast flow, we call this system the *slow reduced problem*. It is itself a multiple timescale problem, since the slow and superslow timescales are still both present. It is convenient to further separate scales by letting $\varepsilon_2 \rightarrow 0$ in (2.11); doing so yields the *slow reduced layer problem*,

$$(2.12a) \quad \frac{dw_1}{dt_s} = g_1(v_1, w_1),$$

$$(2.12b) \quad \frac{dv_2}{dt_s} = f_2(v_2, w_2),$$

which describes the dynamics of the slow variables w_1 and v_2 for fixed values of w_2 , with all variables restricted to \mathcal{M}_s . Since it takes place entirely on the slow timescale, we refer to the corresponding dynamics as the *slow flow*.

Alternatively, fixing $\varepsilon_1 > 0$ and taking $\varepsilon_2 \rightarrow 0$ in (2.5) or (2.7) yields the *slow layer problem*, which is a different layer problem from (2.12). Starting from (2.5) yields the slow layer problem in the form

$$(2.13a) \quad \varepsilon_1 \frac{dv_1}{dt_s} = f_1(v_1, v_2, w_1),$$

$$(2.13b) \quad \frac{dw_1}{dt_s} = g_1(v_1, w_1),$$

$$(2.13c) \quad \frac{dv_2}{dt_s} = f_2(v_2, w_2).$$

System (2.13) still includes two distinct timescales, and we can manipulate the system to obtain either the fast layer problem (2.8), by rescaling time and taking a limit, or the slow reduced layer problem (2.12), by taking a limit. We define the *superslow manifold*, \mathcal{M}_{ss} , to be the set of equilibrium points of the slow layer problem, i.e.,

$$(2.14) \quad \mathcal{M}_{ss} := \{(v_1, v_2, w_1, w_2) : f_1(v_1, v_2, w_1) = g_1(v_1, w_1) = f_2(v_2, w_2) = 0\}.$$

Note that \mathcal{M}_{ss} is a subset of \mathcal{M}_s . Similarly to \mathcal{M}_s , the normally hyperbolic parts of \mathcal{M}_{ss} perturb to nearby locally invariant manifolds for ε_2 sufficiently small, and we approximate the collection of these manifolds by \mathcal{M}_{ss} .

Taking the same limit in (2.6), i.e., $\varepsilon_2 \rightarrow 0$ with $\varepsilon_1 > 0$, gives a system that describes the dynamics of w_2 restricted to \mathcal{M}_{ss} ,

$$(2.15) \quad \frac{dw_2}{dt_{ss}} = g_2(v_2, w_2).$$

We call this system the *superslow reduced problem* and refer to the corresponding dynamics as the *superslow flow*.

There is one more limiting system that turns out to be important for the dynamics we consider. We define the three-dimensional manifold, \mathcal{M}_σ , by

$$\mathcal{M}_\sigma := \{(v_1, w_1, v_2, w_2) : f_2(v_2, w_2) = 0\}.$$

Because the dynamics of (v_2, w_2) decouples from (v_1, w_1) in (2.4), we can find a function F_2 such that

$$(2.16) \quad w_2 = F_2(v_2)$$

on \mathcal{M}_σ . Differentiation of (2.16) with respect to t_s yields

$$\frac{dw_2}{dt_s} = F_2'(v_2) \frac{dv_2}{dt_s}.$$

This equation can be combined with (2.5) to obtain the three timescale system

$$(2.17a) \quad \varepsilon_1 \frac{dv_1}{dt_s} = f_1(v_1, w_1, v_2),$$

$$(2.17b) \quad \frac{dw_1}{dt_s} = g_1(v_1, w_1),$$

$$(2.17c) \quad \frac{dv_2}{dt_s} = \frac{\varepsilon_2 g_2(v_2, F_2(v_2))}{F_2'(v_2)}$$

describing the dynamics on \mathcal{M}_σ , away from its folds (to leading order in ε_2 ; see Remark 1). An analogous system was used heavily in the analysis of three timescale dynamics in [35].

Remark 1. Just as \mathcal{M}_s is defined in the singular limit and perturbs to a nearby locally invariant manifold for $0 < \varepsilon_1 \ll 1$, \mathcal{M}_σ perturbs to a nearby locally invariant manifold for $0 < \varepsilon_2 \ll 1$. This manifold is given by $w_2 = F_2(v_2) + O(\varepsilon_2)$, and additional terms should appear in the v_2 equation in (2.17) to reflect this perturbation, but these are higher order in ε_2 and we omit them.

It will be useful to work with two systems defined from (2.17). First, taking $\varepsilon_1 \rightarrow 0$ yields the slow reduced problem for (2.17) governing the dynamics on $\mathcal{M}_s \cap \mathcal{M}_\sigma$. Taking the subsequent limit $\varepsilon_2 \rightarrow 0$ gives the slow reduced layer problem for (2.17), namely

$$(2.18) \quad \frac{dw_1}{dt_s} = g_1(v_1, w_1),$$

on $\mathcal{M}_s \cap \mathcal{M}_\sigma$; note that this equation is consistent with (2.12) with $f_2 = 0$, although it cannot be obtained by taking a limit in (2.12) directly.

Second, taking $\varepsilon_2 \rightarrow 0$ directly in (2.17) gives

$$(2.19a) \quad \varepsilon_1 \frac{dv_1}{dt_s} = f_1(v_1, w_1, v_2),$$

$$(2.19b) \quad \frac{dw_1}{dt_s} = g_1(v_1, w_1).$$

System (2.19) is the slow layer problem for (2.17). To distinguish it from (2.13), we will also call (2.19) the v_2 -frozen system, with solutions that we call v_2 -frozen solutions. Similarly, when it is helpful, we will refer to (2.18) as the v_2 -frozen system reduced problem and (2.8) as the v_2 -frozen system layer problem, since these can be obtained through appropriate limits from (2.19).

For reference, we summarize the subsystems that are useful for describing the dynamics of (2.4) in Table 2.2.

Within the context of GSPT, the usual way to proceed from here is to construct *singular periodic orbits* by concatenating solution segments of singular limit systems (see Figure 1.1 in the introduction section). A similar method could also be used to explain the oscillations seen in three timescale systems, although the process would be more complicated since there are more than two singular limit systems to be considered. In this chapter, for reasons of brevity, we choose not to show detailed constructions of singular orbits and subsequent analysis of how these perturb. Instead, we appeal to intuition based on the way the technique works in two timescale systems to explain the mechanisms underlying solutions generated in simulations done with a separation of

Table 2.2: Subsystems for (2.4).

equation	system name	dynamic variables	baseline timescale	domain
(2.8)	fast layer / v_2 -frozen layer	v_1	t_f	\mathbb{R}^4
(2.11)	slow reduced	w_1, v_2, w_2	t_s	\mathcal{M}_s
(2.12)	slow reduced layer	w_1, v_2	t_s	\mathcal{M}_s
(2.19)	slow layer on \mathcal{M}_σ / v_2 -frozen	v_1, w_1	t_s	\mathcal{M}_σ
(2.18)	slow reduced layer on \mathcal{M}_σ / v_2 -frozen reduced	w_1	t_s	$\mathcal{M}_s \cap \mathcal{M}_\sigma$
(2.15)	superslow reduced	w_2	t_{ss}	$\mathcal{M}_{ss} \subset \mathcal{M}_s$

scales but away from a true singular limit. In the following discussion, we will show orbits of the full system and refer to different segments of them as being governed by the subsystems in Table 2.2 and evolving under the fast, slow or superslow flow; by this we mean that, in an appropriate singular limit, these segments will converge to nearby solutions of these subsystems.

Remark 2. *We could have chosen alternative values of C_1, C_2, ϕ_1, ϕ_2 to impose a wider separation of timescales. We opted to use the values specified in Table 2.1, corresponding to $\varepsilon_1 = 0.1$ and $\varepsilon_2 = 0.053$, to show that extreme timescale separation is not necessary in order for the issues that we consider to arise. This point will come up again later in the chapter, when proximity of timescales renders certain analysis steps more subtle.*

Recall from Section 1 that identifying the type of fold points (jump points or folded singularities) is fundamental in determining the nature of the solution that arises from a perturbation of a singular periodic orbit in the two timescale context. Similar considerations are also relevant for three timescale systems, although once again the situation is complicated by the existence of more than two singular limit systems. Since \mathcal{M}_s is a three-dimensional surface, fold points of \mathcal{M}_s lie on two-dimensional surfaces within \mathcal{M}_s defined by

$$(2.20) \quad L_s := \left\{ (v_1, v_2, w_1, w_2) \in \mathcal{M}_s : \frac{\partial f_1}{\partial v_1}(v_1, w_1, v_2) = 0 \right\}$$

or, equivalently, as

$$(2.21) \quad L_s := \left\{ (v_1, v_2, w_1, w_2) : w_1 = F_1(v_1, v_2), \frac{\partial F_1}{\partial v_1} = 0 \right\}$$

where F_1 was defined in (2.10).

Folded singularities for three timescale systems have not been comprehensively studied, although [35] classifies the folded singularities in a particular three dimensional, three timescale system by extending ideas from two timescale systems, and [81] extends the concepts developed for two timescale systems with two slow variables to systems with three or more slow variables; ideas related to both of these approaches appear in [77], where a degenerate type of folded singularity that arises naturally in three timescale systems is identified and some analysis of the related dynamics is given.

In the usual manner, we define the desingularised slow reduced problem by differentiating the algebraic equation defining \mathcal{M}_s (i.e., $f_1(v_1, v_2, w_1) = 0$) and rescaling time using $\tau_s = (\partial F_1 / \partial v_1) t_s$, yielding

$$(2.22a) \quad \frac{dv_1}{d\tau_s} = g_1(v_1, w_1) - \frac{\partial F_1}{\partial v_2} f_2(v_2, w_2),$$

$$(2.22b) \quad \frac{dv_2}{d\tau_s} = \frac{\partial F_1}{\partial v_1} f_2(v_2, w_2),$$

$$(2.22c) \quad \frac{dw_2}{d\tau_s} = \varepsilon_2 \frac{\partial F_1}{\partial v_1} g_2(v_2, w_2).$$

We then look for equilibria of (2.22) that are not equilibria of the full system; these are what we refer to as folded singularities of \mathcal{M}_s . We find that they lie on one-dimensional curves within L_s defined by

$$(2.23) \quad FS := \left\{ (v_1, v_2, w_1, w_2) \in L_s : g_1(v_1, w_1) - \frac{\partial F_1}{\partial v_2}(v_1, v_2) f_2(v_2, w_2) = 0 \right\}.$$

Away from \mathcal{M}_{ss} , the linearisation of (2.22) at a folded singularity has one zero eigenvalue (due to there being a curve of folded singularities, as in [81]) and two other eigenvalues; the folded singularities can be classified using these other eigenvalues, as in [35, 81]. As we will see, the location and type of folded singularities within \mathcal{M}_s depends on g_{syn} . We note that points where \mathcal{M}_{ss} and L_s intersect are always folded singularities since $g_1 = f_2 = 0$ on \mathcal{M}_{ss} ; some discussion of this degenerate type of folded singularity is contained in [77].

Since \mathcal{M}_{ss} is a one-dimensional subset of \mathcal{M}_s , fold points of \mathcal{M}_{ss} occur at isolated points; these are located on the set

$$(2.24) \quad L_{ss} := \left\{ (v_1, v_2, w_1, w_2) \in \mathcal{M}_{ss} : \frac{\partial f_2}{\partial v_2}(v_2, w_2) = 0 \text{ or } \frac{\partial f_1}{\partial v_1} \frac{\partial g_1}{\partial w_1} - \frac{\partial f_1}{\partial w_1} \frac{\partial g_1}{\partial v_1} = 0 \right\}.$$

For all values of g_{syn} that we consider below, points that satisfy the latter condition lie on the middle sheet of \mathcal{M}_s and hence will not play a role in the dynamics, and points that satisfy the former condition are jump points.

2.1.2 Effect of coupling

When $g_{syn} = 0$, our model decouples into two systems, each of which has two variables and a two timescale structure. For the parameter values we have chosen, the nullclines for the uncoupled systems are qualitatively as shown in Figure 2.1. Each v nullcline is cubic shaped, with outer branches that are attracting relative to the v dynamics and a repelling inner branch. When solutions are near the outer branch with lower (resp. higher) v values, we say that the system is in the silent (resp. active) phase.

Since the coupling in our system is unidirectional, the oscillations in (v_2, w_2) are independent of the value of g_{syn} and of the dynamics of v_1 and w_1 ; they are standard relaxation oscillations consisting of a superslow excursion through the silent phase (Fig. 2.1B, ①), a slow jump away from the v_2 nullcline up to the active phase (Fig. 2.1B, ②), a superslow excursion through the active phase (Fig. 2.1B, ③), and a slow jump back to the silent phase (Fig. 2.1B, ④). By contrast, v_1 and w_1 depend on g_{syn} and, if $g_{syn} > 0$, on v_2 and w_2 . For positive g_{syn} we find it helpful to consider the phase plane for the v_2 -frozen system (2.19) for various fixed values of v_2 ; this is a reasonable approach to take when v_2 is in a superslow phase, i.e., if the dynamics is close to \mathcal{M}_σ . Figure 2.3 shows configurations of the v_1 and w_1 nullclines for (2.19) for several different values of v_2 with $g_{syn} = 5.1$. Note that the v_1 nullcline satisfies (2.10) and is in fact a section of \mathcal{M}_s .

Continuing in this spirit, bifurcation diagrams can be obtained for (2.19) using v_2 as the bifurcation parameter. Examples are shown in Figure 2.4 for several values of g_{syn} . For $g_{syn} = 4.1$ and $g_{syn} = 5.1$, several families of periodic orbits are seen. The first is almost invisible on the scale of Figure 2.4; as v_2 is increased a branch of unstable small amplitude periodic orbits is created in a homoclinic bifurcation involving the middle branch of equilibria and is destroyed in a subcritical AH bifurcation of the lower branch of equilibria. A second family of stable periodic orbits of much larger amplitude is created in a homoclinic bifurcation also involving the middle branch of equilibria. For $g_{syn} = 5.1$, but not 4.1, this family of orbits terminates for larger v_2 when it coalesces

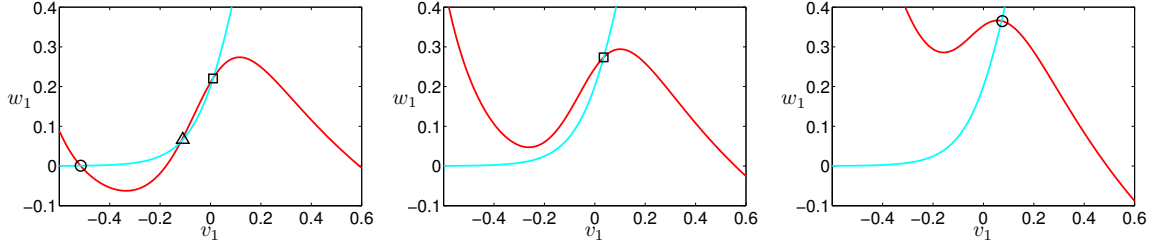


Figure 2.3: Nullclines for v_1 (red) and w_1 (cyan) for the v_2 -frozen system (2.19). The red curve is a slice through \mathcal{M}_s taken at a fixed v_2 and restricted to the (v_1, w_1) plane. The cyan curve is the restriction of the w_1 nullcline to the (v_1, w_1) plane. Varying v_2 changes the red curve but not the cyan curve. From left to right: $v_2 = -0.7, -0.4, 0.2$, all with $g_{syn} = 5.1$. Circles, triangles, and squares denote equilibria of (2.19) of sink, saddle, and source type, resp.

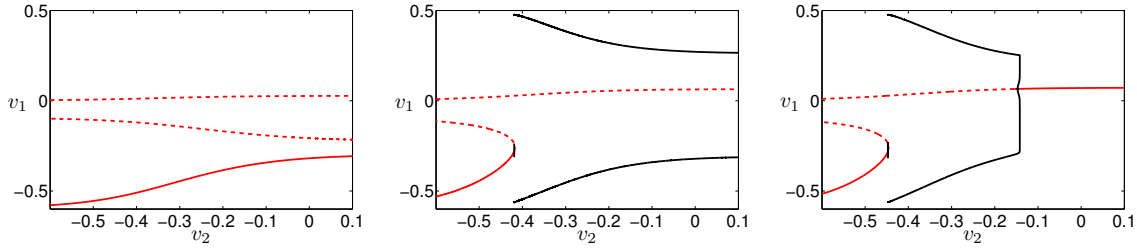


Figure 2.4: Bifurcation diagrams for (2.19) with v_2 as a parameter. From left to right, $g_{syn} = 1.0, 4.1, 5.1$. Solid (resp. dashed) red curves indicate stable (resp. unstable) equilibria, and black curves indicate periodic solutions (stability not indicated).

with a third family of unstable periodic solutions born in a subcritical AH bifurcation at relatively large v_2 . For $g_{syn} = 4.1$, even with the coupling function $S(v_2)$ set to its upper limit of 1, the upper equilibrium point of (2.19) remains unstable and the stable periodic orbits persist as $v_2 \rightarrow \infty$.

Allowing both g_{syn} and v_2 to vary, we find bifurcation curves in the (v_2, g_{syn}) parameter plane, as illustrated in Figure 2.5. The green (resp. blue) curve in the left panel is the curve of AH bifurcations on the lower (resp. upper) branch of equilibria. These approach horizontal asymptotes

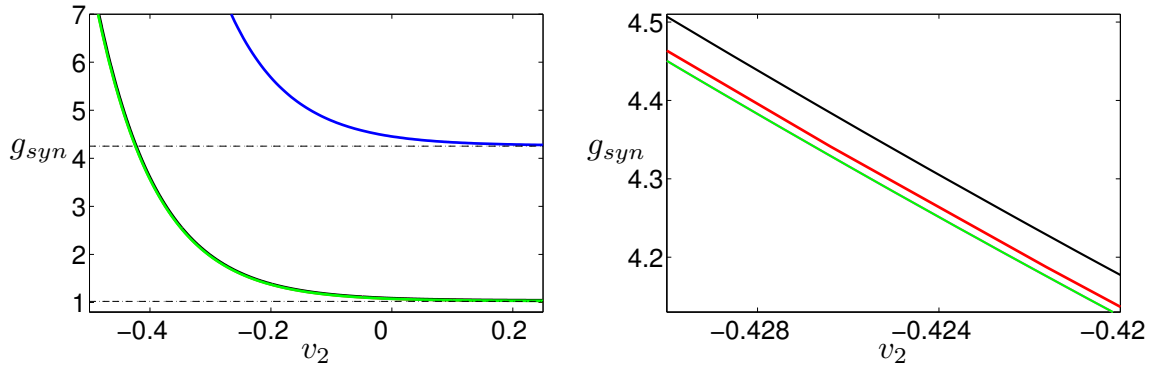


Figure 2.5: Bifurcation curves for (2.19) in (v_2, g_{syn}) parameter space. Left: Two curves of AH bifurcations (green, lower v_1 ; blue, higher v_1) and their horizontal asymptotes (dashed). Right: Enlargement of part of left panel showing, in order of increasing v_2 and g_{syn} , part of the lower AH curve (green), two overlapping homoclinic bifurcation curves (red), and, for comparison, the curve of saddle-node bifurcations that occurs at relatively low v_1 (black).

as v_2 increases; the lower asymptote is at $g_{syn} \approx 1.0319 =: \tilde{g}$ while the upper asymptote is at $g_{syn} \approx 4.2628 =: \bar{g}$. Existence of the upper asymptote implies that the (v_1, w_1) system will not oscillate for any fixed $g_{syn} > \bar{g}$ if v_2 is fixed at a large enough value; this is illustrated in the right panel of Figure 2.4. The onset of stable oscillations, on the other hand, is not directly tied to the green AH curve, since that curve relates to the family of unstable oscillations near the lower branch of equilibria. To identify the onset of stable oscillations, we compute the curve of homoclinic bifurcations through which the stable large amplitude oscillations arise as v_2 increases. It turns out that this curve lies extremely close to the lower AH curve (compare the red and green curves in the right panel of Figure 2.5), with approximately the same asymptote. Thus, for $g_{syn} < \tilde{g}$, there is no value at which v_2 can be fixed to yield oscillations in (v_1, w_1) , while for $g_{syn} \in (\tilde{g}, \bar{g})$, oscillations occur for all v_2 above the homoclinic bifurcation.

The structure of the bifurcation set in Figure 2.5 stems in part from the form of the coupling function $S(v_2)$ in (2.1), as defined in (2.2) and shown in Figure 2.6. For v_2 sufficiently small or sufficiently large, $S(v_2)$ varies little in response to changes in v_2 , whereas for intermediate values

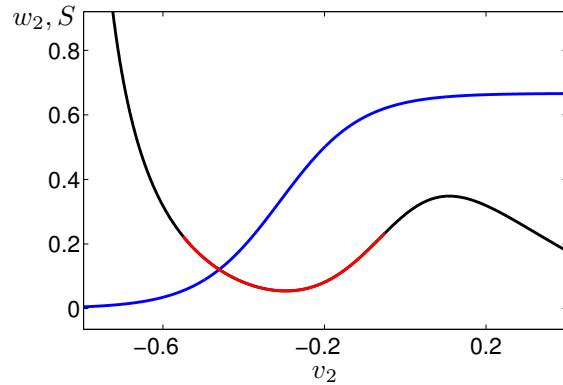


Figure 2.6: Graph of $S(v_2)$ (blue) and locus of the v_2 -nullcline (black/red). The red section of the v_2 -nullcline indicates the range of v_2 values over which $S(v_2)$ is steeply sloped.

of v_2 , $S(v_2)$ changes rapidly with v_2 (red in Figure 2.6). As a consequence, changes of v_2 within the intermediate interval result in significant effects on the v_1 equation, while changes in v_2 outside of this domain have little effect. This saturation of S explains why the horizontal asymptotes in Figure 2.5 exist and why certain bifurcations cannot be achieved by increasing v_2 in (2.19) if g_{syn} is not sufficiently large. Figure 2.6 also shows where the steepest part of S lies relative to the v_2 nullcline. We see that $S(v_2)$ is sensitive to changes in v_2 over the silent phase and over jumps between phases but is insensitive to v_2 in the active phase for the parameter values we use.

As noted above, the (v_2, w_2) dynamics is not dependent on (v_1, w_1) or on g_{syn} ; with parameters fixed as in Table 2.1, the (v_2, w_2) variables trace out a relaxation oscillation, shown in the right panel of Figure 2.1. It will be helpful to define some reference points along the relaxation oscillation. Figure 2.7 shows the (v_2, w_2) oscillation from Figure 2.1 plotted in non-dimensionalised coordinates, with green symbols marking points at the transition between the four different sections of the oscillation. These symbols have the same interpretation in all the figures and analysis that follow.

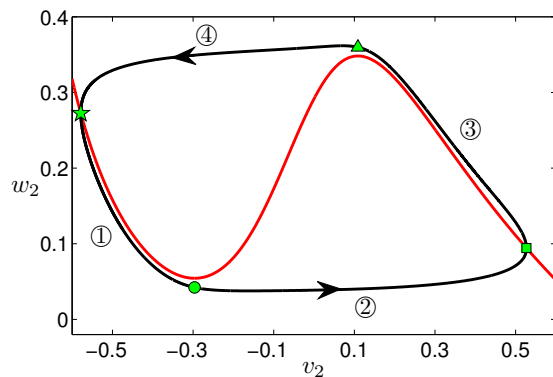


Figure 2.7: Attracting dynamics in (v_2, w_2) -space. The green symbols mark the approximate points of transition between the slow and superslow sections of the oscillation: the square and star mark the transitions from slow to superslow motion, and the circle and triangle mark the transitions from superslow to slow motion. The circled numbers label the sections of the oscillation, using the same convention as in the right panel of Figure 2.1.

2.2 ANALYSIS OF THREE TIMESCALE SOLUTIONS

Simulation of (2.4) over a range of parameter values yields a variety of solution behaviors, with variation in g_{syn} giving a particularly nice progression of features. We focus our analysis on three values of g_{syn} ; these values highlight the distinct combinations of dynamic mechanisms that can arise for (2.4) and together capture the most interesting dynamic effects that we have identified over a range of g_{syn} values. The case $g_{syn} = 1.0$ represents an interesting transitional case between solutions in which v_1 remains relatively steady at a low level and solutions for which v_1 spikes repeatedly. The cases $g_{syn} = 4.1$ and $g_{syn} = 5.1$ are representative of two related yet distinct solution behaviors each seen over a wide range of g_{syn} values.

In the following, we will present analysis from two points of view, one that focuses on the roles of \mathcal{M}_s and \mathcal{M}_{ss} in organizing the flow of the full model and another that focuses on how the oscillations of (v_2, w_2) affect the dynamics of (v_1, w_1) . The inclusion of both perspectives, we feel, provides the clearest picture of how the dynamics emerges, and may be of use to those readers who

typically adopt only one perspective or the other.

2.2.1 Case 1: $g_{syn}=1.0$

2.2.1.1 (v_1, w_1) driven by (v_2, w_2) We now consider (2.1) from the perspective of a fast-slow system driven by a slow-superslow oscillation. The use of this kind of perspective has proved helpful in past analyses of various models with two timescales (e.g., [71, 70, 57, 55, 12]).

Recall that for the parameter values we are considering, in the absence of coupling, the (v_1, w_1) system has a stable equilibrium but no oscillatory solution. If coupling is introduced by setting $g_{syn} = 1.0$, however, then oscillations in v_1 are observed, as can be seen in Figure 2.2. It might be natural to ascribe the onset of these oscillations to variation of v_2 pushing the v_2 -frozen system (2.19) through a bifurcation at which oscillations are born. As shown in Figures 2.4 and 2.5, however, there is no such bifurcation for $g_{syn} = 1.0$. The key point in considering the dynamics with $g_{syn} = 1.0$ from the perspective of (v_2, w_2) driving (v_1, w_1) is to explain the observed oscillations in v_1 .

To provide this explanation, we consider the phases of the (v_2, w_2) oscillation in succession. The yellow dot in Figure 2.9 marks the point in phase ③ where the conditions $f_1 = g_1 = f_2 = 0$ become (approximately) satisfied; the trajectory at this point lies on the v_2 -nullcline when projected to the (v_2, w_2) plane and at the intersection of the v_1 and w_1 nullclines of the v_2 -frozen system (2.19) when projected to the (v_1, w_1) plane. From the yellow dot, the solution evolves under the superslow reduced problem (2.15) with v_2 slaved to w_2 . The evolution of v_2 in turn moves the v_1 nullcline of (2.19) on the superslow timescale, while the w_1 nullcline is independent of v_2 and thus remains fixed. The (v_1, w_1) projection of the trajectory then tracks the intersection of the v_1 and w_1 nullclines. In fact, $v_2 > 0$ throughout phase ③, so based on the shape of $S(v_2)$, which provides the coupling from v_2 to v_1 , these intersection points depend only very weakly on v_2 (see Figure 2.6). Thus, if projected to the (v_1, w_1) plane, the yellow dot would lie almost on the green triangle that marks the end of phase ③, and the trajectory remains near the green triangle throughout this part of phase ③ (Figure 2.8).

After the trajectory passes the green triangle and moves into phase ④, the condition $f_2 = 0$ no longer applies. The flow is now governed by the slow reduced layer problem (2.12). The trajectory

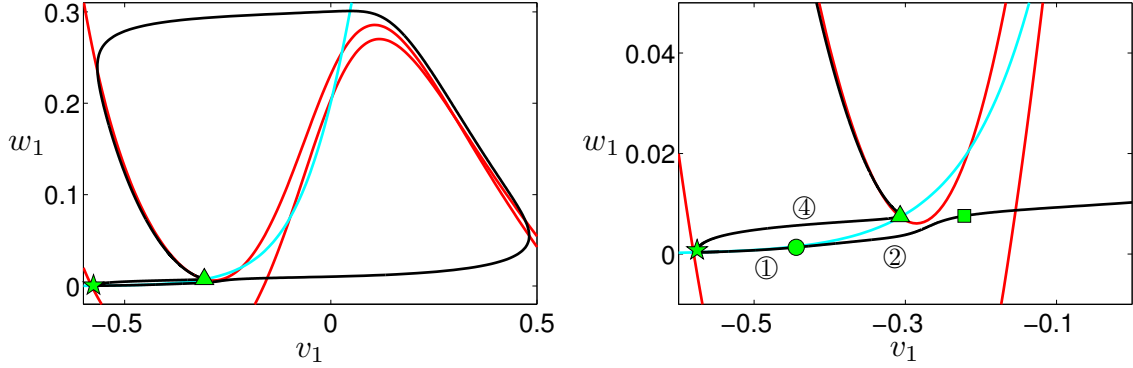


Figure 2.8: An attracting solution of (2.4) for $g_{\text{syn}} = 1.0$ (black curve) projected to the (v_1, w_1) plane; the right panel shows an enlargement of part of the left panel. Circled numbers and green symbols correspond to phases of the (v_2, w_2) oscillation and the transition points, as shown in Figure 2.7. The cyan curve is the w_1 nullcline for (2.19), which is independent of v_2 , while the red curves are the v_1 nullclines for (2.19) for $v_2 = v_{2_{\text{max}}}$ (higher red curve) and $v_2 = v_{2_{\text{min}}}$ (lower red curve).

still lies on \mathcal{M}_s , and thus, in the projection to the (v_1, w_1) plane, is on the curve $f_1(v_1, w_1, v_2) = 0$, but it diverges from the w_1 -nullcline (cyan curve in Figure 2.8). Correspondingly, the trajectory diverges from the red curve in Figure 2.9, which shows the w_1 -coordinate of the intersection of v_1 - and w_1 -nullclines of (2.19) for each v_2 .

Phase ④ ends when the trajectory converges to a critical point of (2.12), at which time its projection to the (v_2, w_2) plane reaches the left branch of the v_2 -nullcline. The v_2 -coordinate of this point is the minimal value of v_2 along the trajectory; call it $v_{2_{\text{min}}}$. Within the (v_1, w_1) plane, the trajectory is seen to converge to a point at the intersection of the v_1 and w_1 nullclines for the v_2 -frozen system (2.19), with the v_1 nullcline computed with $v_2 = v_{2_{\text{min}}}$ (green star in Figure 2.8). This convergence corresponds to the end of the jump between branches of \mathcal{M}_{ss} within \mathcal{M}_s^l described in the previous subsection.

Next, phase ① is governed by the superslow reduced flow (2.15), as for phase ③. Under this flow, the v_1 -nullcline for (2.19) moves superslowly in the (v_1, w_1) plane while the w_1 -nullcline

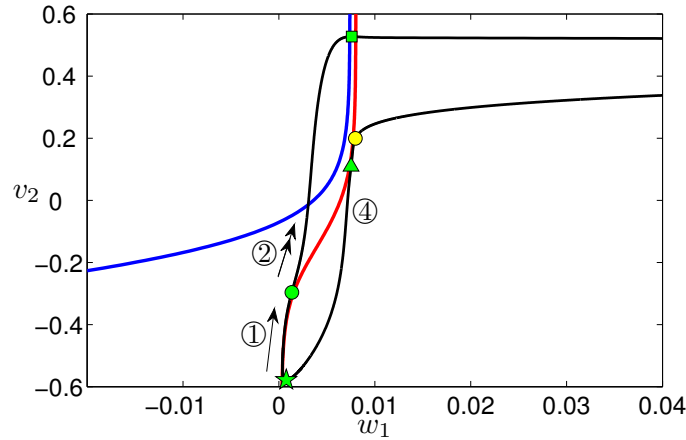


Figure 2.9: The attracting trajectory from Figure 2.8 (black curve) projected onto the (w_1, v_2) plane. Circled numbers and green symbols correspond to phases of the (v_2, w_2) oscillation and their transition points as in Figure 2.7. The yellow dot indicates where the trajectory reaches a small neighborhood of a critical point of the slow reduced layer problem on \mathcal{M}_σ , namely a point of \mathcal{M}_{ss} within \mathcal{M}_s^l . The blue curve shows the w_1 -coordinate of the left fold of the v_1 -nullcline for (2.19), while the red curve indicates the w_1 -coordinate of the intersection of the v_1 - and w_1 -nullclines for (2.19), both parametrized by v_2 . The direction of flow on the trajectory is indicated by arrows, one arrowhead for superslow flow and two for slow flow.

stays fixed, and the projection of the trajectory tracks the fixed point of (2.19) along the w_1 -nullcline (green star to green circle in Figures 2.8-2.9). Since there is no bifurcation in (2.19) as v_2 varies, this situation continues until the trajectory reaches the lower fold of the v_2 -nullcline in the (v_2, w_2) plane, as marked by the green circle, at the end of phase ①.

The most interesting phase of this oscillation is phase ②. At the start of this phase (green circle in Figures 2.8 and 2.9), the trajectory is governed by (2.12) and v_2 begins a slow jump away from its nullcline. During this slow jump, v_1 is slaved to w_1 and v_2 , as in phase ④. Even though (2.19) does not govern the evolution of this part of the trajectory, it is still useful to track the v_1 nullcline of (2.19), which slowly slides in the direction of increasing w_1 in the (v_1, w_1) plane.

Each such nullcline has two folds; as can be seen in Figure 2.9, the slow flow of (2.12) steers the trajectory across the one-dimensional curve of lower folds of the family of v_1 nullclines (blue curve), projected to the (w_1, v_2) space. Thus, we observe that the flow of (2.12), in which the two slow variables conspire to pull the trajectory away from the curve of fixed points of (2.19) and across the curve of lower folds of the family of v_1 -nullclines, is crucial for the emergence of an oscillation in v_1 for $g_{syn} = 1.0$.

Following the fold crossing, there is a fast jump in v_1 governed by (2.8), from left to right branches of the v_1 -nullcline family in the projection to the (v_1, w_1) plane. If we had a greater separation of timescales, then the jump would occur almost as soon as the fold was crossed. With the weaker separation that we consider, the jump is delayed; it begins quite close to the end of phase ② and ends during phase ③ (Figure 2.8, right panel). Once the jump in v_1 is complete, just after the start of phase ③, the trajectory evolves under (2.18) or, equivalently, under the reduced problem for (2.19), tracking the right branches of the v_1 -nullclines in the direction of increasing w_1 in the projection to the (v_1, w_1) plane (Figure 2.8, left and Figure 2.9). The trajectory eventually reaches the right knee curve of the v_1 -nullcline family and jumps down to the left v_1 -nullcline branches under (2.8) or, equivalently, under the layer problem of (2.19). Finally, the trajectory converges under (2.18) to the curve of critical points where the v_1 -nullclines intersect the w_1 -nullcline (yellow dot in Figure 2.9), bringing us back to where we started our description.

Remark 3. *In the true singular limit, we expect that the fast jump up of v_1 would happen instantly with respect to the slow timescale, during phase ②. After that jump, w_1 and v_2 would evolve according to (2.12), continuing phase ②, until being interrupted again by the fast jump down of v_1 . Finally, the slow evolution of (2.12) would continue until convergence to where $f_1 = g_1 = f_2 = 0$, analogous to our yellow dot point, at the end of phase ②. This progression is expected from GSPT and we have observed it numerically (not shown).*

2.2.2 Case 2: $g_{syn}=4.1$

2.2.2.1 (v_1, w_1) driven by (v_2, w_2) We now use our alternative perspective to explain properties of the attracting solution when $g_{syn} = 4.1$. Figure 2.4 shows that treating v_2 as a parameter in the v_2 -frozen system (2.19) and increasing v_2 from its minimal relevant value pushes (2.19)

through a homoclinic bifurcation, resulting in the appearance of oscillatory solutions of (2.19); these oscillations persist no matter how large v_2 becomes, which explains why the v_1 spikes continue throughout phase ③ as v_2 drifts on the superslow timescale and only end after v_2 drops below the homoclinic bifurcation value during phase ④.

Next, we explain why the amplitude of the v_1 spikes decreases progressively during phase ① until v_2 jumps up in phase ②, and then remains approximately constant throughout phase ③. Consider the effect of v_2 on the position of the v_1 -nullcline of (2.19). At the start of phase ① the v_1 - and w_1 -nullclines intersect in three critical points (Figure 2.10, lowest red curve and cyan curve). Under (2.17), as v_2 increases on the superslow timescale during phase ①, it raises the corresponding v_1 -nullcline of (2.19). This rise is not uniform in v_1 , however; since it occurs through the term $g_{syn}S(v_2)(v_1 - V_{syn})$ in (2.1), a fixed change in v_2 causes a relatively large change in the w_1 -values along the part of the v_1 -nullcline with v_1 far below V_{syn} , including the left branch of the v_1 -nullcline, and a relatively small change where $|v_1 - V_{syn}|$ is small, including the right branch of the v_1 -nullcline (Figure 2.10).

The increase in v_2 causes a bifurcation in which two of (v_1, w_1) critical points near the left knee of the v_1 -nullcline, with v_1 values far from V_{syn} , merge and annihilate. For each v_2 above the bifurcation value, (2.19) exhibits a stable relaxation oscillation involving fast jumps in v_1 between branches of the v_1 -nullcline alternating with slow drift in (v_1, w_1) along these branches. Since the right branch of the nullcline depends little on v_2 , each jump down occurs from a similar value of w_1 even as v_2 varies (Figure 2.10). The minimal values of v_1 within spikes are determined by the fast flow and increase with v_2 , since they are on the left branches of the v_1 -nullclines. Thus, we find increasing v_1 values along successive v_1 spike troughs before v_2 becomes active. Furthermore, the jumps up in v_1 occur from larger w_1 values across successive spikes as v_2 increases. These jumps land at points on similar negatively sloped right branches, meaning that an increase in w_1 translates to a decrease in v_1 at the landing point (Figure 2.10). Thus, peak values of v_1 decrease across successive spikes during this phase.

When phase ① ends, v_2 jumps up through and beyond the active range of $S(v_2)$ (Figure 2.6) to the right branch of its nullcline in the (v_2, w_2) phase plane, where phase ③ begins. The (v_1, w_1) relaxation oscillations continue; since $S(v_2)$ remains approximately constant, so does the v_1 -nullcline and hence so do the quantitative features of the relaxation oscillation. The insensitivity of the v_1

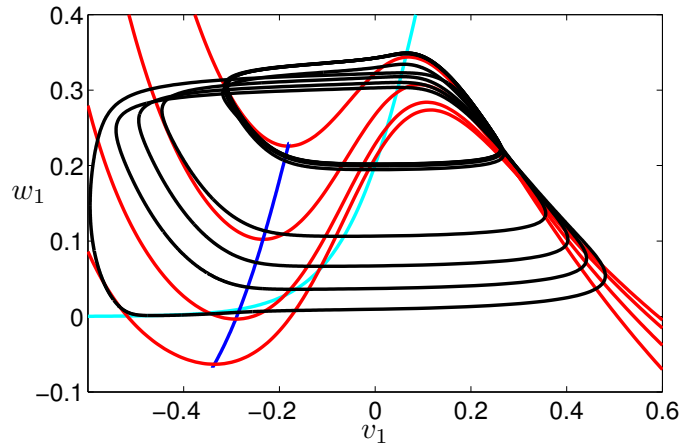


Figure 2.10: An attracting solution of (2.4) for $g_{\text{syn}} = 4.1$, projected to (v_1, w_1) -space (black curve). The red curves are v_1 -nullclines for a selection of fixed values of v_2 ; these move upwards as v_2 increases. The cyan curve is the w_1 -nullcline, which is independent of v_2 , and the blue curve denotes the left folds of the v_1 -nullclines over the full range of v_2 arising during v_2 oscillations.

equation to v_2 in phase ③ explains why the v_1 spikes have approximately constant amplitude throughout this phase (upper right cycles in the trajectory in Figure 2.10).

The discussion above shows how variations in v_2 can shape the v_1 spikes: superslow drift in v_2 imposes a superslow v_1 spike amplitude modulation. To appreciate fully how transitions in the v_2 dynamics relate to the (v_1, w_1) dynamics, we consider the projection of the attracting solution onto the (w_1, v_2) plane (see Figure 2.11). During the part of phase ① when there is no spiking, the trajectory evolves under (2.15), moving along an attracting branch of \mathcal{M}_{ss} (near the single arrow). A fast excursion away from \mathcal{M}_{ss} , and in fact away from \mathcal{M}_s altogether, occurs when the branch of \mathcal{M}_{ss} crosses the fold of \mathcal{M}_s (green diamond). At the onset of the fast jump, v_2 is still below the value corresponding to the left fold of the v_2 -nullcline and continues to drift on the superslow timescale while the (v_1, w_1) system has alternating fast and slow segments, with w_1 oscillating between the folds of the v_1 -nullcline (blue curves), under (2.17). Once the lower fold of the v_2 -nullcline is crossed (green circle), (2.12) governs the slow segments of the trajectory; these

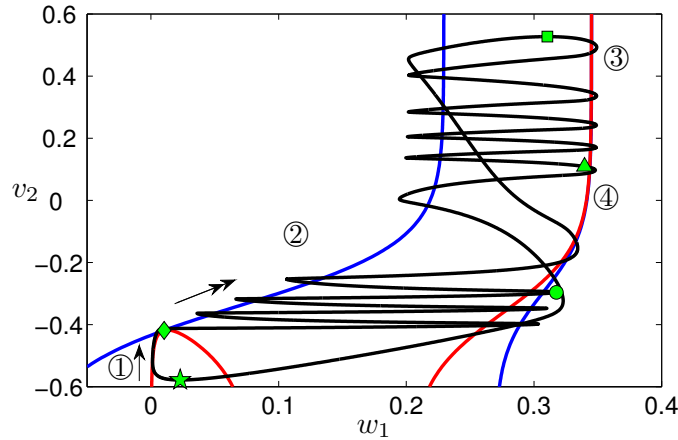


Figure 2.11: Projection to the (w_1, v_2) -plane illuminates several features of the periodic solution (black) for $g_{syn} = 4.1$. The red curves are branches of \mathcal{M}_{ss} or, equivalently, critical points of (2.19), the blue curves are the left (smaller w_1) and right (larger w_1) folds of the v_1 -nullcline, the green diamond marks the time point when v_1 begins spiking, and the other green symbols have the same meanings as in Figure 2.7.

alternate with fast jumps governed by (2.8), but there is only time for a few of these jumps, since w_1 and v_2 evolve on the same timescale during this phase. The return of (v_2, w_2) to a neighborhood of the v_2 -nullcline occurs as v_2 reaches its maximum value (green square); then the evolution of v_2 becomes superslow again, so that only small decreases in v_2 are seen during the subsequent spikes governed by (2.19). This progression continues until (v_2, w_2) crosses the right fold of the v_2 -nullcline (green triangle), at which time another slow jump in v_2 occurs. Under (2.12), the trajectory then converges back to \mathcal{M}_{ss} , completing the cycle.

Figure 2.11 shows clearly the v_2 -dependence of the w_1 coordinate on folds of the v_1 -nullcline of (2.19), as discussed earlier. The w_1 coordinate of the left folds of the v_1 -nullcline depends strongly on v_2 while v_2 is negative but becomes approximately independent of v_2 at positive v_2 , while the w_1 coordinate of the right folds is more weakly dependent on v_2 and also becomes approximately independent of v_2 for v_2 sufficiently large (Figure 2.11). Correspondingly, the minimal w_1 value

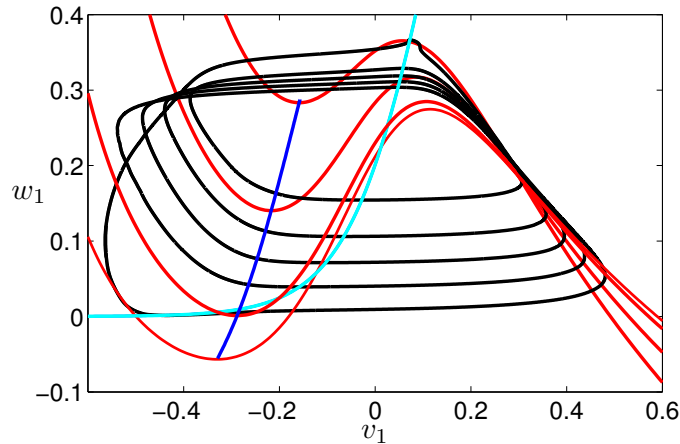


Figure 2.12: An attracting solution of (2.4) for $g_{syn} = 5.1$, projected to (v_1, w_1) -space (black curve), together with nullclines for (2.19). Colours of curves are as in Figure 2.10.

during a spike increases on subsequent spikes when the (v_2, w_2) system is in phase ①, as does the minimal v_1 value, and is approximately constant when the (v_2, w_2) system is in phase ③. The maximal w_1 value remains relatively constant over all spikes.

2.2.3 Case 3: $g_{syn}=5.1$

2.2.3.1 (v_1, w_1) driven by (v_2, w_2) Comparing the relevant bifurcation diagrams in Figure 2.4 shows that changes in v_2 have a qualitatively similar impact on the v_2 -frozen system (2.19) for $g_{syn} = 5.1$ as for $g_{syn} = 4.1$ except that for $g_{syn} = 5.1$, when v_2 becomes sufficiently large, oscillations of (2.19) are lost as a stable critical point at elevated v_1 is born through an AH bifurcation. Correspondingly, comparing Figures 2.12 and 2.10 reveals a similar progression of v_1 -nullclines except that when $g_{syn} = 5.1$, the upper knee of the v_1 -nullcline eventually crosses the w_1 -nullcline, so that the w_1 -nullcline intersects the uppermost v_1 -nullcline on its right branch. The trajectory tends towards this intersection point on the slow timescale during phase ② and remains in a small neighborhood of the point throughout phase ③.

Similarly, there is a strong resemblance between the slow phase plane projections in Figures

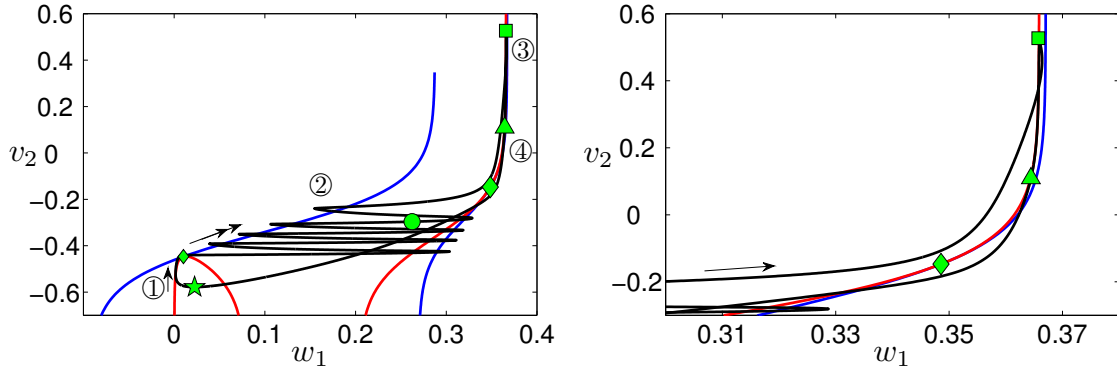


Figure 2.13: Projection to the (w_1, v_2) plane illuminates several features of the periodic solution (black) for $g_{syn} = 5.1$. Color coding and symbols have the same meaning as in Figure 2.11, except there is now a diamond appearing on the upper (larger w_1) branch of \mathcal{M}_{ss} , corresponding to the location of an AH bifurcation in the frozen system (2.19) with v_2 treated as a parameter. Right panel shows an enlarged view.

2.13 and 2.11. The key new feature that arises for $g_{syn} = 5.1$ is that there is an attracting limit point of (2.12) at the green square in Figure 2.13. This point becomes attracting because the curve of critical points of (2.19) (red) crosses through the fold curve (blue) with increasing v_2 ; due to the projection, the crossing appears as a tangency in Figure 2.13 (green diamond). After the trajectory reaches the green square, it drifts back down the red curve on the superslow timescale under (2.15) until it returns to the fold line (green square to green triangle) and then departs from the nullcline intersection curve on the slow timescale, again under (2.15), converging towards the lower stable branch of \mathcal{M}_{ss} .

Importantly, as noted in the previous subsection, the convergence to the limit point on the upper branch of \mathcal{M}_{ss} occurs on the slow timescale, governed by (2.12). That is, while v_2 evolves along the left branch of the v_2 -nullcline on the superslow timescale as part of (2.17), (v_1, w_1) engage in fast-slow relaxation oscillations as described by their equations, which comprise (2.19). Once v_2 reaches the lower fold of the v_2 -nullcline, however, there is a transition to a phase of slow flow of (2.12) with $v_1 \approx v_1(w_1, v_2)$ satisfying $f_1(v_1(w_1, v_2), v_2, w_1) = 0$. The linearization of (2.12) about

its limit point on \mathcal{M}_{ss} yields an upper triangular matrix with real eigenvalues, which can easily be shown to be negative as expected. Thus, this convergence features a direct transition from v_1 spikes to a v_1 plateau, with no damped oscillations. We shall see later that this property contrasts with features of similar solutions in two timescale systems.

2.3 IDENTIFYING THREE TIMESCALE FEATURES

We next seek to identify which aspects of the solutions discussed above are truly three timescale features in some reasonable sense. In this section we find it useful to work with our original dimensional system (2.1), which produces the solutions shown in Figure 2.2, but, for convenience, we omit units on the parameter values.

Our approach is to transform (2.1) into certain two timescale systems by adjusting system parameters, then consider whether these systems can generate solutions that are similar to the three cases considered in Section 2.2. We will exaggerate the timescale separation in the three timescale system, speeding up V_1 by decreasing C_1 from 8 to 0.8 and slowing down w_2 by decreasing ϕ_2 from 0.001 to 0.0001. This amounts to reducing both ϵ_1 and ϵ_2 by a factor of 10, to 0.01 and 0.0053, respectively. In our original scaling and in this exaggerated version, our system has 1 fast, 2 slow, and 1 superslow (1F, 2S, 1SS) variables. There are many ways to regroup timescales to transform this system into a two timescale system. One natural approach is to slow down V_1 , say by setting $C_1 = 80$, so that it evolves on the same timescale as w_1 and V_2 , resulting in a 3 slow, 1 superslow (3S, 1SS) system; similar effects are seen if w_1 , V_2 and w_2 are sped up appropriately to produce a system with three fast and one slow (3F, 1S) variables. Another approach is to speed up w_2 , say by increasing ϕ_2 to 0.01, so that it evolves on the same slow timescale as V_2 and w_1 and we have a 1 fast, 3 slow (1F, 3S) system; qualitatively similar effects will be seen for a one slow, three superslow (1S, 3SS) system obtained by slowing V_1 , w_1 and V_2 appropriately. Other rescalings are also possible, leading to pairs of variables on each of two scales, but these require more significant changes, namely modifying the relative speeds of evolution of two variables or altering the speed of one variable by two orders of magnitude, and so will not be considered.

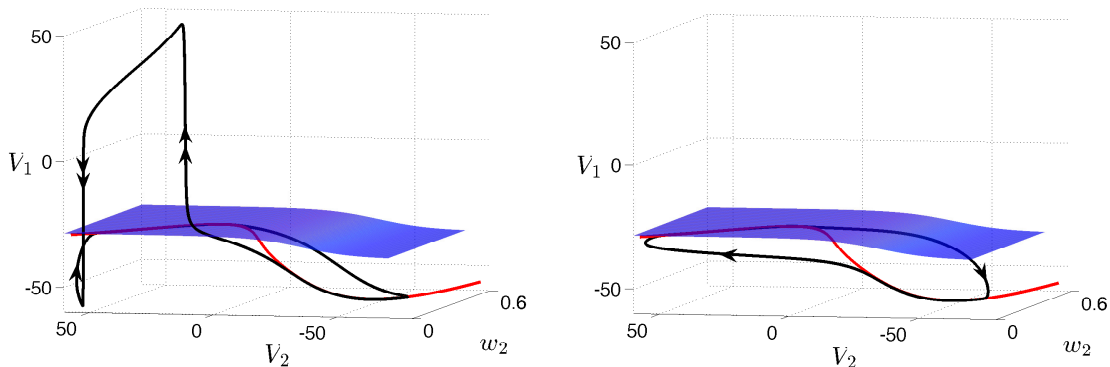


Figure 2.14: Projections of solutions for $g_{syn} = 1.0$ onto (V_1, V_2, w_2) -space. The solution trajectory (black curve) exhibits a spike in V_1 for the (1F, 2S, 1SS) system (left) but not for the (3S, 1SS) system (right). In both cases, the red curves are \mathcal{M}_{ss} , with stable (unstable) branches drawn as solid (dashed) curves. For the (1F, 2S, 1SS) case, the blue surface represents the lower fold of \mathcal{M}_s . The same surface is shown in the (3S, 1SS) case for comparison, although \mathcal{M}_s is no longer meaningful.

2.3.1 $g_{syn} = 1.0$: recruitment of a transient V_1 spike

When $g_{syn} = 1.0$, (2.1) generates a solution with a single V_1 spike per period, as shown in the first panel of Figure 2.2. With exaggerated timescale separation, there is little change in this solution. We first compare this solution to solutions from the (3S,1SS) version of the (2.1) described above.

Projections onto (V_1, V_2, w_2) -space show that in the (1F, 2S, 1SS) system, the trajectory reaches the lower fold surface of \mathcal{M}_s and jumps to higher V_1 . No analogous jump occurs in the (3S, 1SS) case with $g_{syn} = 1.0$ (Figure 2.14), resulting in an absence of spikes in the V_1 time course (Figure 2.15, top panel). The fact that (2.19) does not have an AH bifurcation when the frozen variable v_2 is varied can be used to explain why there is no V_1 spike in the (3S, 1SS) case. Consider a trajectory of the (3S, 1SS) system evolving under the superslow flow on the critical manifold for that system, namely \mathcal{M}_{ss} , on a branch where V_1 and V_2 are low. Suppose this trajectory reaches a fold of \mathcal{M}_{ss} such that a transition to the slow layer problem occurs. By construction, the slow layer

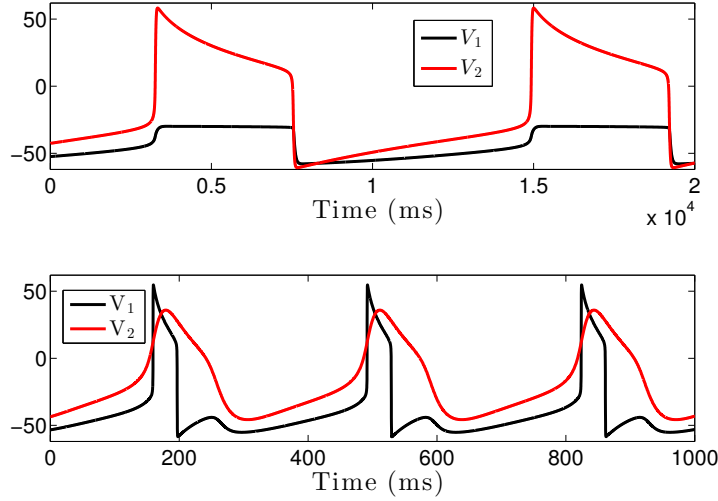


Figure 2.15: Time series of rescaled versions of (2.1) with $g_{\text{syn}} = 1.0$. Top: (3S, 1SS) case, with $C_1 = 80$, $\phi_2 = 0.0001$; Bottom: (1F, 3S) case, with $C_1 = 0.8$, $\phi_2 = 0.01$. Other parameters as in Table 2.1.

problem in this case has a unique stable equilibrium point with V_2 high and V_1, w_1 low. The value of V_2 at this equilibrium can be obtained from solving $dV_2/dt_s = 0$ and $\partial(dV_2/dt_s)/\partial V_2 < 0$. The corresponding values of V_1 and w_1 are those for the unique stable equilibrium point of the dimensional version of (2.19) at this V_2 value (see Figure 2.4). Hence, after passing the fold of \mathcal{M}_{ss} , the solution of the (3S, 1SS) system will follow the slow layer flow to the unique stable equilibrium of the layer problem, as seen in the jump from the low- V_2 branch of \mathcal{M}_{ss} to the high- V_2 branch in the right panel of Figure 2.14. The subsequent motion is governed by the superslow flow, with V_2 slaved to w_2 and (V_1, w_1) following the V_2 -dependent branch of stable equilibria until V_2 jumps down again.

The solutions to the (3S, 1SS) case remain similar for all g_{syn} values for which there is no AH bifurcation in (2.19) as v_2 is varied. For g_{syn} fixed sufficiently above the minimal bifurcation value (\tilde{g} from Section 2.1), on the other hand, the trajectory of the (3S, 1SS) system does exhibit a slow V_1 spike after reaching the fold of \mathcal{M}_{ss} . These spikes continue even after V_2 reaches the

active phase, however. That is, during its active phase, V_2 is slaved to w_2 and hence evolves on the superslow timescale, while the spikes in V_1 (and w_1) occur on the slow timescale and hence occur repeatedly. By continuity, there is a small range of g_{syn} values close to but above \tilde{g} for which very few or even one V_1 spike occurs, but such limited spiking arises because the (V_1, w_1) components of the slow vector field remain quite small beyond the AH bifurcation. Hence, the spikes appear with a significant delay relative to the slow activation of V_2 , yielding a qualitatively different solution from that found in the (1F, 2S, 1SS) system with $g_{syn} = 1.0$. Such solutions are straightforward to find numerically but, for reasons of space, we do not show an example here.

Under the alternative rescaling to a (1F, 3S) system, the attracting trajectory with $g_{syn} = 1.0$ is as shown in Figure 2.15 (bottom). The spike in V_1 has been restored and the fast jumps in V_1 can be described using the fast flow. However, the solution differs qualitatively from that for the (1F, 2S, 1SS) system (Figure 2.2). In the (1F, 3S) case, after the initial rise in V_1 under the fast flow, the trajectory is governed by the 3-dimensional slow reduced problem along \mathcal{M}_s^u . There is no longer a superslow manifold to attract w_1 and V_2 and there is no longer a relaxation oscillation in (V_2, w_2) . Thus, the time the trajectory spends on the upper sheet of \mathcal{M}_s (with large V_1) is commensurate with the time for V_2 to fall from higher to lower values, and so the V_1 spike has similar duration to that of V_2 . Moreover, after the fast jump down from the upper fold, w_1 continues to evolve along with V_2 and w_2 rather than settling down, and since V_1 is slaved to (w_1, V_2) along \mathcal{M}_s^l , there is no longer a prolonged plateau in V_1 after the trough of its spike.

In summary, neither of these two timescale systems captures the full features of the oscillating solution shown in the first panel of Figure 2.2. Since a two timescale system will either lose the large spikes in the V_1 time series, generate additional or delayed V_1 spikes, or elongate the V_1 spikes relative to the V_2 spikes and eliminate the plateau in V_1 after each spike, it appears that for (2.1) to produce the solution shown in Figure 2.2, its three timescale structure must be preserved. We therefore classify the solution shown in Figure 2.2 with $g_{syn} = 1.0$ as an intrinsically three timescale phenomenon.

2.3.2 $g_{syn} = 4.1$: transition from V_1 spikes of gradually decaying amplitude to V_1 spikes of constant amplitude

When the timescale separation is exaggerated in the (1F, 2S, 1SS) scaling, the qualitative form of the solution with $g_{syn} = 4.1$ does not change, nor does the relevance of the mechanisms shown in Figure 2.10-2.11, although the number of V_1 spikes per cycle increases because the slowed superslow flow prolongs the solution period. In particular, the V_1 time series continues to exhibit two groups of rapid spikes, one with decrementing amplitudes and one with constant amplitudes, corresponding to passage of the trajectory near parts of \mathcal{M}_s with low V_2 (phase ①) and elevated V_2 (phase ③), resp. With rescaling to (3S, 1SS), the solution time series changes qualitatively (Figure 2.16, top). In this case, the V_1 spike amplitudes are initially approximately constant, rather than decrementing, then taper off into damped oscillations and approach a plateau, rather than maintaining a fixed amplitude.

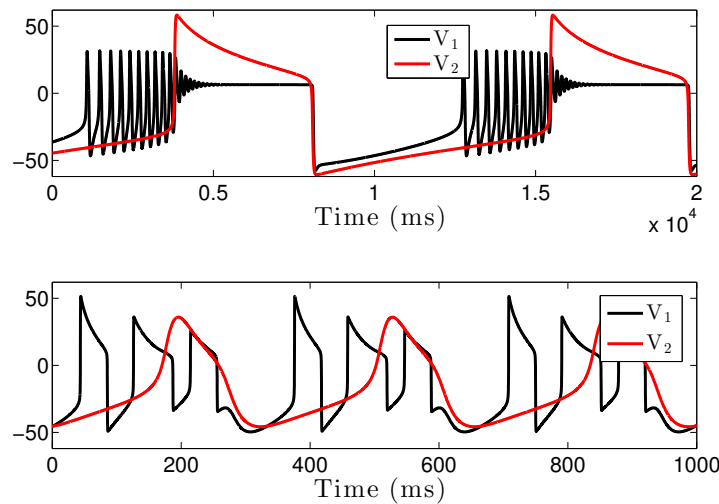


Figure 2.16: Time series of (2.1) with $g_{syn} = 4.1$. Top: (3S, 1SS) case, with $C_1 = 80$, $\phi_2 = 0.0001$; Bottom: (1F, 3S) case, with $C_1 = 0.8$, $\phi_2 = 0.01$. Other parameters as in Table 2.1.

The mechanism for the gradual decay of V_1 spike amplitudes in the three timescale system was explained in Section 2.2.2 (Figures 2.10, 2.11) and depends on the fact that trajectories closely follow the V_2 -dependent V_1 -nullclines in the projection onto (V_1, w_1) -space in between fast jumps

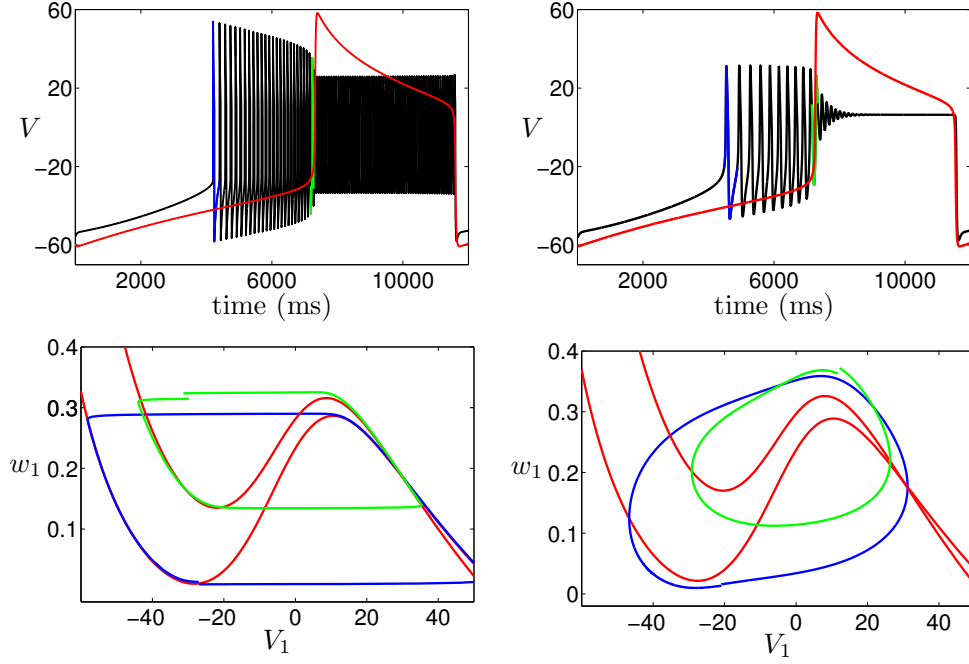


Figure 2.17: Upper row: Time courses of V_2 (red) and V_1 (black/blue/green) for $C_1 = 0.8$ (left) and $C_1 = 80$ (right), which reduces the amplitude modulation during the period when V_1 is spiking and V_2 is still depressed; $\phi_1 = 0.01$ and $\phi_2 = 0.0001$ in both cases. Bottom row: Projections to the (V_1, w_1) phase plane of the parts of the solutions colored blue and green in the upper row, along with V_1 -nullclines computed with V_2 fixed at the value attained by the V_2 time series at the start of the corresponding segment of the time series: $V_2 = -41.94$ (left, lower red curve), -26.00 (left, upper red curve), -40.23 (right, lower red curve), and -18.84 (right, upper red curve). Flow is counterclockwise. Note that for $C_1 = 0.8$ (left), the orbits adhere very closely to the nullclines in the silent and active phases and the maximal V_1 drops significantly between the cycles shown. For $C_1 = 80$ (right), the orbits deviate from the nullclines much more and the difference in maximal V_1 values, even between the first and last spikes of the burst, is significantly smaller.

in V_1 . Equivalently, in the projection onto (V_1, W_1, V_2) -space, V_2 has a strong effect on the shape of \mathcal{M}_s , which trajectories follow between these fast jumps. In the (3S, 1SS) scaling, however, \mathcal{M}_s no longer plays a role and the oscillations in the projection to (V_1, w_1) pull away from the

V_1 -nullclines and lose their relaxation character. As a result, the V_1 amplitude becomes less varied across spikes (Figure 2.17, top row). This effect persists across all g_{syn} values that yield V_1 spiking before V_2 jumps up in the (3S, 1SS) system.

Figure 2.18 shows the attracting solution for the (3S, 1SS) case projected onto (V_1, V_2, w_2) -space. On the lower right of this figure, the trajectory follows an attracting branch of \mathcal{M}_{ss} with low V_1 and V_2 . When the trajectory reaches the fold where this branch ends, slow oscillations of V_1 begin, but V_2 remains slaved to w_2 , evolving on the super slow timescale, until a fold of the V_2 -nullcline in the projection onto (V_2, w_2) -space is reached (although this projection is not shown, the fold is indicated by the green circle in Figure 2.18) and the slow transition to the next phase of the solution, with V_2 elevated, occurs. In the (3S, 1SS) regime, the branch of \mathcal{M}_{ss} to the left of the blue circle is stable with respect to the three-dimensional slow system, and when the trajectory jumps up from the fold of the V_2 -nullcline, it converges with damped oscillations in V_1 to this branch. This stability contrasts with the instability of \mathcal{M}_{ss} for the (1F, 2S, 1SS) system with $g_{syn} = 4.1$, which corresponds to the instability of the critical points of the v_2 -frozen system (2.19) with elevated v_2 since V_2 is slaved to the superslow flow of w_2 during the relevant solution segment in the (1F, 2S, 1SS) case. Thus, the grouping of timescales can significantly alter the behavior of V_1 and w_1 in the regime where V_2 is elevated for $g_{syn} = 4.1$. After the damped V_1 oscillations, the trajectory jumps from a fold of \mathcal{M}_{ss} (blue circle) back to the attracting branch of \mathcal{M}_{ss} at low V_1 and V_2 (Figure 2.18) and another solution cycle begins.

Under rescaling to a (1F, 3S) system, a different type of trajectory is observed (Figure 2.16, bottom). The solution exhibits prolonged V_2 spikes as in the (1F, 3S) case with $g_{syn} = 1.0$ (Figure 2.15), but there are now multiple V_1 spikes per cycle because the trajectory can jump up from \mathcal{M}_s^l with smaller V_2 than it could with $g_{syn} = 1.0$. The solution is quite different from that of the (1F, 2S, 1SS) system, lacking the rapid V_1 spikes and the transition from decrementing to constant amplitude spikes seen for (1F, 2S, 1SS) (Figure 2.17, top left).

In summary, neither of these two timescale systems captures the full features of the oscillating solution generated by (2.1) with $g_{syn} = 4.1$. The three timescale system has distinctive solutions with two groups of rapid V_1 spikes per cycle, one with decrementing amplitude and one with constant amplitude, but neither of the rescaled systems has solutions with both types of V_1 spikes. We therefore conclude that the solution shown in the second panel of Figure 2.2 represents an

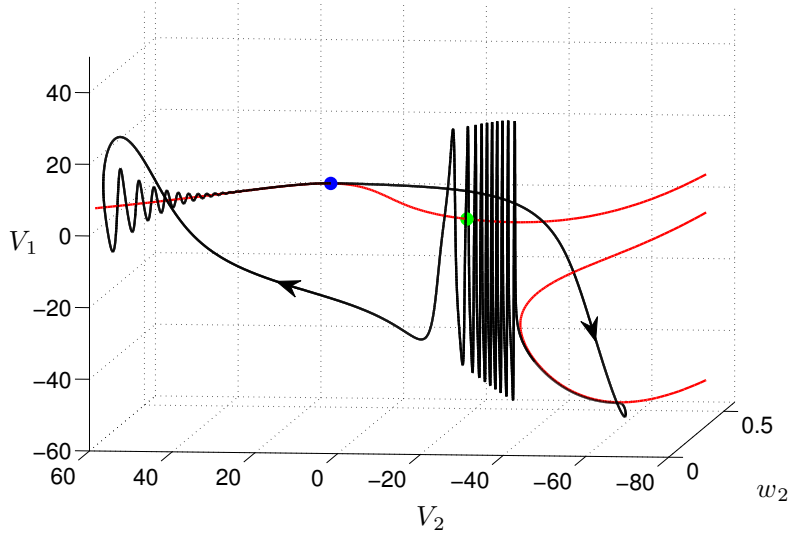


Figure 2.18: Projection of the attracting solution (black curve) of the (3S, 1SS) system with $g_{syn} = 4.1$, $C_1 = 80$, $\phi_2 = 0.0001$ onto (V_1, V_2, w_2) -space. Red curves denote \mathcal{M}_{ss} , and blue and green circles mark two folds of \mathcal{M}_{ss} .

intrinsically three timescale phenomenon.

2.3.3 $g_{syn} = 5.1$: direct transition to a depolarized plateau

When the timescale separation is exaggerated in the (1F, 2S, 1SS) system with $g_{syn} = 5.1$, the qualitative form of the solution, shown in Figure 2.2, does not change, nor does the relevance of the mechanisms shown in Figures 2.12-2.13. In particular, the V_1 time series includes a group of rapid spikes with decrementing amplitudes, followed by a depolarized plateau.

A time series obtained after rescaling to a (3S, 1SS) system with $g_{syn} = 5.1$ is shown in Figure 2.19 (top panel). As with $g_{syn} = 4.1$, this rescaling eliminates the gradual decrease of V_1 spike amplitudes, again due to the loss of relevance of \mathcal{M}_s or, equivalently, the loss of relaxation oscillator character in the (V_1, w_1) oscillations; by similar arguments, varying g_{syn} away from 5.1 cannot restore this property. A second, subtle change is that the transition from large V_1 spikes to a V_1 plateau features a gradual damping in the two timescale case, evident during the abrupt

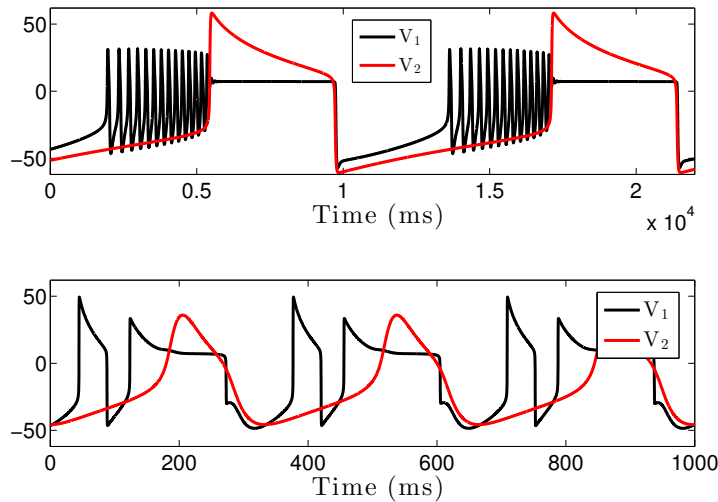


Figure 2.19: Time series of (2.1) with $g_{syn} = 5.1$. Top: (3S, 1SS) case corresponding to the choice $C_1 = 80$, $\phi_2 = 0.0001$; Bottom: (1F, 3S) case, with $C_1 = 0.8$, $\phi_2 = 0.01$. Other parameters as in Table 2.1.

increase in V_2 , that is absent with three timescales. Recall that in the (1F, 2S, 1SS) case, this transition occurs while the orbit is following a solution segment of the two-dimensional slow layer problem. Linearization of this problem about the equilibrium point to which the solution segment converges, on \mathcal{M}_{ss} , yields a matrix with eigenvalues that can be shown to be real and negative for the (1F, 2S, 1SS) system; hence, the slow layer solution converges without damped oscillations to this equilibrium point. The situation is different in the (3S, 1SS) case. The solution segment during the V_2 jump is described by a solution of a three-dimensional slow layer problem. A calculation shows that the matrix obtained by linearizing this slow layer system about its equilibrium point on \mathcal{M}_{ss} has eigenvalues of negative real part, but these can be complex. Thus, a possibility arises for subthreshold oscillations, and we observe these numerically for $g_{syn} = 5.1$ and other nearby values.

In the (1F, 3S) regime (Figure 2.19, bottom panel), the solution with $g_{syn} = 5.1$ is qualitatively similar to that obtained in the (1F, 3S) scaling with $g_{syn} = 4.1$, with similar mechanisms involved.

In particular, there is no convergence to an equilibrium point of a slow system (i.e., a point on \mathcal{M}_{ss}) during the active phase but instead an increase and decrease in all three slow variables, w_1, V_2, w_2 . The V_1 time course is determined by the path of the slow system solution along \mathcal{M}_s , showing a gradual, non-monotonic decay as V_2 increases that is quite distinct from the abrupt transition from spiking to plateau arising with three timescales.

In summary, the attracting solution of the (1F, 2S, 1SS) system with $g_{syn} = 5.1$ has two distinguishing features: a phase of rapid V_1 spikes of decrementing amplitudes and an abrupt transition to a depolarised plateau. The first of these is lost in both two timescale versions of the system that we considered. The second may in principle occur with a rescaling to (3S, 1SS), but is lost in the parameter regime we use; instead, subthreshold oscillations are seen during the transition. However, the effect is visually rather subtle and thus may not be relevant to efforts to model experimental data. Based on the spike amplitude modulation, at least, we can still conclude that the solution shown in Figure 2.2 with $g_{syn} = 5.1$ is an intrinsically three timescale phenomenon, but we acknowledge that the distinctiveness of the three timescale case is more limited than with the other g_{syn} values we discussed.

2.4 DISCUSSION

In this work, we have considered the dynamics of a model system with three timescales. This analysis has been done based on the ideas of fast-slow decomposition by considering the interaction of two potentially oscillating systems, i.e., one fast-slow and the other slow-superslow. This perspective is commonly used in the context of two timescale dynamical systems, and our work illustrates that it can be extended to the three timescale setting. Moreover, it complements the other perspective that involves concatenation of segments of solutions of various subsystems, i.e., reduced and layer problems well [41]. In particular, the concatenation method provides a clear view of how characteristics of trajectories relate to the features of slow and superslow manifolds and their folds, while the coupled oscillator approach helps elucidate how these manifold features arise. For $g_{syn} = 4.1$, for example, considering how nullclines of one oscillator respond to changes in another oscillator gives insight into the evolution of solution features (e.g., spike amplitudes)

over time. We hope that these insights will guide other researchers undertaking similar analyses related to their problems of interest.

Additionally, our analysis yields several insights. First, the fast-slow decomposition methods developed for two timescale systems do extend naturally to three timescale settings, and it is clear that this extension would carry over similarly to systems with more than three timescales as well. Second, there are natural mechanisms for transitions directly from superslow to fast dynamics, yet we generically do not expect transitions directly from fast to superslow, as these would require fast layer problem solutions to asymptote to limits that happen to be equilibria of certain slow systems as well. Besides superslow to fast transitions, we also observe transitions from superslow dynamics to fast-slow relaxation oscillations in some variables with continued superslow drift in others. This finding highlights a need for an averaging result for the three timescale setting, like the one that justifies use of a slow averaged system in a two timescale context when solutions combine fast oscillations and slow drift. Third, there is a limitation to the utility of frozen systems for the analysis of coupled oscillator systems; full system dynamics can have features not predicted from bifurcation analysis based on frozen systems, as we see with $g_{syn} = 1.0$.

While parts of this work investigate rather specific details of solution features, we have followed our descriptive analysis with an investigation of which solution features are truly three timescale phenomena. Identifying solution features that require three timescales provides useful information for modeling studies, where a determination needs to be made about how many timescales to include in a model to represent some given experimental data. In fact, many of the solution features that we observe are lost under grouping to two timescales and hence can be said to require three timescales, at least in the system we have studied. This finding suggests that classifying disparate timescales into two groups should no longer be a default approach in modeling work. We also note that choices about how to group timescales determine the dimensionality of various subsystems that come into play, and the dimension of a subsystem constrains the types of solutions it can support; certain solution features will therefore only be observed in certain timescale groupings. In an arbitrary multiple timescale system, the number of timescales exhibited by a particular solution need not be as large as the number of distinct timescales in the system as a whole. An example occurs in system (2.1) for small g_{syn} ; in this case, v_1 stays relatively steady and does not spike, so the fast timescale is not observed in the attracting solution for the system. Hence, three

timescale effects can be destroyed in our system by decreasing g_{syn} . However, since the (v_2, w_2) system decouples, there will always be slow and superslow components to solutions and, once g_{syn} is large enough that v_1 becomes active, three timescales will be manifest in solutions. Thus, while it is generally the case that three timescale effects can be removed by varying a system parameter rather than by changing the timescale separation as we have done in this article, this possibility is not of interest in our system.

Ours is not the first work to provide mathematical analysis of a three timescale system. Several papers in this area have focused on mixed-mode oscillations (MMOs) supported by three timescales. The initial approach was to consider a three-dimensional system where the right hand sides were $\mathcal{O}(1)$, $\mathcal{O}(\epsilon)$, $\mathcal{O}(\epsilon^2)$, respectively [34]; MMOs were shown to emerge through an effect analogous to a slow drift through a canard explosion. Certain higher dimensional systems were also shown to reduce to similar three-dimensional systems with the same structure [48], [29]; see also [39].

The paper closest to ours is [35], which also considers two coupled systems, one fast-slow and one slow-superslow, with unidirectional coupling such that the slow-superslow oscillator forces the fast-slow system. Some similar features are seen in solutions to our model and those from [35], including periods of rapid oscillation of relaxation type (called the pulsatile phase in [35]) and segments where all variables are changing on the superslow timescale (occurring within the surge phase in [35]). However, in [35], the slow variable from the slow-superslow oscillator appears in the slow equation of the fast-slow oscillator, rather than in the fast equation as in our model. An important consequence is that while our model can exhibit amplitude modulation during the fast spiking phase (as in, for instance, the upper right and lower panels of Figure 2.2) because the position and shape of the nullcline for the fast variable is modified by the coupling term, this effect is absent in the model of [35] where the coupling moves the relative positions of the nullclines but does not alter their shape. The focus in [35] is also somewhat different to ours; they are interested in determining the dynamical mechanisms for the MMOs found in their system whereas we have concentrated on identifying features of the dynamics that are truly three timescale phenomena. We note that MMOs are likely to occur in our system in certain parameter regimes, but we have not looked for them.

Ha and Kuznetsov [23] also considered a three timescale model, describing the interactions

of voltage and calcium concentration in a neuronal soma linked with a neuronal dendrite. Their work focused on mechanisms leading to two different types of oscillations, one involving the fast and intermediate timescales and another based on fast and slow components, rather than solution features emerging from the concurrent interaction of all three timescales. A recent paper by Vo et al. [77] considered solutions of a four-dimensional, three timescale model of electrical activity and calcium signaling in a pituitary lactotroph, focussing on solutions such as MMOs that can appear in systems with two timescales. The authors considered the effect of grouping the timescales into two groups in two different ways and showed that the dynamics of these rescaled models could be understood as different unfoldings of the full three timescale system. The two two-scale approaches were compared, were shown to provide different insights, and were unified via a fully three timescale representation, but little consideration was given to identifying dynamic features that are specifically three timescale phenomena, as we do. Franci et al. [21] considered bursting in conductance-based models of neurons and proposed a three timescale ‘normal form’ for the phenomenon. The focus was on explaining how observed bursting behaviour might arise in unfoldings of the normal form, rather than on identifying phenomena that are intrinsically three timescale. Indeed, many earlier analyses of bursting behaviour have shown that only two timescales are needed in order to observe bursting solutions, and the work of [21] shows how previously observed two timescale bursters might be transformed into one another by superslow variation of system parameters. Other models with three timescales have been discussed in the recent literature (see, e.g., [24, 25, 36]) but, again, the analysis presented arises mostly from grouping the timescales into two groups and there is little insight into intrinsically three timescale phenomena.

In the emerging study of systems with more than two timescales, there are many directions for future work, even without considering complications such as stochasticity, forcing, or delays. As in other earlier work (e.g., [35]), we have considered a specific form of coupling such that our model system can be thought of as one oscillator forcing another. Preliminary investigations suggest that in the scenarios we have considered, the inclusion of bidirectional coupling has surprisingly little influence on solution features. Nonetheless, there are many variations on the coupling among timescales that arise in other model systems and should be considered in future work. The consideration of bidirectional coupling is likely to be particularly important for understanding the dynamics of our main motivating example, the oscillatory dynamics of neurons, where mem-

brane potential and cytoplasmic Ca^{2+} concentration can each influence the evolution of the other. Note also that our ML models were tuned individually to be Type I oscillators, with an onset of oscillations through a SNIC bifurcation under variation of the applied current parameter I_i , yet the coupling nonetheless induced oscillations in (V_1, w_1) via an AH bifurcation with respect to changes in V_2 . This effect would not change with intrinsically Type II oscillators, so we expect little difference there relative to what we have considered, but this expectation still remains to be confirmed.

From a more theoretical point of view, there is much work to be done to explore folded singularities that can arise and affect solutions in systems with three or more timescales. In the solutions that we considered, trajectories pass close to folded singularities yet these play little role in the resulting dynamics. This is unlikely to always be the case, however (see also [77]), and a comprehensive theory of folded singularities in systems with more than two timescales is needed. There are also many other forms of dynamics that one could consider that are outside the coupled oscillator framework altogether, and these will likely yield a variety of three timescale phenomena beyond those that we have identified.

3.0 MULTIPLE TIMESCALE MIXED BURSTING DYNAMICS IN A RESPIRATORY NEURON MODEL

Certain neurons in the pre-Bötzinger complex (pre-BötC) of the mammalian brainstem exhibit bursting activity in the inspiratory phase of respiration, which has been extensively studied both experimentally and computationally. Two distinct bursting mechanisms have been identified in the pre-BötC, depending on the persistent sodium current (I_{NaP}) or a nonspecific cation current (I_{CAN}) activated by intracellular Ca^{2+} , respectively. Motivated by experimental results, Toporikova and Butera [73] developed a two-compartment conductance-based model (TB model) that encompasses both burst mechanisms, which was then reduced by Park and Rubin [47] to a single-compartment model of a pre-BötC inspiratory neuron featuring both NaP and CAN currents, as well as intracellular calcium oscillations that activate the CAN current. The dynamics of this model is given by the following equations:

$$(3.1a) \quad C_m \frac{dV}{dt} = -g_L(V - V_L) - g_K n^4(V - V_K) - g_{\text{Na}} m_\infty^3(V)(1 - n)(V - V_{\text{Na}}) \\ - g_{\text{NaP}} m p_\infty(V) h(V - V_{\text{Na}}) - g_{\text{CAN}} f([\text{Ca}]) (V - V_{\text{Na}})$$

$$(3.1b) \quad \frac{dn}{dt} = (n_\infty(V) - n) / \tau_n(V)$$

$$(3.1c) \quad \frac{dh}{dt} = (h_\infty(V) - h) / \tau_h(V)$$

$$(3.1d) \quad \frac{d[\text{Ca}]}{dt} = K_{\text{Ca}} (J_{\text{ERIN}} - J_{\text{EROUT}})$$

$$(3.1e) \quad \frac{dl}{dt} = AK_d(1 - l) - A[\text{Ca}]l$$

with

$$(3.2a) \quad x_\infty(V) = 1/(1 + \exp((V - \theta_x)/\sigma_x)), \quad x \in \{m, mp, n, h\}$$

$$(3.2b) \quad \tau_x(V) = \bar{\tau}_x/\cosh((V - \theta_x)/2\sigma_x), \quad x \in \{n, h\}$$

$$(3.2c) \quad f([\text{Ca}]) = 1/(1 + (K_{\text{CAN}}/[\text{Ca}])^{n_{\text{CAN}}})$$

$$(3.2d) \quad J_{\text{ERIN}} = \left(L_{\text{IP}_3} + P_{\text{IP}_3} \left[\frac{[\text{IP}_3][\text{Ca}]l}{([\text{IP}_3] + K_I)([\text{Ca}] + K_a)} \right]^3 \right) ([\text{Ca}]_{\text{ER}} - [\text{Ca}])$$

$$(3.2e) \quad J_{\text{EROUT}} = V_{\text{SERCA}} \frac{[\text{Ca}]^2}{K_{\text{SERCA}}^2 + [\text{Ca}]^2}$$

$$(3.2f) \quad [\text{Ca}]_{\text{ER}} = \frac{[\text{Ca}]_{\text{Tot}} - [\text{Ca}]}{\sigma}.$$

Default parameter values and corresponding units for this system are given in Table 3.1. We refer to the system of equations (3.1a)-(3.1e) as the *mixed bursting model*. Following the terminology used in [47], we call the system of equations (3.1a)-(3.1c) the *somatic subsystem* and the system of equations (3.1d)-(3.1e) the *dendritic subsystem*. Analysis of the somatic subsystem can be performed by treating the variable h as a bifurcation parameter for the other, fast model equations (3.1a), (3.1b) (Figure 3.1A). The resulting bifurcation diagram includes an S-shaped curve of equilibria (S) and a family of stable periodic orbits (P) that initiates in a homoclinic (HC) bifurcation involving the middle branch of S and terminates, as h is increased, in a saddle-node of periodic orbits (SNPO) bifurcation where it coalesces with a second family of unstable periodic solutions that is born in a subcritical Andronov-Hopf (AH) bifurcation. To first approximation, the mixed bursting model exhibits quiescence if the h -nullcline intersects S on its lower branch; square-wave bursting if the intersection point lies in the middle branch of S yet below the homoclinic point; or tonic spiking if the fixed point lies above the homoclinic point [53], and hence the somatic subsystem constitutes a conditional square-wave bursting model. The location of this intersection depends on the tuning of parameters (e.g. g_{NaP} , g_{ton}).

In the full system, intracellular calcium dynamics is confined to the dendritic subsystem and evolves independently from somatic activity patterns. More specifically, in the dendritic subsystem, the dynamics of Ca^{2+} is governed by the intracellular Ca^{2+} concentration, $[\text{Ca}]$, and the IP_3 channel gating variable, l . This subsystem acts as a relaxation oscillator, where the nullcline of

Table 3.1: The values of the parameters in the pre-BötC model given by equations (3.1) and (3.2)

Parameter values							
C_m	21 pF	g_{Na}	28 nS	σ_h	5 mV	L_{IP_3}	$0.37 \text{ pL} \cdot \text{ms}^{-1}$
V_{Na}	50 mV	g_K	11.2 nS	$\bar{\tau}_n$	10 ms	P_{IP_3}	$31,000 \text{ pL} \cdot \text{ms}^{-1}$
V_K	-85 mV	g_L	11.2 nS	$\bar{\tau}_h$	10,000 ms	K_I	$1.0 \mu\text{M}$
V_L	-58 mV	g_{NaP}	1 nS	K_{CAN}	$0.74 \mu\text{M}$	K_a	$0.4 \mu\text{M}$
θ_m	-34 mV	g_{CAN}	0.7 nS	n_{CAN}	0.97	V_{SERCA}	$400 \text{ aMol} \cdot \text{ms}^{-1}$
θ_n	-29 mV	σ_m	-5 mV	$[IP_3]$	$0.95 \mu\text{M}$	K_{SERCA}	$0.2 \mu\text{M}$
θ_{mp}	-40 mV	σ_n	-4 mV	$[Ca]_{Tot}$	$1.25 \mu\text{M}$	A	$0.005 \mu\text{M}^{-1} \cdot \text{ms}^{-1}$
θ_h	-48 mV	σ_{mp}	-6 mV	K_{Ca}	0.000025 pL^{-1}	K_d	$0.4 \mu\text{M}$
σ	0.185						

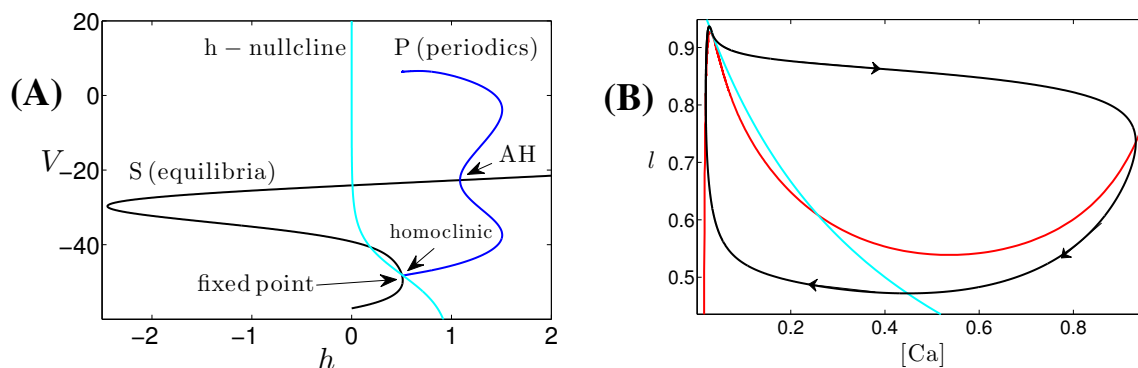


Figure 3.1: Basic structures of the two subsystems (3.1a)-(3.1c) and (3.1d)-(3.1e) with parameter values as given in Table 3.1 but without coupling. (A): Projection onto (h, V) -space of the bifurcation diagram for the somatic subsystem along with the h -nullcline shown in cyan. The curve S (black) denotes the fixed points of the equations (3.1a)-(3.1b) with h taken as a constant parameter, and the blue curve shows the maximum and minimum V along the family of periodics (P). (B): Nullclines of $[Ca]$ (red) and l (cyan) for the dendritic subsystem (3.1d)-(3.1e). The attracting periodic orbit for this subsystem is shown in black.

$[Ca]$ is a cubic curve and that of l is sigmoidal (Figure 3.1B). The dynamics of $([Ca], l)$ affects the dynamics of (V, n, h) ; the parameter g_{CAN} controls the coupling strength.

Similarly to the TB model [73], this model can produce two types of intrinsic bursting behav-

iors, depending on chosen parameter values. One type of bursting (*somatic bursting*) depends on persistent sodium current inactivation, whereas the other type (dendritic bursting) relies on intracellular Ca^{2+} . $[\text{IP}_3]$ and g_{NaP} are two critical parameters that can be used to switch the bursting mechanism from one type to the other [47, 73]. Specifically, the level of $[\text{IP}_3]$ determines whether the $([\text{Ca}], l)$ system exhibits a stable steady state or a stable periodic orbit, while $[\text{Ca}]$ and g_{NaP} both affect the shape of the bifurcation diagram of the somatic subsystem. In the two extreme cases, bursting is driven by either somatic membrane properties or Ca^{2+} oscillations alone. However, in some region of $(g_{\text{NaP}}, [\text{IP}_3])$ parameter space, these mechanisms interact to produce a hybrid bursting pattern called *somato-dendritic bursting*. Figure 3.2 shows the three types of bursting.

One of the most interesting somato-dendritic bursting solution patterns presented in [47] is generated when $[\text{IP}_3] = 0.95$ and $g_{\text{NaP}} = 2$ (Figure 3.2, bottom panel). This pattern consists of long bursts separated by sequences of short bursts and is observed experimentally [14]. For convenience, we refer to such solutions as *mixed bursting* (MB) solutions. Numerical simulations show that MB solutions are quite sensitive to changes of values of parameters such as $[\text{IP}_3]$ and g_{NaP} , to changes of timescale parameters, and to changes in timescale separation.

Since a regular bursting solution requires at least two timescales, it is natural to expect that MB solutions, which involve a temporal progression of bursts, might need a third timescale. In this chapter, we aim to better understand the mechanisms underlying the dynamics of the MB solution [47] and to determine what mix of timescales is involved in generating this solution. More generally, we seek to analyze what combinations of timescales can support MB solutions and whether the mixed bursting model can be tuned to make the MB solution more robust, corresponding to the fact that is seen in experiments [14]. With this goal, we will nondimensionalize to reveal the presence of different timescales; determine how to group the timescales that are present (in particular, whether to use two or three classes); use geometric singular perturbation theory to set up reduced systems based on separation of timescales; and use the reduced systems to explain the mechanisms underlying the dynamics of MB solutions.

By uncovering the mechanisms underlying the MB solution pattern in the mixed bursting model, we deduce what combination of timescales can generally support MB solutions and conclude that a third timescale is not required to generate MB solutions in this model. In the course of our analysis, we also attain important insights into how the mixed bursting model can be tuned to

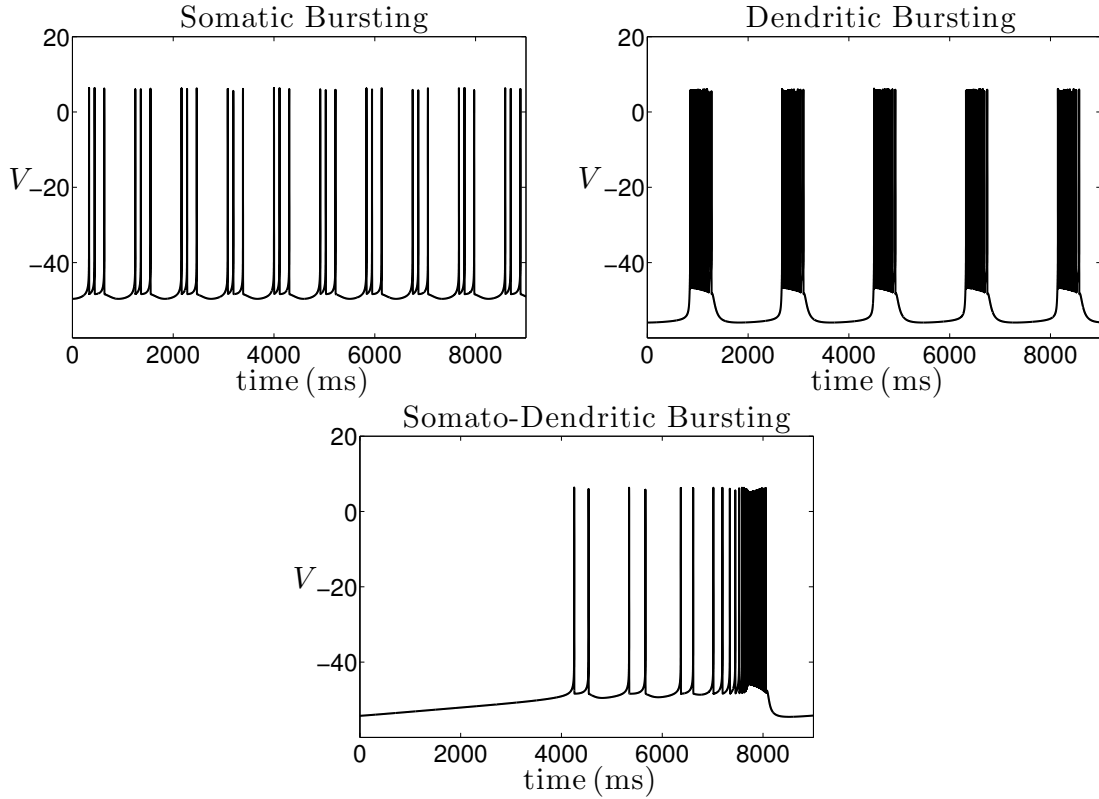


Figure 3.2: Time series for bursting solutions of the full system (3.1)-(3.2). This model produces somatic bursting (shown for $[IP_3] = 0.9$ and $g_{NaP} = 2.5$), dendritic bursting ($[IP_3] = 1.2$ and $g_{NaP} = 1$), and one cycle of somato-dendritic bursting ($[IP_3] = 0.95$ and $g_{NaP} = 2$), with other parameter values as in Table 3.1; all patterns repeat periodically.

make MB solutions more robust.

3.1 ANALYSIS OF THE MIXED BURSTING MODEL

Henceforth, we set $[IP_3] = 1$ and $A = 0.001$ (see Appendix Section 6.2 for a detailed analysis of relevant timescales) so that the the dendritic subsystem acts as a standard relaxation oscillator, with simple nullcline interactions. The dendritic subsystem generates relaxation oscillations involving

jumps in $[Ca]$ between branches of the $[Ca]$ -nullcline alternating with drift in $([Ca], l)$ along these branches (Figure 3.3); the $[Ca]$ -jumps are fast relative to the drift. Under this new choice of parameter values, there is a clear separation of timescales between V (fast), $[Ca]$ (slow) and l (superslow). To apply standard tools of geometric singular perturbation theory, we also need a clear separation of timescales between n , h and the other variables. However, this separation is lacking, since the rate factors multiplying the equations for the gating variables depend on the voltage. Until we resolve this issue, we temporarily group n as a fast variable and h as a slow variable, as has been suggested in past studies of the Butera model, such as [2].

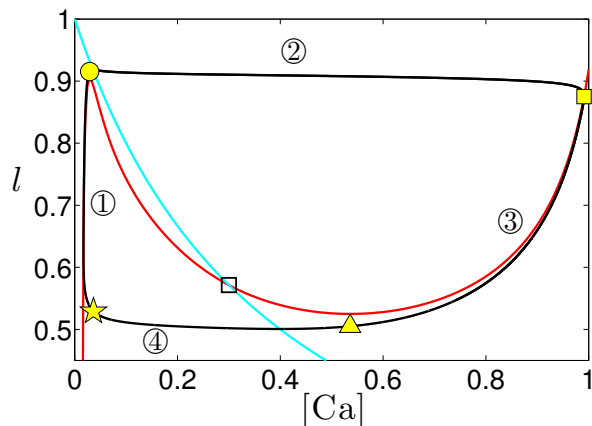


Figure 3.3: Attracting dynamics in $([Ca], l)$ -space, with parameter values given in Table 3.1 except $[IP_3] = 1$ and $A = 0.001$. The red curve is the $[Ca]$ -nullcline and the cyan curve is the l -nullcline. The hollow square denotes the equilibrium solution, which is a source. The attracting periodic orbit for the dendritic subsystem is shown in black (with clockwise flow passing through the numbered regions in increasing order). Yellow symbols mark key points along the solution trajectory (star: start of phase ①; circle: start of phase ②; square: start of phase ③; triangle: start of phase ④).

To explain the mechanisms underlying the dynamics of the mixed bursting model (3.1), we link various two-dimensional projections, each corresponding either to a bifurcation diagram with respect to some parameter or to the phase plane of one oscillator. Since $([Ca], l)$ oscillates independently of (V, n, h) , it is useful to consider the system from the perspective of a fast-slow system driven by a slow-superslow oscillation (cf. [41]). There are three slow/superslow variables,

h , $[\text{Ca}]$, l , in the full system. Changes in l affect the somatic subsystem (3.1a)-(3.1c) indirectly, through the coupling between $[\text{Ca}]$ and l and the coupling of $[\text{Ca}]$ to V , but not directly. Thus, if we treat all slow or superslow variables as bifurcation parameters, then it is sufficient to consider only h and $[\text{Ca}]$ when studying the dynamics of the somatic subsystem [47]. With these two parameters, it is convenient to treat h as a bifurcation parameter for the geometric analysis of the somatic subsystem and to consider the effect of $[\text{Ca}]$ on the resulting bifurcation diagram. Instead of using $[\text{Ca}]$ directly, we follow [47] and choose $g_{\text{CAN}_{\text{Tot}}} = g_{\text{CAN}}f([\text{Ca}])$ as a bifurcation parameter, where $f([\text{Ca}])$ is the concave down and monotonically increasing function of $[\text{Ca}]$ given in equation (3.2c). Before we actually implement the analysis, however, we will perform some helpful pre-processing of the equations.

3.1.1 Rescaling and simplification of timescales

Our analysis will depend heavily on exploiting the presence of different timescales. As a first step, it is helpful to rescale the variables so that the important timescales can be explicitly identified. To this end, we define new dimensionless variables (v , c , τ), and voltage, calcium and timescales Q_v , Q_c and Q_t , respectively, such that:

$$(3.3) \quad V = Q_v \cdot v, \quad [\text{Ca}] = Q_c \cdot c, \quad t = Q_t \cdot \tau.$$

Note that n , h and l are already dimensionless in (3.1).

Details of the nondimensionalization procedure, including the determination of appropriate values for Q_v , Q_c and Q_t , are given in Appendix Section 6.3. From this process, we obtain a dimensionless system of the form

$$(3.4a) \quad R_v \frac{dv}{d\tau} = f_1(v, n, h, c)$$

$$(3.4b) \quad R_n \frac{dn}{d\tau} = g_1(v, n)/t_n(v)$$

$$(3.4c) \quad R_h \frac{dh}{d\tau} = h_1(v, h)/t_h(v)$$

$$(3.4d) \quad R_c \frac{dc}{d\tau} = f_2(c, l)$$

$$(3.4e) \quad R_l \frac{dl}{d\tau} = g_2(c, l)$$

with parameters R_v , R_n , R_h , R_c and R_l given in (6.6), where the functions f_1 , f_2 , g_1 , g_2 , h_1 , t_n and t_h are specified in (6.7) in Appendix 6.3. All right hand side functions are of size $O(1)$, except $1/t_n$ and $1/t_h$, which are bounded by 1. We use the notation O to denote an order of magnitude estimate: $x \sim O(10^n)$, where n is the nearest integer to $\log(x)$. The parameter values given in Table 3.1 and the modified $A = 0.001$ yield $R_v \sim O(1)$, $R_c \sim O(10)$ and $R_l \sim O(1000)$.

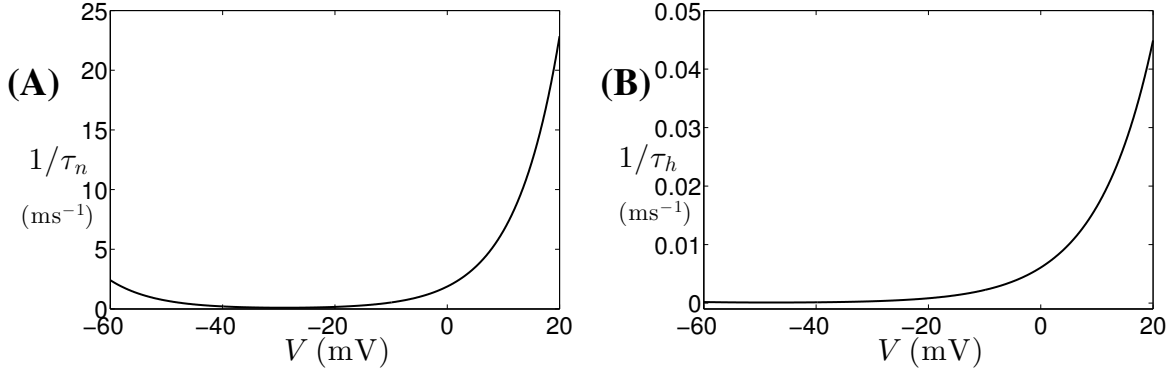


Figure 3.4: Functions (A) $1/\tau_n(V)$ and (B) $1/\tau_h(V)$. Note the difference in vertical scales between panels.

To obtain $R_x = \frac{1}{Q_t T_x}$ for $x \in \{n, h\}$ in Appendix 6.3, we followed the standard procedure of defining scaling factors $T_x = \max(1/\tau_x(V))$, where $\tau_x(V)$ appears in system (3.1). These factors turn out to be problematic, however, because both $1/\tau_n(V)$ and $1/\tau_h(V)$ depend heavily on voltage. Specifically, Figure 3.4 shows the plots of $1/\tau_n(V)$ and $1/\tau_h(V)$ over the range $V \in [-60, 20]$. This figure indicates that $1/\tau_n(V)$ varies from about 0.1 ms^{-1} to about 20 ms^{-1} and

$1/\tau_h(V)$ varies from about 0.0001 ms^{-1} to about 0.04 ms^{-1} . From the definition of T_x , we then obtain $T_n \approx 20 \text{ ms}^{-1}$ and $T_h \approx 0.04 \text{ ms}^{-1}$. As a result, the terms $1/t_x(V) =: \frac{1/\tau_x(V)}{T_x}$ appearing on the right hand sides of the n and h equations in (3.4) vary from $O(0.001)$ to $O(1)$. However, nondimensionlization requires the right hand sides to be $O(1)$. Therefore, the quantities R_n and R_h , based on T_n and T_h , respectively, cannot capture the timescales for n and h . In other words, because the evolution rates of n and h depend on voltage $V(t)$, these variables will have different timescales at different phases within a solution. As a first step in addressing this issue, we temporally reduce the reliance of the timescales of n and h on voltage by setting the two functions $\tau_h(V)$, $\tau_n(V)$ in (3.1) to be constants, τ_h , τ_n , respectively. As a result, we obtain the following dimensionless mixed bursting model, which we call the constant- τ model:

$$(3.5a) \quad R_v \frac{dv}{d\tau} = f_1(v, n, h, c)$$

$$(3.5b) \quad R_n \frac{dn}{d\tau} = g_1(v_1, n)$$

$$(3.5c) \quad R_h \frac{dh}{d\tau} = h_1(v_1, h)$$

$$(3.5d) \quad R_c \frac{dc}{d\tau} = f_2(c, l)$$

$$(3.5e) \quad R_l \frac{dl}{d\tau} = g_2(c, l)$$

with relative rates of all variables:

$$(3.6a) \quad R_v = O(1), \quad R_x = \frac{\tau_x}{Q_t} = O(\tau_x), \quad x \in \{n, h\}$$

$$(3.6b) \quad R_c = O(10), \quad R_l = O(1000).$$

from which we conclude that v evolves on a fast timescale, c evolves on a slow timescale, and l evolves on a superslow timescale for the baseline parameter values, although the values R_v , R_c and R_l can be varied by changing C_m , K_{Ca} and A , respectively, as shown in (6.6) in Appendix 6.3. The constants τ_n and τ_h appearing in (3.6a), which control the timescales for n and h , will need to be determined. As noted earlier, to analyze the dynamics of (3.5), our approach is to treat h as a bifurcation parameter for the geometric analysis of the somatic subsystem (3.5a)-(3.5b) and consider the effect of the dendritic system (c, l) on the resulting bifurcation diagram. In the following, we will first determine what timescales for n and h , controlled by τ_n and τ_h , are needed

for (3.5) to generate an MB solution, while other timescales are as specified in (3.6); second, we will ascertain which timescales can be combined without losing the qualitative features of MB solutions; and third, we will deduce what combinations of timescales can support MB solutions in general. For convenience, we henceforth omit units of parameter values.

3.1.2 Dynamics of the constant- τ model (3.5)

Based on simulations of (3.5) over a range of τ_n and τ_h values, we find that under the choice $\tau_n = 5$ and $\tau_h = 1000$, (3.5) yields an MB solution, the time series of which is shown in Figure 3.5A. In this case, h evolves on a superslow timescale, comparable to l .

As a first step of analyzing such MB patterns, we investigate the coupling effect in (3.5). When $g_{\text{can}} = 0$, the constant- τ model decouples into two systems, each of which has a multiple-timescale structure. For the parameter values we have chosen, the bifurcation structure and the nullclines for the uncoupled systems are qualitatively as shown in Figure 3.1. Since the coupling in our system is unidirectional, the oscillations in (c, l) are independent of g_{can} and of the dynamics of the (v, n, h) subsystem; they are standard relaxation oscillations consisting of a superslow excursion through the silent phase (Figure 3.3, ①), a slow jump away from the c -nullcline up to the active phase (Figure 3.3, ②), a superslow excursion through the active phase (Figure 3.3, ③), and a slow jump back to the silent phase (Figure 3.3, ④). In contrast, if $g_{\text{can}} > 0$, then the (v, n, h) subsystem depends on g_{can} and on the (c, l) oscillation. With the choice of $g_{\text{can}} = 0.7$, the constant- τ model can generate an MB solution. An example of the coupling effect can be seen in Figure 3.5B: the magenta (resp. blue) curve denotes the bifurcation diagram of the somatic subsystem that is obtained for c at 0.0171 (resp. 1) and we can see that as c increases, the bifurcation diagram will shift down and to the left.

In the following, we will first explain the mechanism underlying the small bursts in the MB solution ([53], [26]) and then elucidate how the transition to a long burst occurs, from the perspective of how the somatic subsystem is driven by the dendritic subsystem. The use of this kind of perspective has proved helpful in past analyses of various models with two timescales as well as of a three timescale model [41].

In Figure 3.5C, we project the first small burst solution and the bifurcation diagram of the

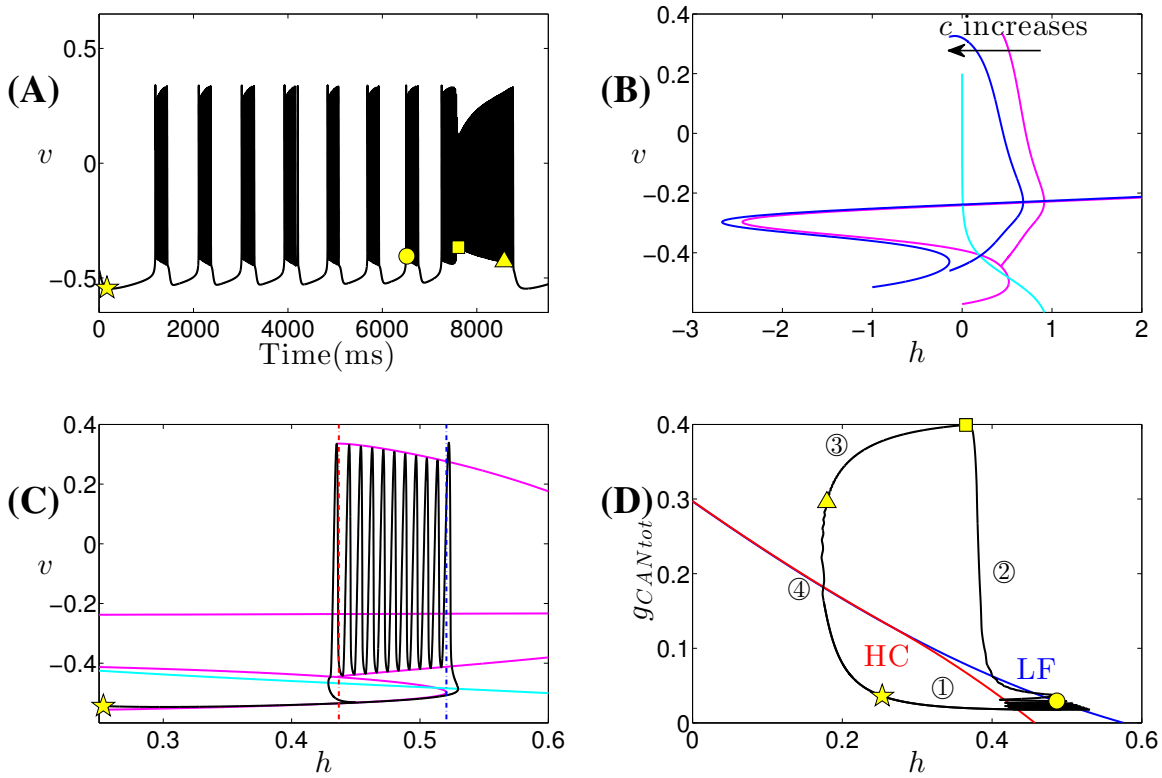


Figure 3.5: Simulation of the MB solution generated by (3.5), together with corresponding bifurcation diagrams, for $\tau_n = 5$, $\tau_h = 1000$, $[IP_3] = 1$, $A = 0.001$, and other parameter values as given in Table 3.1. Circled numbers and yellow symbols correspond to phases of the (c, l) oscillation and the points of transition between them, as shown in Figure 3.3. (A): Temporal evolution of v . (B): The effect of c on the bifurcation diagram for the (v, n) system, projected into (h, v) -space, along with the h -nullcline (cyan). Increasing c from 0.0171 to 1 results in a shift of the bifurcation diagram to the left (magenta to blue) and switches the homoclinic bifurcation to a SNIC. (C): Projection of the first small burst in the MB solution from (A) onto the bifurcation diagram (with $c = 0.0171$) in (h, v) -space, along with the h -nullcline (cyan). The blue and red dashed lines indicate the h values where the lower fold and homoclinic bifurcations occur, respectively. (D): Homoclinic bifurcation curve (red), the curve of saddle-node bifurcations corresponding to the lower fold of the bifurcation diagram (blue) and the trajectory (black) in $(h, g_{CAN_{Tot}})$ parameter space.

somatic subsystem for c fixed at 0.0171, corresponding to its value at the beginning of this first small burst (near the yellow star in Figure 3.5A), onto (h, v) -space. Also shown is the red (resp. blue) dashed line representing the h value at which the homoclinic (resp. saddle-node/ lower fold of equilibria) bifurcation occurs.

Nearly all small bursts happen in phase ①, during which c is slaved to l by the requirement that $f_2(c, l) = 0$ and thus evolves on a superslow timescale. Hence, during the first small burst period, which is relatively short, c only increases by a small amount. Notice that the coupling strength we have chosen is not strong, so the bifurcation diagram only depends weakly on c (Figure 3.5B). As a result, the bifurcation diagrams for c corresponding to the beginning and end of the first small burst lie extremely close to each other, which is why it suffices to consider the single bifurcation diagram for $c = 0.0171$ in Figure 3.5C. Starting from the yellow star, the trajectory moves on the superslow timescale associated with h along the stable lower branch of the bifurcation diagram until it reaches the lower fold. After that, the trajectory jumps up to the stable periodic orbit branch and then moves to the left, since the trajectory stays above the h -nullcline. After crossing the homoclinic bifurcation at the h value indicated by the red dashed line, the trajectory will jump down to the lower branch of equilibria, completing a small burst. Such square-wave bursting solutions will repeat until c jumps up near the yellow circle shown in Figures 3.3 and 3.5A.

Understanding of the persistence of the small bursts and the mechanism by which a transition to the long burst occurs requires us to consider the effect of c on the somatic subsystem. To do so, as noted before, we use $g_{\text{CAN}_{\text{Tot}}}$ as the second bifurcation parameter and allow both $g_{\text{CAN}_{\text{Tot}}}$ and h to vary and find the two-parameter bifurcation curves of the (v, n) subsystem in the $(h, g_{\text{CAN}_{\text{Tot}}})$ parameter plane, as illustrated in Figure 3.5D. The red (resp. blue) curve in this panel is the curve of HC (resp. lower fold (LF)) bifurcations, which terminates (resp. initiates) each burst, as noted previously. Since the increase of $g_{\text{CAN}_{\text{Tot}}}$ moves the bifurcation diagram in the direction of decreasing h , both the LF and HC curves are negatively sloped in $(h, g_{\text{CAN}_{\text{Tot}}})$ -space. Within the same projection, the trajectory evolves rightward from the yellow star until it reaches the LF curve (see Figure 3.5D), where it turns around and heads leftward while the full trajectory starts oscillating, as in the active phase of Figure 3.5C. These oscillations terminate when the trajectory reaches the HC bifurcation curve, which completes the first small burst. Similarly, a sequence of subsequent small bursts occurs, with the local maximum of h progressively decreasing due to the

left drift of LF as $g_{\text{CAN}_{\text{Tot}}}$ increases on the superslow timescale. The fact that the trajectory in $(h, g_{\text{CAN}_{\text{Tot}}})$ -space reaches the LF and HC curves six times before $g_{\text{CAN}_{\text{Tot}}}$ jumps up corresponds to the existence of the six small bursts (see Figure 3.5A). In fact, since the l -nullcline lies close to the left knee of the c -nullcline, as discussed in the Remark of Appendix Section 6.2, the jump up is gradual; a seventh small burst actually occurs during the initial part of the jump up (just after the yellow circle in Figure 3.5A) and is followed by the start of an eighth small burst. In the singular limit, however, this additional bursting will be lost and all small bursts will occur within phase ①.

As the trajectory passes the yellow circle and moves into phase ②, $f_2 = 0$ no longer applies, and the flow switches from superslow to slow. More precisely, the $g_{\text{CAN}_{\text{Tot}}}$ coordinate starts to jump up on the slow timescale, while h remains on the superslow timescale. During this jump up in phase ② (from circle to square), the LF and HC curves will meet at some point, coalescing to form a SNIC bifurcation curve; since the oscillation frequency goes to 0 as a SNIC is approached, as with the HC, we color the SNIC curve red in Figure 3.5D. As c jumps up and pulls the trajectory farther away from the SNIC curve, there is a burst of higher frequency spiking. This spiking results because h , which is evolving superslowly, remains almost constant during phase ②, relative to the decrease of the h -coordinate of the SNIC bifurcation due to the slow jump up of c , and hence the trajectory is now oscillating somewhere relatively far from the SNIC curve (see the yellow square in Figure 3.5D); in this system, the farther the trajectory is from the SNIC, the higher its spiking frequency. We thus obtain spiking with high frequency at the start of phase ③ (yellow square), after which the frequency gradually decreases as the trajectory moves closer to SNIC on the superslow timescale.

Besides the change in frequency, the amplitude of the v spikes increases progressively during phase ③. This feature results from the structure of the somatic system bifurcation diagram: periodic orbit amplitudes start small at the AH bifurcation (large h) and keep increasing as h gets closer to the SNIC bifurcation (Figure 3.5B). The bifurcation diagram moves to the leftmost position as c reaches its maximum value (blue curve in Figure 3.5B), at which h is around 0.4 (yellow square in Figure 3.5D). Hence, at the start of phase ③, the trajectory is oscillating in the middle of the periodic orbit branch, somewhere far from the SNIC bifurcation, resulting in spiking with low amplitude. As c decreases on the superslow timescale during phase ③, it shifts the corresponding bifurcation diagram to the right. Meanwhile, the trajectory moves in the direction of decreasing h

(Figure 3.5D). As a result, the periodic orbits that shape the v spikes are progressively closer to the SNIC bifurcation, and hence these spikes feature increasing amplitude as phase ③ progresses.

As phase ④ begins, c no longer tracks l on the superslow timescale and instead evolves on the slow timescale, just as during phase ②. Hence, the slow jump down in c will bring the trajectory far below the HC/SNIC curve, so the trajectory enters the silent phase and the long burst terminates. As the solution finally returns to our starting point (star in Figure 3.5A and D), one cycle of the MB solution is completed.

Besides describing the dynamic mechanisms underlying MB solutions, our goal is to determine what mix of timescales is involved in the MB pattern. In the following, we separate the MB solution into three phases, denoted by the quiescence (Q) phase, the square-wave bursting (SW) phase, and the long bursting (LB) phase, respectively. Below are the three conditions drawn from the above analysis that together support the MB solution:

- (C1): It is necessary that the somatic subsystem acts as a square-wave burster for c values arising during the SW phase, so that there exist small burst solutions before c jumps up to its active phase. In other words, there must be a gap in h between the LF and HC curves in the $(h, g_{\text{CAN}_{\text{Tot}}})$ parameter plane for c small (Figure 3.5D).
- (C2): The trajectory needs to cross the gap between the LF and HC curves multiple times, with each crossing taking long enough to allow for a square-wave burst, so that there are multiple small bursts before the long burst; the timescales of h , v , and c should be related during the SW phase in a way that makes outcome possible.
- (C3): The transition to the long burst occurs due to the jump up of c to the active phase, which requires the timescale for c to become faster than h and l after the SW phase.

We use these three conditions to find the right combination of timescales that are generally needed to obtain an MB solution.

3.1.3 Finding the combination of timescales that supports MB solutions in the constant- τ model (3.5)

3.1.3.1 (C1) \Rightarrow Analysis of timescales of v and n (C1) requires that the (v, n, h) subsystem acts as a square-wave burster for c small, which is determined by the bifurcation diagram of the

(v, n) subsystem with h treated as a bifurcation parameter. Note that the AH value and the position of the periodic orbit (P) branch of the bifurcation diagram for (v, n) depend on R_v and R_n , which determine the timescales of v and n . Thus, we investigate what mix of timescales for these two variables is needed.

Recall that R_v and R_n can be varied by changing the two parameters C_m and τ_n , respectively. In the following, we fix $C_m = 21$ and vary τ_n to study how it will affect the bifurcation diagram and under what condition the somatic subsystem can generate a square-wave bursting solution. Representative results are shown in Figure 3.6A, where the bifurcation diagram of the (v, n) subsystem with respect to h for $c = 0.0171$ is computed. While the curve of equilibria of the (v, n) subsystem, S (black), and the h -nullcline (cyan) are both independent of τ_n , the periodic orbit branch, P, is sensitive to changes of τ_n . Specifically, an increase of τ_n moves the family of periodic orbits to the right in (h, v) -space (Figure 3.6A).

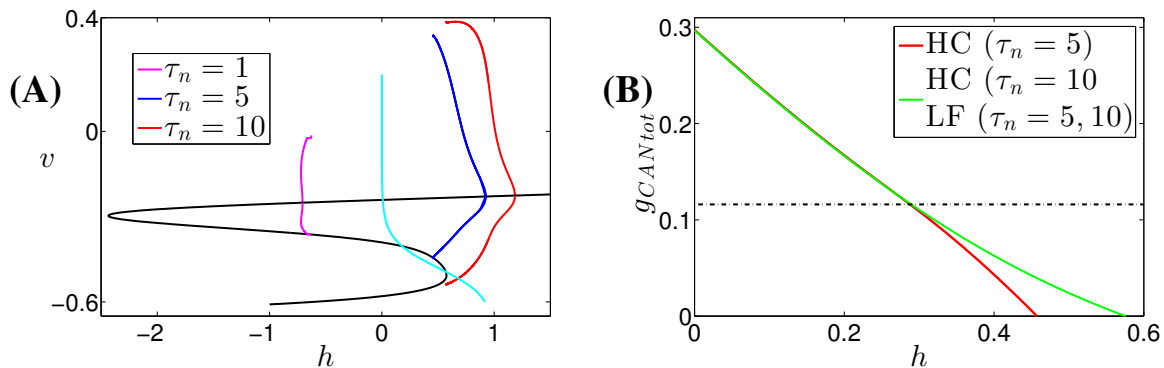


Figure 3.6: Bifurcation diagrams for the somatic subsystem for various τ_n values. (A): Bifurcation diagrams for the somatic subsystem with h as a parameter and c fixed at 0.0171. From the magenta curve to the blue to the red, τ_n varies from 1 to 5 to 10. As τ_n increases, AH and P move to the upper right, while the h -nullcline (cyan) and S (black) remain unchanged. (B): Two curves of HC bifurcations (red, $\tau_n = 5$; green, $\tau_n = 10$) and two curves of LF bifurcations for $\tau_n = 5$ and 10, both overlapping with the green curve, in $(h, g_{CAN_{Tot}})$ parameter space. The horizontal line represents $g_{CAN_{Tot}} = 0.116$, where the green and red curves meet.

For $\tau_n = 1$, as h is decreased, there is a family of small amplitude unstable periodic orbits created in a HC bifurcation involving the middle branch of equilibria S, which terminates when

it coalesces in a SNPO bifurcation with a second family of stable periodic solutions born in a supercritical AH bifurcation on the upper branch of equilibria, as illustrated by the magenta curve in Figure 3.6A. In this case, the MB solution does not exist. In fact, under such a choice, the constant- τ model yields a solution lacking v spiking. For c at its minimum, the h -nullcline and the equilibria branch S intersect at one stable fixed point on the upper branch of S and two unstable fixed points on the middle branch (see Figure 3.6A). Notice that the increase of c , which moves S (black) and P (magenta) to the left, will not change the stability of the equilibrium point on the upper branch of S. Hence, for the full range of c values, there is a stable equilibrium of (v, n, h) , and the trajectory will eventually be attracted by this family of stable equilibria, yielding the plateau of v .

For $\tau_n = 5$ (resp. $\tau_n = 10$) and $c = 0.0171$, the periodic orbit branch is given by the blue (resp. red) curve in Figure 3.6A. In both cases, unlike when $\tau_n = 1$, as h is increased, a stable family of periodic orbits is created in a HC bifurcation involving the middle branch of S and is destroyed in a supercritical AH bifurcation along the upper branch. Although these two stable periodic orbit branches appear to be quite similar, there is a crucial difference between them. For $\tau_n = 10$, there is a SNIC bifurcation as the HC bifurcation meets with the LF bifurcation for c at its minimal value and this bifurcation persists for all c values within a complete relaxation oscillation cycle (see Figure 3.6B). Thus there is only a tonic spiking solution, which violates (C1). For $\tau_n = 5$, there is a gap in h between the LF and HC curves for $c = 0.0171$ (Figure 3.6A), persisting up to roughly $c = 0.14$ (Figure 3.6B), which will result in a square-wave bursting solution as required. Therefore, $\tau_n = 5$ together with $C_m = 21$ is a parameter set that satisfies (C1).

In summary, among all three cases that we have discussed above, only $\tau_n = 5$ ($R_n = 5$) can support the MB solution. Recall that we have chosen the timescale of voltage to be $R_v \sim O(1)$. To determine whether v and n truly can be coordinated as evolving on disparate timescales, a natural question to ask is: can we make the timescales of v and n more separated without losing the MB solution? To figure this out, we now fix $\tau_n = 5$ and allow both C_m and h to vary to find the somatic (v, n) subsystem bifurcation curves in the (C_m, h) parameter plane, as illustrated in Figure 3.7. The LF and HC curves are shown in blue and red, respectively, and the green curve denotes the AH bifurcation on the upper branch of S.

For C_m sufficient large (e.g., 200), as h is increased, there is a branch of unstable small ampli-

tude periodic orbits created in a subcritical AH bifurcation of the upper branch of S and destroyed in a HC bifurcation involving the middle branch of S. As C_m decreases and reaches the intersection point between the AH and HC curves, the criticality of the AH bifurcation changes from subcritical to supercritical and as a result, the bifurcation diagram looks qualitatively the same as the one denoted by the magenta curve in Figure 3.6A. In both cases, there is a stable equilibrium of (v, n, h) at an h value between the AH curve and the LF curve, and hence v asymptotes to a constant depolarized plateau, as for $\tau_n = 1$. As C_m decreases further, the equilibrium point is overtaken by the AH curve and becomes unstable, and (v, n, h) may engage in oscillatory, bursting-like behavior involving a plateau at the start of each active phase (until h decreases through the AH bifurcation) or other complicated behavior; we do not explore such complicated dynamics on the relatively small parameter interval where they arise. From there, an additional decrease of C_m will finally result in the intersection of LF and AH, after which LF is between AH and HC. The resulting bifurcation diagram is then qualitatively as shown in the blue curve in Figure 3.6A and so it can support MB solutions, without any plateau phase or other complications; for clarity, we use this transition to approximate the onset of the MB regime. As we keep decreasing C_m , the curves of HC and LF will meet at $C_m = 12.87$ and become a SNIC. As a result, the bifurcation diagram is qualitatively as shown in Figure 3.6A by the red curve and hence v engages in tonic spiking for C_m below this value, corresponding to the end of the MB regime.

We use the two vertical dashed magenta lines in Figure 3.7A to demarkate $C_m = 12.87$ and $C_m = 35.62$, at which the SNIC bifurcation appears and at which the LF and AH bifurcation curves intersect, respectively. These two lines divide (C_m, h) -space into three regions, which we can call regions 1, 2, and 3 from left to right. Our analysis has shown that v engages in tonic spiking for parameter values chosen in region 1 and v asymptotes to a steady state in at least most of region 3. MB solutions arise for parameters selected in region 2, which is bounded by the two magenta curves, i.e., $12.87 \leq C_m \leq 35.62$ with τ_n fixed at 5. In terms of the timescales, (C1) requires the timescale of v to satisfy $0.4596 \leq R_v \leq 1.2721$ with the timescale of n given by $R_n = 5$. Similarly, there is a range of τ_n values for which the bifurcation curves align properly for fixed C_m (Figure 3.7B). In other words, a certain difference in rate constants for v and n is required, but the extent of the timescale separation is bounded, and thus v, n should indeed be considered as evolving on the same timescale, albeit at different rates.

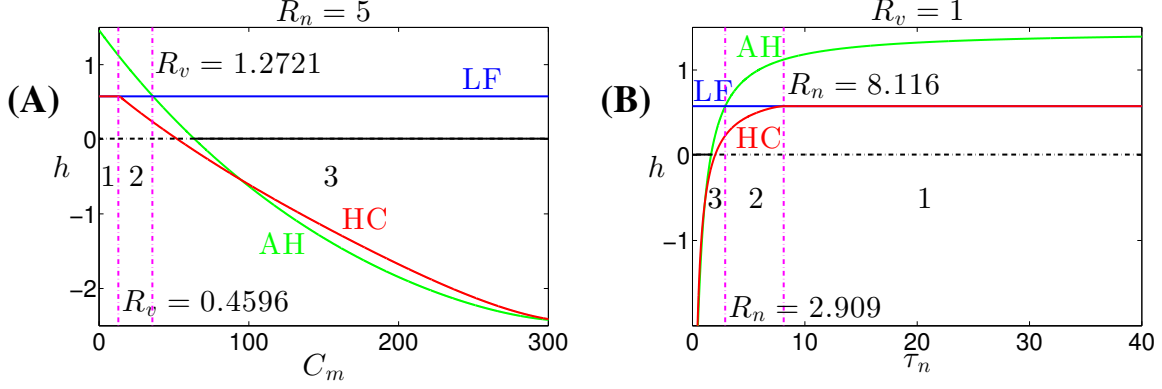


Figure 3.7: Bifurcation curves for the (v, n) subsystem of (3.5) for $c = 0$. The curves of AH bifurcations, LF bifurcations and HC bifurcations are given by the green, blue and red curves, respectively. Solid (resp., dashed) black curves indicate stable (resp., unstable) equilibria of the somatic subsystem. (C1) requires that for fixed C_m , the curves progress from red to blue to green as h increases. (A): (C_m, h) parameter space with $\tau_n = 5$. The two magenta vertical lines represent $C_m = 12.87$ and $C_m = 35.62$, at which the LF and HC bifurcation curves intersect and the LF and AH bifurcation curves intersect, respectively. (B): (τ_n, h) parameter space with $C_m = 21$. The two magenta vertical lines represent $\tau_n = 2.909$ and $\tau_n = 8.116$, with similar interpretations as in (A).

3.1.3.2 (C2) and (C3) \Rightarrow Analysis of timescales of h , v_2 and w Using (C2) and (C3), we can obtain the relation among timescales for the other three variables, h , c and l , required to yield an MB solution. Imposing (C3), we require that the (c, l) system acts as a relaxation oscillator and so the timescale of c is determined by that of l during its silent phase. In other words, we have $R_c \approx R_l$ during phase ① and phase ③. Moreover, the fact that almost all small bursts happen during phase ① suggests that the SW phase lies in phase ①. As a result, for (C2), we compare R_h with R_l , rather than R_c , during phase ①.

Based on (C1), (C3), and (3.6), we set the timescales to be $(R_v, R_n) \sim (1, 5)$ and $(R_c, R_l) \sim (10, 1000)$, respectively. Next we consider (C2). By fixing $R_l = 1000$ and varying τ_h , which controls R_h , we study the influence of the relation between R_h and R_l on the dynamics of (3.5). From numerical simulations over a range of τ_h values, we find that (3.5) can generate MB solutions

when $\tau_h = 1000$, but this pattern is lost when $\tau_h = 90$ (Figure 3.8A) or $\tau_h = 10000$ (Figure 3.8B). These numerical results suggest that h and l may need to evolve at comparable rates in order for the constant- τ model to generate MB solutions.

The top row in Figure 3.8 shows the time series for v , while the bottom row shows the two-parameter bifurcation diagrams in $(h, g_{\text{CAN}_{\text{Tot}}})$ -space together with the projection of the solution shown in the top row. The left panel of Figure 3.8 shows the case when $R_h = 90 < R_l = 1000$ during phase ①. Since c is slaved to l in this phase, h is evolving faster than c and thus the trajectory crosses the curves of LF and HC bifurcations within only one spike. This process will continue until c jumps up to its maximum value (yellow square), after which a burst of higher frequency spiking begins via the mechanism discussed in Section 3.1.2 and terminates when c falls down during phase ④. Therefore, the spiking persists throughout the c oscillation, failing to yield an MB solution. In the other case, when h evolves on a timescale of $O(10000)$, h is slower than l and c , and (3.5) generates a bursting solution as shown in Figure 3.8B. This solution arises because the drift of the trajectory in the direction of decreasing h after passing the curve of LF bifurcations is too slow for the solution to reach the curve of HC bifurcations (see Figure 3.8D). As a result, spiking continues throughout the silent and active phases of the (c, l) oscillation, corresponding to a single burst active phase, until the slow jump down of c during phase ④ brings the flow below the HC curve, terminating the burst of v spiking. On the other hand, if we fix $R_h = 1000$ and slow down l (e.g., $R_l = 10000$), the MB solution persists, with more small bursts produced within each MB cycle because phase ①, during which small bursts occur, is prolonged. Therefore, we conclude that for mixed bursting, the timescales should satisfy the following refined and extended version of condition (C2):

(C2)': The trajectory needs to cross the gap between the LF and HC curves multiple times, with each crossing taking long enough to allow for a square-wave burst, so that there are multiple small bursts before the long burst; for this to happen, h should be slow enough relative to v and n , and c should evolve at least as slowly as h during the SW phase.

For the above analysis to apply, we require that c evolves faster than h and l , but we have not yet specified how fast. The discussion up to this point shows that if (C3) holds and we speed up c , then we do not affect (C1), (C2)', or (C3). In fact, as long as the relaxation character of the (c, l)

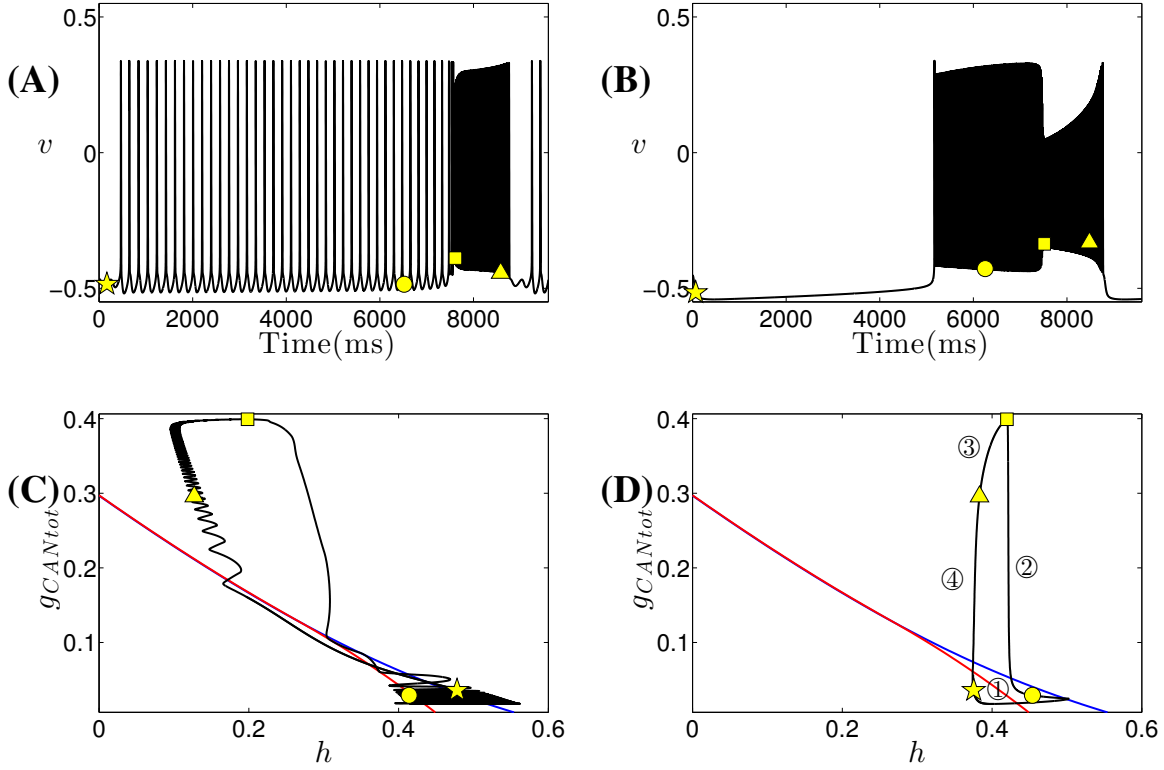


Figure 3.8: Time series for attracting solutions of the constant- τ model and associated bifurcation diagrams when $R_v = 1$, $R_n = 5$, $R_c = 10$, and $R_l = 1000$. In (A) and (C), $R_h = 90$, (B) and (D): $R_h = 10000$. Top row shows temporal evolution of v (black); bottom row shows the curves of HC bifurcations (red), LF bifurcations (blue) and the trajectory (black), projected into $(h, g_{CAN_{Tot}})$ parameter space. The yellow symbols indicate transition points between different phases for the dendritic subsystem, as shown in Figure 3.3. Circled numbers in (D), which represent the four phases of the (c, l) oscillation as in Figure 3.3, are omitted in (C).

oscillations is maintained, the timescale of c , which determines how fast the jump up of c happens and hence determines how fast the transition from the small burst to the long burst occurs, will not affect the MB pattern qualitatively. This claim is supported by the simulation result that if we make $R_c \sim O(1) = R_v$ so that c evolves on the same timescale as v , the MB pattern still occurs.

We summarize the choices about the timescales that support MB dynamics in Table 3.2, from

which we observe that there are three different orders of magnitude present. If MBs are truly a three timescale form of dynamics, then we should be able to separate these three classes as much as we like while still maintaining the MB solution. However, this is not the case. In fact, the MB solution breaks down as we make (v, c) and n more separated. Hence, in a timescale decomposition, the timescales should be considered as segregating into two classes. This grouping is supported by the fact that as we exaggerate the separation between these two classes, the MB solution still exists. Therefore, we conclude that the MB solution of the constant- τ model (3.5) is not specifically a three timescale phenomenon.

Table 3.2: Timescales for the constant- τ model (3.5)

Fast			Slow	
R_v	R_n	R_c	R_h	R_l
(0.4596, 1.2721)	5	(0.4596, 5)	1000	≥ 1000

3.1.4 Dynamics of the mixed bursting model (3.1)

In this subsection, we will first use the approach that was applied in Section 3.1.2 to explain the mechanisms underlying MB solutions of (3.1) with parameters given by Table 3.1. After that, we will analyze what mix of timescales can support MB solutions and how timescales should be grouped to apply geometric singular perturbation theory. Finally, recalling that MB solutions generated by the system (3.1) for its original parameter values are very sensitive to changes in parameters, we will investigate how the timescales of the mixed bursting model can be tuned to make the MB solutions more robust, reflecting the fact that they are observed experimentally [14].

Based on the timescales that we have found in Section 3.1.3, we can now modify the original mixed bursting model (3.1), the dimensionless version of which is given by (3.4), to obtain MB solutions. Notice that the only difference between the mixed bursting model and the constant- τ model is whether the timescales of n and h are the v -dependent functions $\tau_n(v)$ and $\tau_h(v)$ or the constants τ_n and τ_h . We set $R_c = O(1)$ by increasing K_{Ca} from $2.5e - 5$ to $1.25e - 4$ and keep timescales for v and l unchanged so that we have $(R_v, R_c, R_l) = (O(1), O(1), O(1000))$. According

to Table 3.2, we will need to modify $\tau_n(v)$ and $\tau_h(v)$ in order to obtain $R_n \approx 5$ and $R_h \approx 1000$ for MB solutions. Specifically, we require these two functions to be less dependent on v and so as close as possible to the size 5 or 1000. To this end, we introduce a new parameter a_x with default value 0 and abuse notation to redefine $1/\tau_x(V) = \bar{\tau}_x/\cosh((V - \theta_x)/2\sigma_x) + a_x$, where $x \in \{n, h\}$. We constrain the timescales for n and h by varying the parameters (σ_n, a_n) and (σ_h, a_h) , respectively.

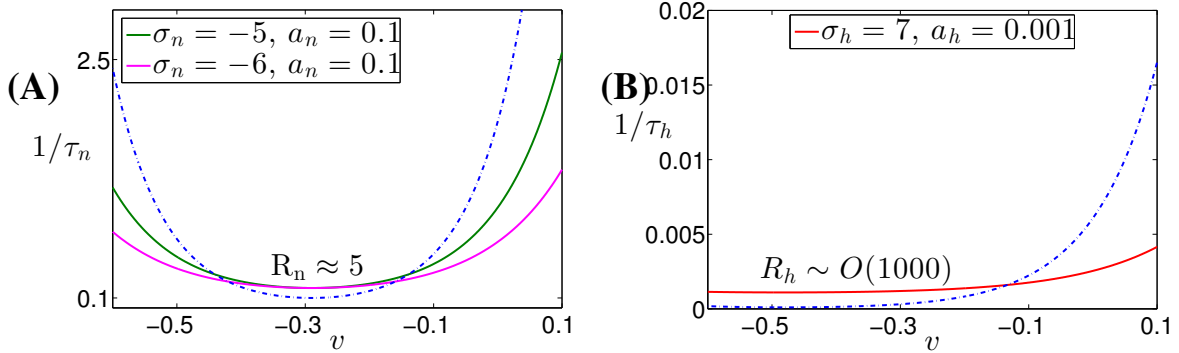


Figure 3.9: The graphs of the functions $1/\tau_n(v)$ and $1/\tau_h(v)$, with both default and new choices of σ_n , a_n , σ_h and a_h . (A): The graph of $1/\tau_n(v)$ for the default parameter values $(\sigma_n, a_n) = (-4, 0)$ (dashed blue), or for the modified parameter values $(\sigma_n, a_n) = (-5, 0.1)$ (green) or $(\sigma_n, a_n) = (-6, 0.1)$ (magenta). (B): The graph of $1/\tau_h(v)$ for the default parameter value $(\sigma_h, a_h) = (5, 0)$ (dashed blue), or for the modified parameter value $(\sigma_h, a_h) = (7, 0.001)$ (red).

In Figure 3.9, we plot both the original τ_x functions and their modified versions with the new parameters we have chosen. The reciprocals of the original τ_n and τ_h functions are given by the dashed blue curves, while the reciprocals of the modified functions that are now less dependent on voltage are denoted by the solid curves. To understand the effects of modifying τ_n on the robustness of MB solutions, we consider two examples of $\tau_n(v)$, the reciprocals of which are shown in Figure 3.9A. In the case when $\sigma_n = -6$, the upper branch of somatic subsystem equilibria (magenta) intersects the h -nullcline (cyan) at a stable fixed point (Figure 3.10), leading to a bistability of silence and bursting and hence compromising the robustness of the bursting solution. There is no such issue in the other case, when $\sigma_n = -5$. In fact, the resulting bifurcation diagram (Figure 3.10, green) is qualitatively the same as the one denoted by the blue curve in Figure 3.6A except that the AH bifurcation on the upper branch of S is now subcritical, and so we choose to modify $\tau_n(v)$ with

$$\sigma_n = -0.5, a_n = 0.1.$$

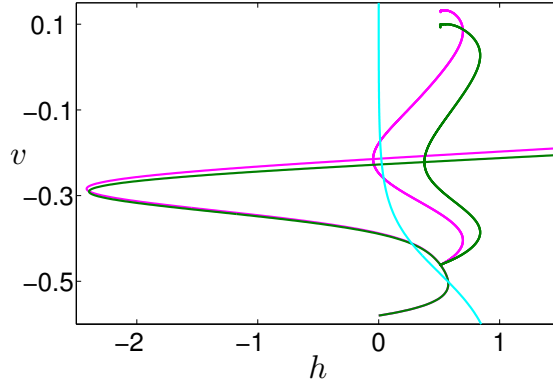


Figure 3.10: The bifurcation diagrams of the somatic subsystem corresponding to the modified forms of $\tau_n(v)$ as shown in Figure 3.9A, along with the h -nullcline (cyan). The other color codings are the same as in Figure 3.9A.

Recall that it is not accurate to simply nondimensionalize $1/\tau_x(V)$ by dividing it by its maximum, $T_x = \max(1/\tau_x(V))$, due to its dependence on voltage. Taking into consideration the full range of $1/\tau_x(V)$ rather than just the maximum, we summarize the timescales of n and h in Table 3.3.

Table 3.3: Time Scales of n and h

Case	σ_n	a_n	R_n	σ_h	a_h	R_h
Default	-4	0	$O(10) \sim O(0.1)$	5	0	$O(10000) \sim O(100)$
Modified	-5	0.1	≈ 5	7	0.001	$\sim O(1000)$

With (R_v, R_c, R_l) fixed at $(O(1), O(1), O(1000))$, the version of system (3.4) derived with the modified τ_n and τ_h given in Table 3.3 is able to generate an MB solution (Figure 3.11A). The HC and LF bifurcation curves in $(h, g_{\text{CAN}_{\text{Tot}}})$ parameter space as shown in Figure 3.11B are qualitatively the same as those denoted by the red and blue curves in Figure 3.5D in Section 3.1.2. Hence the mechanisms underlying the MB solution from (3.4), the dimensionless version of the

mixed bursting model, are qualitatively the same as those underlying the MB solution from the constant- τ model as discussed in Section 3.1.2, and the details of these mechanisms are omitted here.

Further speeding up of h (e.g., dividing τ_h by 10) will eliminate MB solutions (Figure 3.11C), as will the slowing down of h (e.g., multiplying τ_h by 10, see Figure 3.11E). The bifurcation mechanisms involved are again similar to what happens to the constant- τ model, as seen by comparing Figure 3.11D with Figure 3.8C and Figure 3.11F with Figure 3.8D. Hence, the results from the constant- τ model give crucial insights into how to adjust and group timescales for the original mixed bursting model to support MB solutions.

3.2 ROBUSTNESS OF THE MIXED BURSTING MODEL

Recall that for the original parameter values as given in Table 3.1, MB solutions of the mixed bursting model have sensitive dependence to $[\text{IP}_3]$ and g_{NaP} , two critical parameters that help control the relative contributions of I_{CAN} and I_{NaP} and are used in previous studies to switch between different forms of bursting dynamics [73, 47]. With the new mix of timescales chosen in Section 3.1.4, simulation results show that the mixed bursting model can generate MB solutions that are significantly more robust to variations in both $[\text{IP}_3]$ and g_{NaP} (Figure 3.12). In the following, we will examine what happens to the system dynamics under variations of timescales to yield this great enhancement of robustness of MB solutions to $[\text{IP}_3]$ and g_{NaP} .

3.2.1 Robustness to $[\text{IP}_3]$

To investigate the dependence of MB solutions of system (3.4) on $[\text{IP}_3]$, we fix $g_{\text{NaP}} = 2$. Notice that as $[\text{IP}_3]$ increases from 0.95 (Figure 3.13A) to 1.5 (Figure 3.13B), the number of small bursts per MB cycle decreases. If we keep increasing $[\text{IP}_3]$, the small bursts will eventually disappear and the MB solution will be lost. By understanding the effect, we can deduce what adjustments are needed to make MB solutions even more robust to changes in $[\text{IP}_3]$.

From Figure 3.14, we find that an increase of $[\text{IP}_3]$ shifts the c -nullcline downward and there-

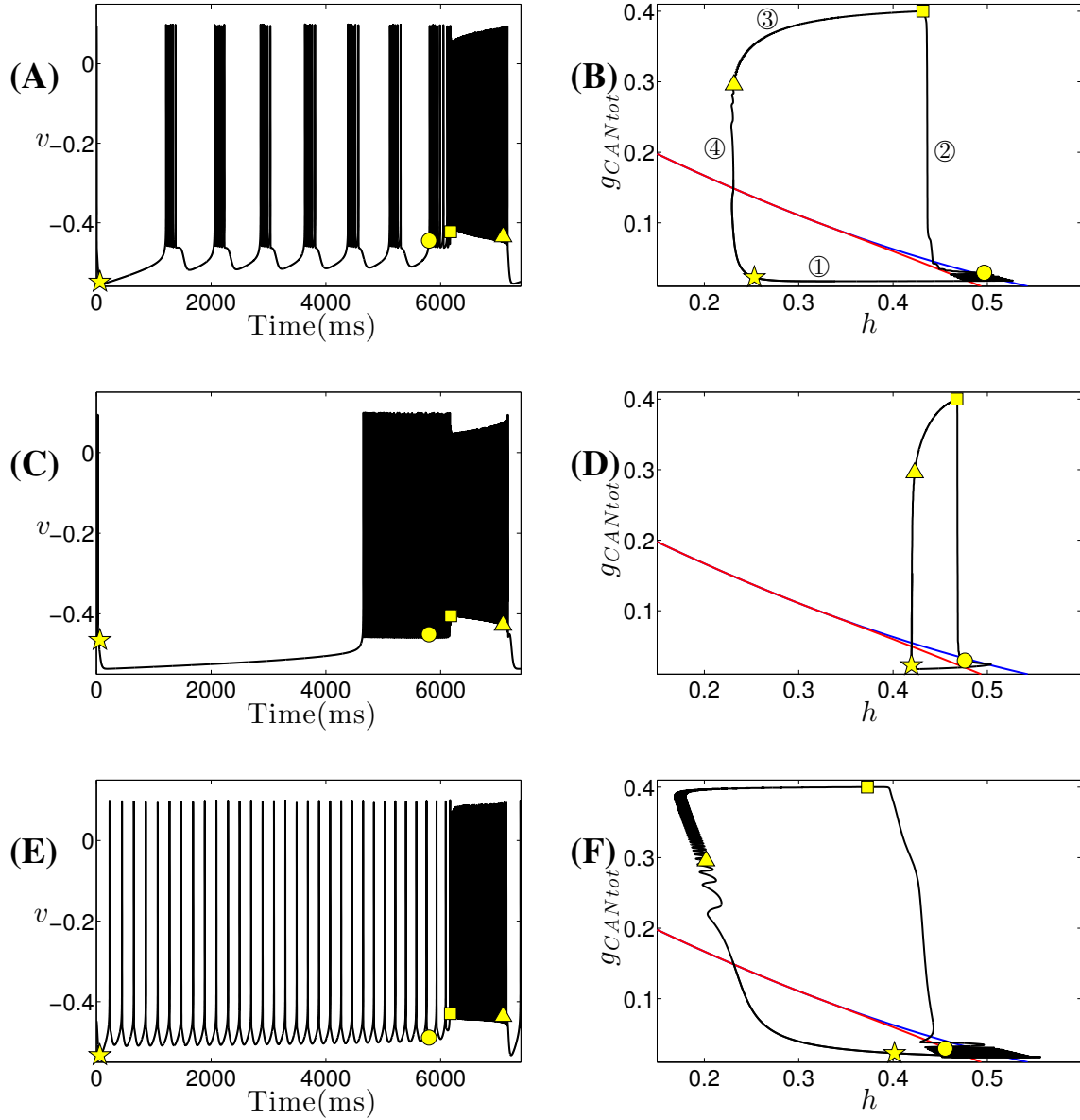


Figure 3.11: Time series for attracting solutions of (3.4) and corresponding bifurcation diagrams, with modified τ_n and τ_h as shown in Figure 3.9 and Table 3.3 and with other timescales given by $(R_v, R_c, R_l) = (O(1), O(1), O(1000))$. Left panels: Temporal evolution of v . Right panels: Two-parameter bifurcation diagrams showing HC (red) and LF (blue) curves, together with the projection of the trajectory (black) from the left panel, in $(h, g_{CAN_{Tot}})$ -space. In the top row, h is evolving on a timescale of $O(1000)$, which is 10 times as slow (resp. fast) as in the middle (resp. lower) row. The yellow symbols have the same meanings as in Figure 3.3. Circled numbers in (B), which represent the four phases of the (c, l) oscillation as in Figure 3.3, are omitted in (D) and (F).

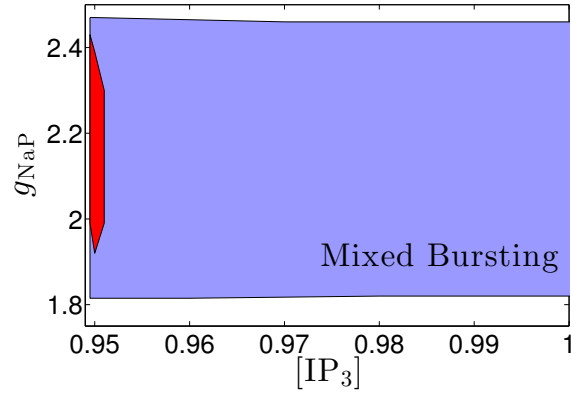


Figure 3.12: Regions of MB solutions in $([IP_3], g_{NaP})$ -space for the mixed bursting model. The region for MB solutions of the mixed bursting model for its original parameter values as given in Table 3.1 is shown in red; the MB region for the new mix of timescales $(R_v, R_c, R_l) = (O(1), O(1), O(1000))$, with R_n and R_h given in Table 3.3, obtained by making $C_m = 21$, $K_{Ca} = 1.25 \times 10^{-4}$, $A = 0.001$, $\sigma_n = -5$, $a_n = 0.1$, $\sigma_h = 7$ and $a_h = 0.001$, is shown in blue. While the right boundary of the blue region ends at $[IP_3] \approx 1.58$ for $g_{NaP} \in [1.78, 2.43]$, we only plot the part with $[IP_3] \leq 1$ to allow better visibility of the red region.

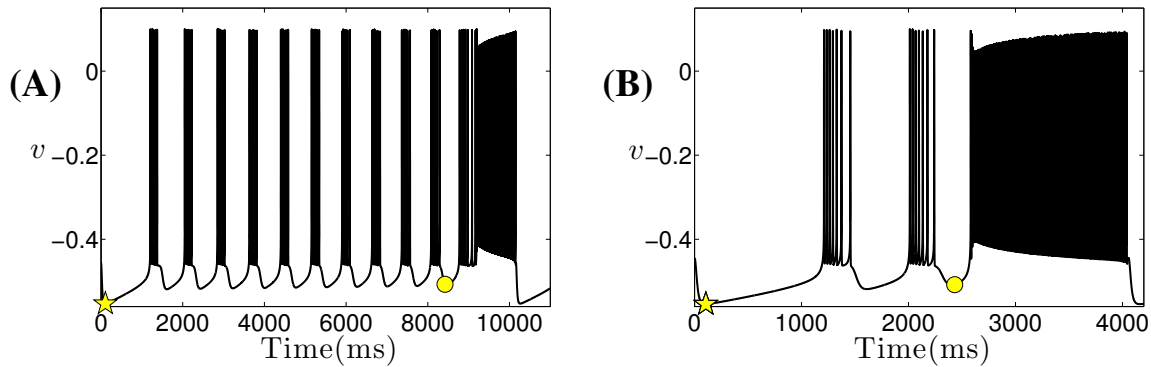


Figure 3.13: Time series of (3.4) with $C_m = 21$, $K_{Ca} = 1.25 \times 10^{-4}$, $A = 0.001$, $\sigma_n = -5$, $a_n = 0.1$, $\sigma_h = 7$ and $a_h = 0.001$. Other parameters are as in Table 3.1 except (A): $[IP_3] = 0.95$, (B): $[IP_3] = 1.5$. In both plots, the yellow symbols have the same meanings as in Figure 3.3.

fore influences the dynamics of the (c, l) subsystem. A summary of the effect of $[IP_3]$ variations on the intracellular calcium dynamics is provided in Figure 3.15. There is one stable fixed point on the left branch of the c -nullcline for $[IP_3]$ small. As $[IP_3]$ increases, the stability changes at an AH bifurcation, which initiates the periodic oscillations of (c, l) . For $[IP_3]$ close to this AH bifurcation, the left knee of the c -nullcline stays near the fixed point of the dendritic subsystem and hence close to the l -nullcline. This proximity is also evident in Figure 3.14, where for $[IP_3] = 0.95$ closer to the AH bifurcation (Figure 3.14A), the l -nullcline lies closer to the left knee of the c -nullcline compared with that when $[IP_3] = 1.5$ (Figure 3.14B). As a result, even though c evolves on the same timescale, determined by its slaving to l , during phase ① (Figure 3.14: from the yellow star, $c \approx 0.0175$, to the yellow circle, $c \approx 0.0293$), for both $[IP_3]$ values in Figure 3.14, this phase duration is much longer for $[IP_3] = 0.95$, where the trajectory spends on long time near the fold (yellow circle), than for $[IP_3] = 1.5$, as observed in Figure 3.13. Recall that all small bursts occur during the silent phase before c gets large, as shown in Figure 3.13 and 3.16; as a result, there are fewer small bursts for $[IP_3] = 1.5$. Specifically, in Figure 3.16A when $[IP_3] = 0.95$, the silent phase time is long enough for the trajectory to pass between the LF and HC curves multiple times and hence v exhibits multiple small bursts. However, for the other case shown in Figure 3.16B, the time available for generating small bursts is so short that only two small bursts occur before the yellow circle.

Therefore, one way to make the MB solution more robust is by prolonging the silent phase of the dendritic subsystem oscillation. To this end, we can make l slower so that it is more separated from c and h . In that way, the orbits adhere closer to the c -nullcline during the silent phase and are slaved to l on a slower timescale, resulting in a longer silent phase for each fixed $[IP_3]$.

On the other hand, according to (C1), the somatic subsystem must yield bursting for the full system to generate MB solutions, i.e., there must be a gap in h between the LF and HC curves in $(h, g_{CAN_{Tot}})$ parameter space (Figure 3.16). The presence of this gap is determined by the effect of $g_{CAN_{tot}}$ on the dynamics of the somatic subsystem: as $g_{CAN_{tot}}$ increases from the yellow star in Figure 3.16, the dynamics changes from square-wave bursting to tonic spiking. As τ_n is modified according to Table 3.3, LF remains unchanged, while the HC curve moves further away from the LF curve (Figure 3.17). Correspondingly, the range of $g_{CAN_{tot}}$ values for which there exists a gap becomes wider and the gap also expands relative to the default case. Therefore, the $g_{CAN_{tot}}$ interval

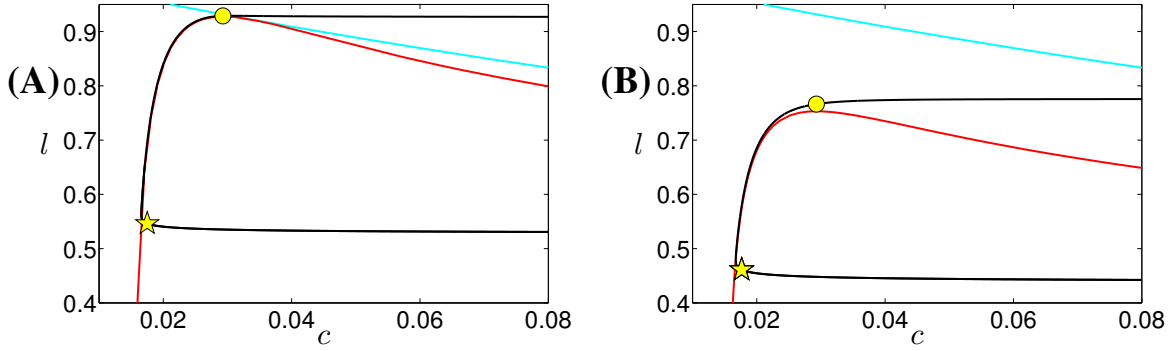


Figure 3.14: Projection of the two MB solutions (black) from Figure 3.13 to (c, l) -space. The red curve is part of the c -nullcline and the cyan curve is part of the l -nullcline. The yellow symbols have the same meanings as in Figure 3.13. (A): $[IP_3] = 0.95$. (B): $[IP_3] = 1.5$. Other parameters as in Figure 3.13.

over which bursting occurs in the somatic subsystem is broadened with the modified timescale for n .

As a result, it is natural to expect that within the same amount of silent phase time of the dendritic subsystem oscillation, the mixed bursting model with the modified τ_n will be able to generate more small bursts. This is not the case, however. In fact, for $[IP_3] = 1.5$, the mixed bursting model with the default τ_n yields an MB solution consisting of the same number of small bursts (Figure 3.17) as with the modified τ_n (Figure 3.16B). The effect of the adjustment of the timescale for n is to increase the duration and the number of spikes within each small burst, corresponding to the larger gap between the LF and HC curves, resulting in more biologically relevant small burst events.

3.2.2 Robustness to g_{NaP}

To study the robustness of MB solutions to g_{NaP} , we fix $[IP_3]$ at 0.95. A systematic way to investigate the dependence of MB solutions on g_{NaP} is via bifurcation analysis. Numerical simulations show that as g_{NaP} is increased, the behavior of the somatic subsystem switches from plateauing

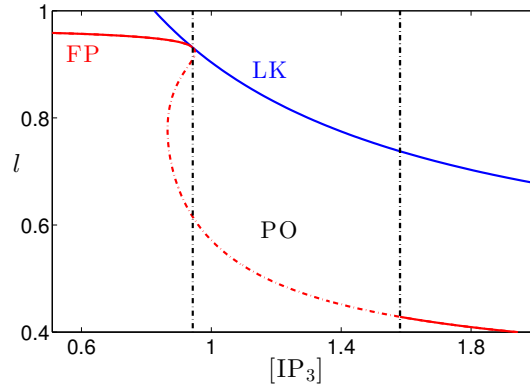


Figure 3.15: Summary of how structures relevant to the activity of the dendritic subsystem depend on the parameter $[IP_3]$, with all other parameters involved in the calcium dynamics as given in Figure 3.13. The red solid (resp., dashed) curve indicates the l -coordinate of the stable (resp., unstable) intersection of the c - and l -nullclines, i.e., fixed points (FP), for the dendritic subsystem, while the blue curve denotes the l -coordinate of the left knee (LK) of the c -nullcline for the dendritic subsystem, both parametrized by $[IP_3]$. The two black vertical lines indicate the $[IP_3]$ values of two AH bifurcations in the dendritic subsystem where the periodic oscillations (PO) of (c, l) begin ($[IP_3] = 0.942602$) and terminate ($[IP_3] = 1.58101$), respectively.

to bursting to spiking, corresponding to the full system transitioning from bursting driven by the dendritic subsystem (dendritic bursting [73, 47]) to mixed bursting to bursting that involves both the somatic and dendritic subsystems but without a mix of burst types (somato-dendritic bursting [73, 47]). A graphical summary of the effect of g_{NaP} variations on the dynamics of the somatic subsystem is provided in Figure 3.18, where the bifurcation structure of the somatic subsystem with respect to g_{NaP} for $g_{CAN_{Tot}} = 0$ is displayed. We plot g_{NaP} against the standard Euclidean norm of the solution. The plateauing branch of the somatic subsystem (red) is stable for the smaller g_{NaP} values. The stability changes at an AH bifurcation and the spiking family (blue) becomes stable at a period doubling (PD) bifurcation. Moreover, the blue curve terminates at a homoclinic bifurcation involving the unstable equilibrium branch (red). Between the spiking and the plateauing is the

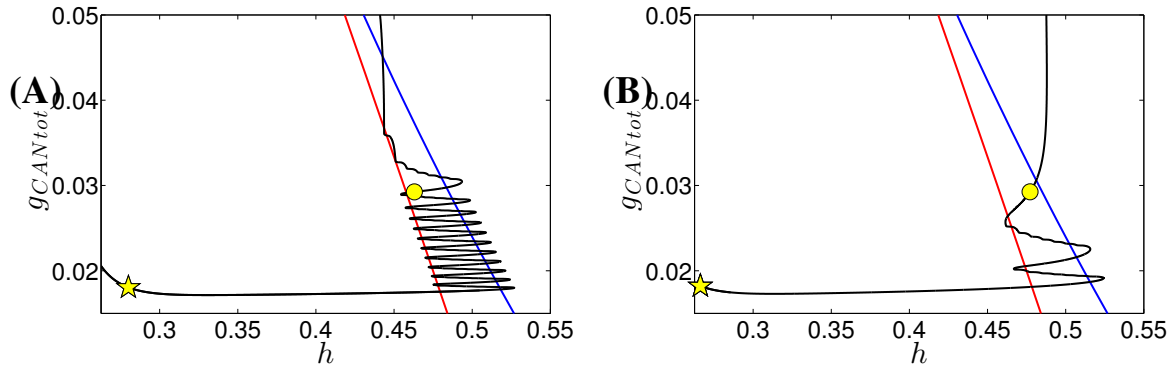


Figure 3.16: The zoomed view of two-parameter bifurcation diagrams of HC (red), LF (blue) and the trajectory (black) from Figure 3.13, projected into $(h, g_{CAN_{tot}})$ -space. The yellow symbols have the same meanings as in Figure 3.13. (A): $[IP_3] = 0.95$, (B): $[IP_3] = 1.5$. Other parameters as in Figure 3.13.

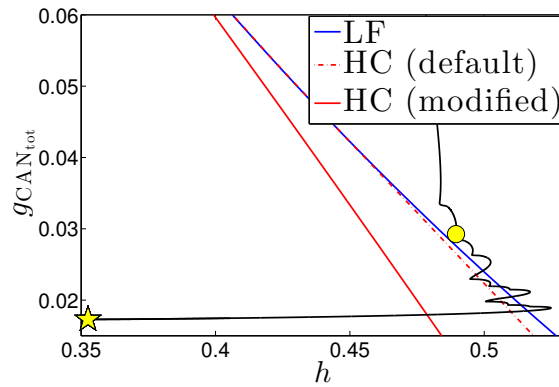


Figure 3.17: Two curves of HC bifurcations (red solid, modified τ_n : $\sigma_n = -5$, $a_n = 0.1$; red dashed, default τ_n : $\sigma_n = -4$, $a_n = 0$) and two overlapping curves of LF bifurcations (blue, default and modified τ_n), in $(h, g_{CAN_{Tot}})$ parameter space. The black curve denotes the trajectory for the default τ_n function, with other parameters the same as in Figure 3.13-3.16B. The yellow symbols have the same meanings as in Figure 3.13.

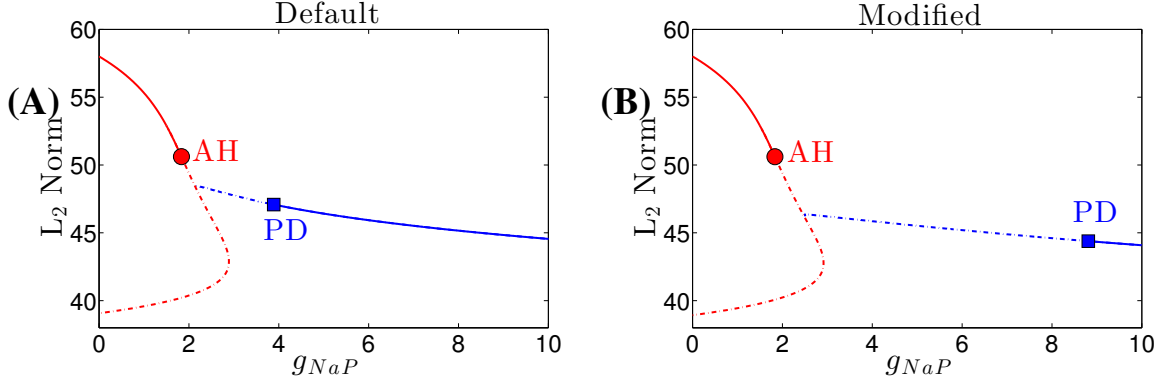


Figure 3.18: Effect of variations in g_{NaP} on the behaviors of the somatic subsystem for (A) default $\tau_n(v)$ and (B) modified $\tau_n(v)$ (denoted by the green curve in Figure 3.9A), respectively, with all other parameters fixed at their standard values.

g_{NaP} interval where the somatic subsystem is available in participating in bursting. According to previous work on the square-wave burster [7], bursting patterns result for most of the g_{NaP} interval between the AH and PD bifurcations. Hence, as g_{NaP} is increased, the transitions mentioned above occur approximately at an AH bifurcation (onset of oscillations) and a PD bifurcation (transition between bursting and spiking) for the somatic subsystem, respectively. Next we extend this bifurcation analysis and examine the dependence of MB solutions on both g_{NaP} and $g_{\text{CAN}_{\text{Tot}}}$. To do this, we compute two-parameter bifurcation diagrams in $(g_{\text{CAN}_{\text{Tot}}}, g_{\text{NaP}})$ -space (Figure 3.19).

In Figure 3.19A, the somatic subsystem's spiking/bursting boundary (blue, PD) was calculated by following the PD point in $(g_{\text{CAN}_{\text{Tot}}}, g_{\text{NaP}})$, while the boundary between bursts and plateau solutions was computed by following the AH point where the fixed points of the somatic subsystem lose stability. In panel (B), we show a similar a two-parameter bifurcation diagram for the modified τ_n function. Comparing these two plots shows that for all $g_{\text{CAN}_{\text{Tot}}}$ values below 0.05, i.e., for all c values within a complete relaxation oscillation cycle, the somatic subsystem after modification can generate bursting solutions for a wider range of g_{NaP} . Recall that in order for the full system to generate MB solutions, (C1) requires the somatic subsystem to engage in bursting for c values arising during the silent phase of calcium. Hence with the new mix of timescales, MB solutions of

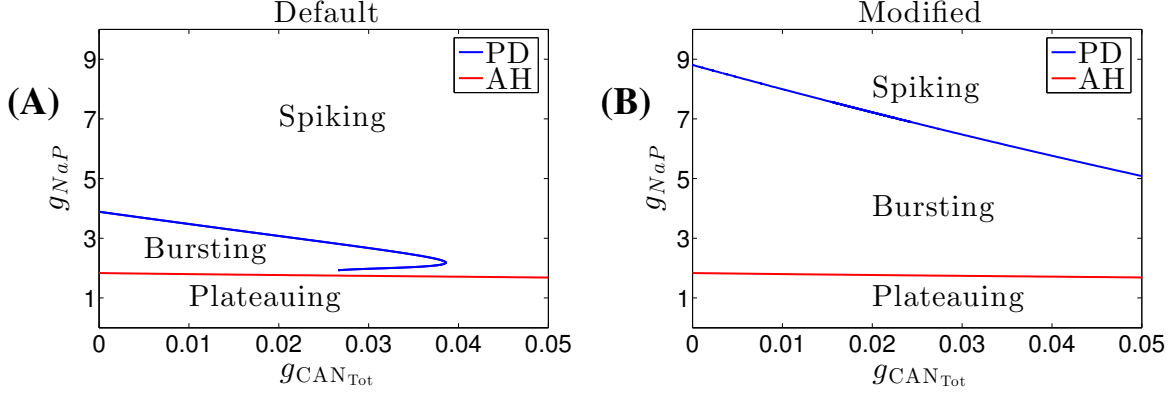


Figure 3.19: Spiking/bursting and bursting/plateauing boundaries of the somatic subsystem for (A) default $\tau_n(v)$ and (B) modified $\tau_n(v)$ as in Figure 3.18.

the mixed bursting model (3.4) become more robust to g_{NaP} .

The bursting region for the somatic subsystem is broadened (Figure 3.19) due to the effect of τ_n on its bifurcation diagram. As discussed in Section 3.2.1, for g_{NaP} fixed, the bursting interval in $g_{CAN_{tot}}$ becomes larger with the new τ_n function, since the range of $g_{CAN_{tot}}$ for which there exists a gap in h between the LF and HC curves in $(h, g_{CAN_{tot}})$ -space is increased. Similarly, for $g_{CAN_{tot}}$ fixed, a gap between the LF and HC curves in (h, g_{NaP}) -space is also required to obtain square-wave bursting. Bifurcation analysis shows that this gap persists for a larger range of g_{NaP} values and therefore the bursting interval in g_{NaP} becomes greater for the modified τ_n . Hence, the new timescale for n helps enlarge the bursting region in $(g_{CAN_{tot}}, g_{NaP})$ -space, which in turn enhances the robustness of MB solutions for the full system with respect to changes in g_{NaP} for each fixed g_{CAN} .

3.3 DISCUSSION

We consider a single compartment reduction [47] of a two-compartment model of a pre-BötC neuron [73], featuring both NaP and CAN currents, as well as intracellular calcium oscillations

that modulate the CAN current. Previous work characterized the regions of $([IP_3], g_{NaP})$ parameter space in which various types of solutions, namely somatic bursting, dendritic bursting, and somato-dendritic bursting, occur in these models [73], [47]. While [47] presented a mathematical analysis explaining relevant bursting mechanisms, based on the NaP current, the CAN current, or both currents working together, less analysis about MB solutions was provided and little consideration was given to identifying how many timescales are truly required to obtain these solutions or to their robustness. In this Chapter, we have explained the mechanisms underlying MB solutions. Our method is based on the ideas of fast-slow decomposition, implemented by considering the interaction of two subsystems (one potentially bursting and the other intrinsically oscillating). This approach is commonly used in the two timescale setting and has also recently been extended to a three timescale system [41], as discussed in Chapter 2.

In the course of our analysis, we derive certain conditions on the timescales that together support MB solutions, based on which we obtain a non-intuitive result that the MB solution is in fact, at its simplest, a two timescale phenomenon rather than requiring three timescales. Our analysis about how to group timescales in this system may provide useful information for future studies of irregular bursting solutions observed in other realistic biological models and in recordings from respiratory CPG neurons as well as subthalamic nucleus (STN) neurons in the basal ganglia (e.g. [3], [30], [14]). Our approach may also prove helpful to modelers making choices about timescale groupings in other physical systems.

While parts of this work investigate rather specific details of the MB solution, we have also followed our analysis with an investigation of how the mixed bursting model can be tuned to obtain more robust MB solutions. In Section 3.2, we have investigated why the new mix of timescales that we have found can support more robust MB solutions and hence have determined how to obtain a larger MB region in $([IP_3], g_{NaP})$ parameter space by changing timescales. Given that MB activity is observed in pre-BötC recordings, we propose that the modified model that we have derived would be a reasonable choice for incorporation in future studies of pre-BötC network dynamics. From an MB state, both increases and decreases of g_{NaP} that are sufficiently large should yield non-mixed bursting. MB dynamics is predicted to be robust to slowing of IP_3 dynamics but not with respect to slowing of Ca^{2+} dynamics. Furthermore, although the contribution of a SNIC bifurcation to MB dynamics is reminiscent of parabolic bursting [53], we nonetheless do not expect pre-BötC

neurons to exhibit behavior with the quantitative properties of parabolic bursting, because the fast jumps in Ca^{2+} , relative to the slower persistent sodium inactivation dynamics, will yield abrupt transitions to rapid spiking and to quiescence (e.g., Figures 3.8A and 3.11E) even if there are two fast subsystem SNIC events per cycle.

4.0 MULTIPLE TIMESCALE SIGH-LIKE BURSTING IN A SELF-COUPLED PRE-BÖTC NEURON

While our methods and analysis developed from Chapter 2 work well in revealing the mechanisms underlying the mixed bursting (MB) solutions discovered in pre-BötC neurons in Chapter 3, we have considered only one-directional coupling, from the dendritic to the somatic subsystem, such that the mixed burst model can be thought of as one oscillator forcing another. Nonetheless, there are many variations on the coupling among timescales that arise in other model systems. As noted in Chapter 1, Jasinski et al. recently presented a more detailed model for neurons in the pre-BötC, where each of membrane potential and cytoplasmic Ca^{2+} concentration can influence the evolution of the other, and showed that a heterogeneous population of these neurons can generate sigh-like bursting (SB) solutions that have similar MB solution patterns [30]. Furthermore, previous work has suggested that the Na^+/K^+ pump, in addition to I_{NaP} and I_{CAN} , plays an important role in the generation of the MB solution, yet this is not considered in the system we have studied [56, 30]. Hence, in this Chapter, we focus on this more complicated model including additional multi-scale forms of dynamics seen in respiratory neurons and synaptic coupling and exhibiting I_{NaP} , I_{Ca} , Ca^{2+} oscillations, and the Na^+/K^+ pump current.

In contrast to previous mathematical models investigating the possible roles of I_{NaP} -dependent and I_{CAN} -dependent bursting mechanisms, in which these currents were included together in the same model of single pre-BötC neurons [73, 47, 80], Jasinski et al. [30] mainly considered models of heterogeneous neural populations. In fact, simulations in [30] showed that at the single-neuron level, sigh-like bursting (SB) solutions no longer exist. Furthermore, the Na^+/K^+ pump is needed to generate the SB solution. Therefore, while the MB solution and the SB solution appear to be quite similar (Figure 4.1), they may have very different bursting mechanisms. Besides understanding the mathematical mechanisms, we are also interested in knowing whether the generation of SB

solutions requires the third timescale or not.

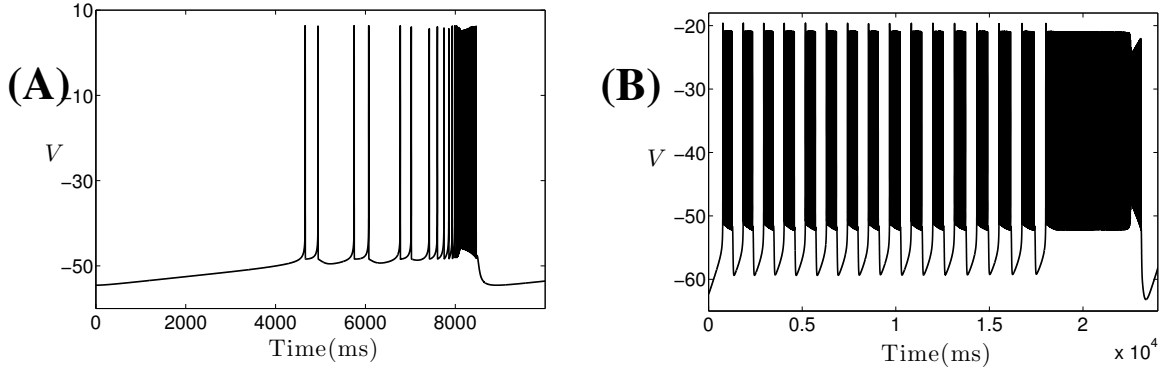


Figure 4.1: Mixed bursting solution (A) and sigh-like bursting solution (B) from [80] and [30], respectively.

To facilitate the identification of the essential mechanisms underlying the SB behavior and the assessment of how to group timescales, we consider a self-coupled model neuron based on the network model presented in [30], which we refer to as the *Jasinski model*:

$$(4.1a) \quad C \frac{dV}{dt} = -I_{Na} - I_{NaP} - I_K - I_{Ca} - I_{CAN} - I_{Pump} - I_L - I_{SynE}$$

$$(4.1b) \quad \frac{dy}{dt} = (y_{\infty}(V) - y)/\tau_y(V), \quad y = \{m_{Na}, h_{Na}, m_{NaP}, h_{NaP}, m_{Ca}, h_{Ca}, m_K\}$$

$$(4.1c) \quad \frac{ds}{dt} = ((1 - s)s_{\infty}(V) - s)/\tau_s(V)$$

$$(4.1d) \quad \frac{dNa_i}{dt} = -\alpha_{Na}(I_{Na} + I_{NaP} + I_{CAN} + 3I_{pump})$$

$$(4.1e) \quad \frac{dCa_{tot}}{dt} = -\alpha_{Ca}I_{Ca} - Ca_i/\tau_{Ca}$$

$$(4.1f) \quad \frac{dCa_i}{dt} = -\alpha_{Ca}I_{Ca} - Ca_i/\tau_{Ca} + K_{Ca}(J_{ERIN} - J_{EROUT})$$

$$(4.1g) \quad \frac{dl}{dt} = AK_d(1 - l) - A[Ca]l$$

The conductance-based single-compartment model of a single neuron was developed in the Hodgkin-Huxley style. The neuronal membrane potential (V) is defined by a set of membrane ionic currents, as shown in (4.1a). C is neuronal membrane capacitance and t is time. The ionic

currents in the model include fast Na^+ , persistent Na^+ , delayed rectifier K^+ , high-voltage-activated Ca^{2+} , Ca^{2+} -activated nonspecific cation, Na^+/K^+ pump, leakage and excitatory synaptic currents (see Table 4.1).

Table 4.1: Ionic currents and channel reversal potentials

Currents	Reversal potentials
$I_{\text{Na}} = \bar{g}_{\text{Na}} \cdot m_{\text{Na}}^3 \cdot h_{\text{Na}} \cdot (V - E_{\text{Na}})$ $I_{\text{NaP}} = \bar{g}_{\text{NaP}} \cdot m_{\text{NaP}} \cdot h_{\text{NaP}} \cdot (V - E_{\text{Na}})$	$E_{\text{Na}} = (R \cdot T/F) \cdot \ln(\text{Na}_o/\text{Na}_i)$
$I_{\text{K}} = \bar{g}_{\text{K}} \cdot m_{\text{K}}^4 \cdot (V - E_{\text{K}})$	$E_{\text{K}} = (R \cdot T/F) \cdot \ln(\text{K}_o/\text{K}_i)$
$I_{\text{Ca}} = \bar{g}_{\text{Ca}} \cdot m_{\text{Ca}} \cdot h_{\text{Ca}} \cdot (V - E_{\text{Ca}})$	$E_{\text{Ca}} = (R \cdot T/2F) \cdot \ln(\text{Ca}_o/\text{Ca}_i)$
$I_{\text{CAN}} = \bar{g}_{\text{CAN}} \cdot m_{\text{CAN}} \cdot (V - E_{\text{CAN}})$	$E_{\text{CAN}} = 0$
$I_{\text{Pump}} = R_{\text{Pump}} \cdot (\varphi(\text{Na}_i) - \varphi(\text{Na}_{i\text{eq}}))$, where $\varphi(x) = x^3/(x^3 + K_{\text{P}}^3)$	
$I_{\text{L}} = g_{\text{L}} \cdot (V - E_{\text{L}})$	$E_{\text{L}} = -68$
$I_{\text{SynE}} = (g_{\text{SynE}} \cdot s + g_{\text{tonic}}) \cdot (V - E_{\text{SynE}})$	$E_{\text{SynE}} = -10$

Activation (m) and inactivation (h) variables for most ionic channels are described as (4.1b), where steady-state activation (m_{∞}) and inactivation (h_{∞}) and their time constants are described as in Table 4.2. Notice from the bottom row in Table 4.2 that different from all other currents, I_{CAN} has instantaneous activation, which depends on Ca_i and is voltage-independent. The parameters for these currents are specified in Table 4.3.

Table 4.2: Activation and inactivation variables

gating variables	steady state activation and inactivation	time constants
m_{Na}	$y_{\infty}(V) = 1/(1 + \exp(-(V - V_{y1/2})/k_y))$	$\tau_y(V) = \tau_{y\text{max}}/\cosh(-(V - V_{\tau y1/2})/k_{\tau y})$
h_{Na}		
m_{NaP}		
h_{Na}		
m_{Ca}		
h_{Ca}	$\tau_{m_{\text{Ca}}} = 0.5 \text{ ms}$	$\tau_{h_{\text{Ca}}} = 18 \text{ ms}$
m_{K}	$m_{\infty} = \alpha_{\infty}/(\alpha_{\infty} + \beta_{\infty})$	$\tau_{\infty} = 1/(\alpha_{\infty} + \beta_{\infty})$
	$\alpha_{\infty} = A_{\alpha} \cdot (V + B_{\alpha})/(1 - \exp(-(V + B_{\alpha})/k_{\alpha}))$, $\beta_{\infty} = A_{\beta} \cdot \exp(-(V + B_{\beta})/k_{\beta})$	
m_{CAN}	$m_{\text{CAN}} = 1/(1 + (K_{\text{CAN}}/\text{Ca}_i)^n)$	

The intracellular concentration of free Ca^{2+} (Ca_i) is described by (4.1f), the right part of which consists of four terms. The first two terms form the right hand side of the equation for the dynamics of the total intracellular Ca^{2+} concentration within the cell (see (4.1e)), which differs from the mixed bursting model in which Ca_{tot} is assumed to be constant. The latter two terms are exactly

Table 4.3: Activation and inactivation variables

Current	Parameters
Fast Na^+	$\bar{g}_{\text{Na}} = 150 \text{ nS}$
I_{Na}	$V_{m1/2} = -43.8 \text{ mV}, k_m = 6 \text{ mV}, \tau_{mmax} = 0.25 \text{ ms},$ $V_{\tau m1/2} = -43.8 \text{ mV}, k_{\tau m} = 14 \text{ mV}$ $V_{h1/2} = -67.5 \text{ mV}, k_h = -10.8 \text{ mV}, \tau_{hmax} = 8.46 \text{ ms},$ $V_{\tau h1/2} = -67.5 \text{ mV}, k_{\tau h} = 12.8 \text{ mV}$
Persistent	$g_{\text{NaP}} = 0 \text{ nS}$
Na^+	$V_{m1/2} = -47.1 \text{ mV}, k_m = 3.1 \text{ mV}, \tau_{mmax} = 1 \text{ ms},$ $V_{\tau m1/2} = -47.1 \text{ mV}, k_{\tau m} = 6.2 \text{ mV}$
I_{NaP}	$V_{h1/2} = -60 \text{ mV}, k_h = -9 \text{ mV}, \tau_{hmax} = 5000 \text{ ms},$ $V_{\tau h1/2} = -60 \text{ mV}, k_{\tau h} = 9 \text{ mV}$ In the case of non-inactivating $I_{\text{NaP}}, h = \text{constant} = 0.4$
K^+ delayed rectifier	$\bar{g}_{\text{K}} = 160 \text{ nS}$
I_{K}	$A_\alpha = 0.01, B_\alpha = 44 \text{ mV}, k_\alpha = 5 \text{ mV}, A_\beta = 0.17,$ $B_\beta = 49 \text{ mV}, k_\beta = 40 \text{ mV}$
Ca^{2+}	$\bar{g}_{\text{Ca}} = 0.00065 \text{ nS}$
I_{Ca}	$V_{m1/2} = -27.5 \text{ mV}, k_m = 5.7 \text{ mV}, \tau_m = 0.5 \text{ ms},$ $V_{h1/2} = -52.4 \text{ mV}, k_h = -5.2 \text{ mV}, \tau_h = 18 \text{ ms}$
Ca^{2+} -activated nonspecific I_{CAN}	$\bar{g}_{\text{CAN}} = 3 \text{ nS}, K_{\text{CAN}} = 0.00074 \text{ mM}, n = 0.97$
Na^+/K^+ pump I_{pump}	$R_{\text{pump}} = 200 \text{ pA}, \text{Na}_{\text{ieq}} = 15 \text{ mM}, K_p = 15 \text{ mM}$
Leakage I_L	$g_L = 2.5 \text{ nS}$
Excitatory synaptic I_{SynE}	$g_{\text{SynE}} = 20 \text{ nS}, g_{\text{tonic}} = 0.78 \text{ nS}$

the same as the right part of the equation for calcium in the mixed bursting model (compare (4.1f) with (3.1d)), so is the dynamics for l (compare (4.1g) with (3.1e)). Correspondingly, parameters associated with $J_{\text{ERin}}, J_{\text{ERout}}$ as specified in (3.2) and the equation for l are the same as given in Table 3.1 in Chapter 3, except $[\text{IP}_3] = 1.5 \mu\text{M}$. For convenience, we henceforth omit units on the parameter and variable values.

At the single-neuron level (when the self-coupling is removed by setting $g_{\text{SynE}} = 0$), this model can produce two types of intrinsic bursting behaviors, depending on chosen parameter values, similar to the mixed bursting model. One type of bursting (I_{NaP} -dependent bursting) is based on the slow voltage-dependent inactivation of I_{NaP} (as represented by the h_{NaP} variable in the equation for I_{NaP} in Table 4.1), whereas the other type (I_{CAN} -dependent bursting) relies on intracellular Ca^{2+} . Various distinct burst-terminating mechanisms based on the slow inactivation of I_{NaP} , the activity-dependent accumulation of Na^+ followed by the $[\text{Na}^+]_{\text{in}}$ -activated I_{pump} , and the Ca^{2+} -dependent inactivation of IP3R, respectively, exist this bursting neuron model.

In the presence of synaptic coupling between neurons (i.e., $g_{SynE} > 0$), the coupled cells are able to generate SB solutions. In this chapter, we consider the special case of a single self-coupled cell model (4.1) as a reduction of coupled network. Numerical simulations show that both mechanisms based on I_{CAN} and I_{Pump} contribute to the generation of SB solutions, without the need of I_{NaP} (e.g. SB solution dynamics will not be abolished at $\bar{g}_{NaP} = 0$, but will be lost without CAN and Pump currents). The left panel of Figure 4.2 demonstrates one cycle of SB solution patterns as well as changes in other relevant variables: Ca_i , Na_i , Ca_{tot} and l . Specifically, there exist low-amplitude Ca_i and Na_i transients during regular bursts followed by the jump up of intracellular Ca^{2+} , due to which Na_i also exhibits high-amplitude transients. Besides, Ca_{tot} and l that are confined to the calcium subsystem (Ca_i, Ca_{tot}, l) both accumulate until Ca_i jumps up. After that, they start decreasing. The right panel of Figure 4.2 shows burst details that Ca_i , Na_i and Ca_{tot} engage in small oscillations during the spiking phase of each regular burst since these variables receiving input from V are perturbed by the voltage spike: they tend to increase as V reaches its maximum and decrease as V oscillates to the minimum.

While the mixed bursting and Jasinski models generate similar solution patterns, the latter is much more complicated than the former one in the sense that: first, (4.1) has one extra Na^+/K^+ pump-based burst-terminating mechanism, yet this is not considered in Chapter 3; second, instead of one-directional coupling used in the mixed bursting model such that the model can be thought of as one oscillator forcing another, membrane potential and cytoplasmic Ca^{2+} concentration in (4.1) can each influence each other, so can membrane potential and intracellular Na^+ concentration; and third, in contrast to the model in Chapter 3, (4.1) incorporates and simulates more realistic and detailed kinetics of the intracellular Ca^{2+} release. These complications and high dimension of (4.1) (consisting of 13 variables) make the mathematical analysis of the Jasinski model quite challenging.

One of the primary goals of this Chapter is to provide a thorough mathematical analysis of the mechanisms underlying the SB solution. To this end, we will nondimensionalize to reveal the presence of different timescales and identify how to group timescales in our model; implement geometric singular perturbation theory to set up reduced systems based on separation of timescales; and use the reduced systems to explain the mechanisms underlying the dynamics of SB solutions.

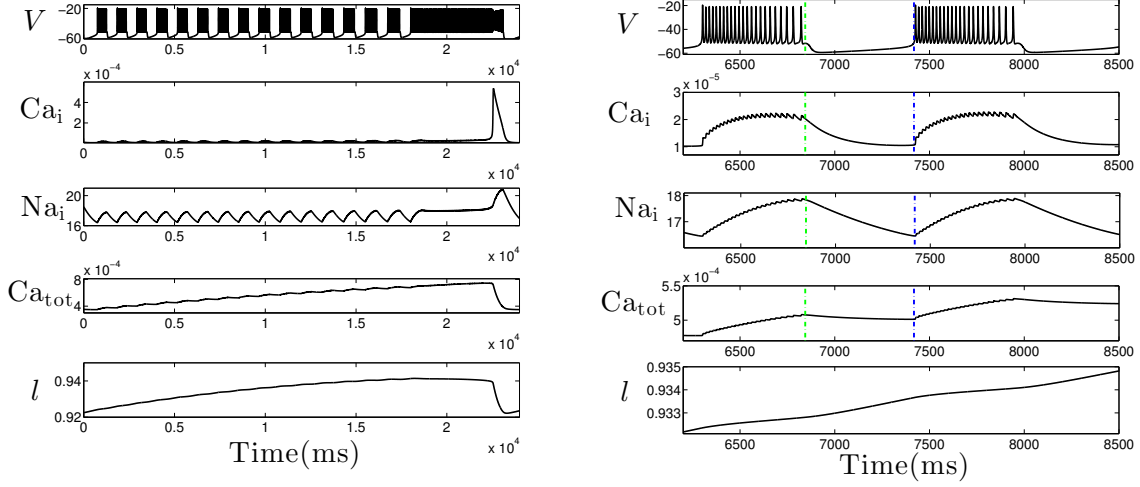


Figure 4.2: Simulation of sigh-like rhythmic bursting of the Jasinski model. From top to bottom: changes in membrane potential, calcium, sodium, total intracellular calcium concentration within the cell (Ca_{tot}) and IP_3 channel gating variable l . This SB pattern repeats periodically. The right panel shows the details of the regular small burst, where the dashed green and blue lines denote the end and the beginning of the regular burst, respectively.

4.1 ANALYSIS OF SIGH-LIKE BURSTING

In this section, we analyze how various bursting mechanisms described above interact to produce the SB solution, in the presence of self-excitation. As noted before, the SB solution dynamics will not be abolished at $\bar{g}_{NaP} = 0$, i.e., I_{NaP} is not required in the Jasinski model for SB solutions. In light of this, we can reduce (4.1) to a 11-dimensional system by removing m_{NaP} and h_{NaP} and setting $I_{NaP} = 0$ in the equation (4.1a). Henceforth, we still refer to Jasinski model (4.1) as the new lower dimensional model without involvement of I_{NaP} . Moreover, similar to the findings in [30], numerical simulations of (4.1) indicate that the regular bursting is independent of I_{CAN} as it will not be abolished at $\bar{g}_{CAN} = 0$. However, assigning $\bar{g}_{Ca} = 0$ or $\bar{g}_{CAN} = 0$ fully removes the sigh-like oscillations, confirming that the generation of sigh-like bursts in this model is I_{Ca}/I_{CAN} -dependent. Similarly, setting $I_{Pump} = 0$ will lose both regular bursting and sigh-like oscillations,

implying that the Na^+/K^+ pump-based bursting mechanism is also involved. In conclusion, the burst terminating mechanisms involved in the SB solution are depending on both Ca^{2+} -dependent IP3R inactivation and I_{Pump} activation. In the following, we aim to provide a mathematical analysis of how these two bursting mechanisms operate together to generate SB solutions.

The fact that both MB and SB solutions result from the interaction of two bursting mechanisms highlights the possibility that analysis for understanding MB solutions may be carried over similarly to the SB solution. Despite sharing one common burst terminating mechanism based on intracellular Ca^{2+} , these two solutions differ by the second operating burst-terminating mechanisms that the MB solution is based on I_{NaP} inactivation, while the SB solution is I_{Pump} -based. In Chapter 3, we analyzed the MB solution from a perspective of one potentially burster (depending on I_{NaP}) driven by an intrinsically oscillating subsystem (Ca^{2+} oscillations). In the Jasinski model, previous finding that regular burst depends on I_{Pump} while is independent of I_{CAN} or I_{Ca} suggests that we can decouple V , Na_i from the calcium dynamics while regular bursting still persists. Hence, we divide the Jasinski system into two subsystems: the system of equations (4.1a)-(4.1d) (denoted as the *voltage subsystem*) as a potentially bursting subsystem and the system of equations (4.1e)-(4.1g) (denoted as the *calcium subsystem*) as a potentially oscillating subsystem. With these two subsystems, we adopt the approach used in Chapter 3 to explain the mechanisms underlying the dynamics of the SB solution. We first investigate the I_{Pump} -based mechanism underlying the regular burst generated by the voltage subsystem through a bifurcation analysis and then study the effect of $(\text{Ca}^{2+}, \text{Ca}_{\text{tot}}, l)$ subsystem on the resulting bifurcation structures to understand how the transition from regular bursts to the long burst happens.

Our methods for analysis of the model will depend heavily on exploiting the presence of different timescales. As a first step, it is helpful to rescale the variables so that the important timescales can be explicitly identified. To this end, we nondimensionalize the model (details of the nondimensionalization procedure are given in Appendix 6.4, with the timescales for all variables shown in Table 6.1). While V , gating variables ($m_{\text{Na}}, h_{\text{Na}}, m_{\text{Ca}}, h_{\text{Ca}}, m_{\text{K}}$) and s are not operating on the same magnitude of timescales, it is clear that they are all relatively faster than others. Hence we choose to group all of them as fast variables, Na_i and Ca_i as slow, whereas l and Ca_{tot} as evolving on a superslow timescale. For simplicity, we abuse notation to let $y \in \mathbb{R}^6$ denote all the fast gating variables and s . Using these information, we can now split our model into fast, slow and super-

slow subsystems. The procedure of setting up reduced systems is similar to what we have done in Chapter 2 and hence is omitted here. The *fast subsystem* (V, y) consists of the equations for the fast variables with both slow variables Ca_i and Na_i treated as static parameters of the system. Since changes in Ca_{tot} and l affect the fast subsystem indirectly, they are not considered as parameters for this subsystem. The Jasinski model (4.1) also has a two-dimensional *slow subsystem* consisting of the equations for Ca_i and Na_i with both superslow variables Ca_{tot} and l fixed. Moreover, we find it useful to work with the system consisting of all the fast and slow variables with superslow variables fixed, which we denote as the *fast-slow subsystem*: (V, y, Ca_i, Na_i) .

As noted before, we will explain the mechanism from the perspective of how the I_{Pump} -based burster is driven by the calcium subsystem. To do so, we first investigate the coupling effect between them. When decoupled from Ca^{2+} by setting $g_{Ca} = g_{CAN} = 0$, the bifurcation diagram for the (V, y, Na_i) system is shown in Figure 4.3A, including an S-shaped curve equilibria (S) and a family of stable periodic orbits (P) that initiates in a supercritical Andronov-Hopf (AH) bifurcation and terminates in homoclinic (HC) bifurcation involving the middle branch of S. Hence, in the absence of calcium dynamics, this subsystem is capable of generating a square-wave bursting solution, the terminating mechanism of which is depending on the accumulation Na_i and subsequent activation of the Na_i -dependent Na/K^+ pump.

In the calcium subsystem (Ca_i, Ca_{tot}, l) , the dynamics of Ca^{2+} depends on the neuronal membrane potential V . Hence, instead of exhibiting relaxation oscillations involving jumps in Ca_i between branches of the Ca_i -nullcline alternating with the drift in (Ca_i, Ca_{tot}, l) along these branches, there exist small oscillations during each regular burst (see Figure 4.3C and the trace for Ca_i in Figure 4.2). Such patterns arise because the Ca_i -nullsurface moves back and forth between the two surfaces as V oscillates between the minimum and maximum during the spiking phase of each burst (Figure 4.3B and C). During the regular bursts, there is a low amplitude transient in Ca_i before it jumps up to the right branch, as noted before. Figure 4.3B shows that these two surfaces corresponding to V at its minimum and maximum values lie close to each other due to the insensitive dependence of I_{Ca} on V for calcium large. As a result, the trajectory bounded between the two right branches is approximately evolving along the right branch of the Ca_i -nullsurface. Ca_i decrease as l decreases until the trajectory jumps back to the left branch. What remains unclear about this loop is to identify the bifurcation corresponding to the jump up of calcium, which should

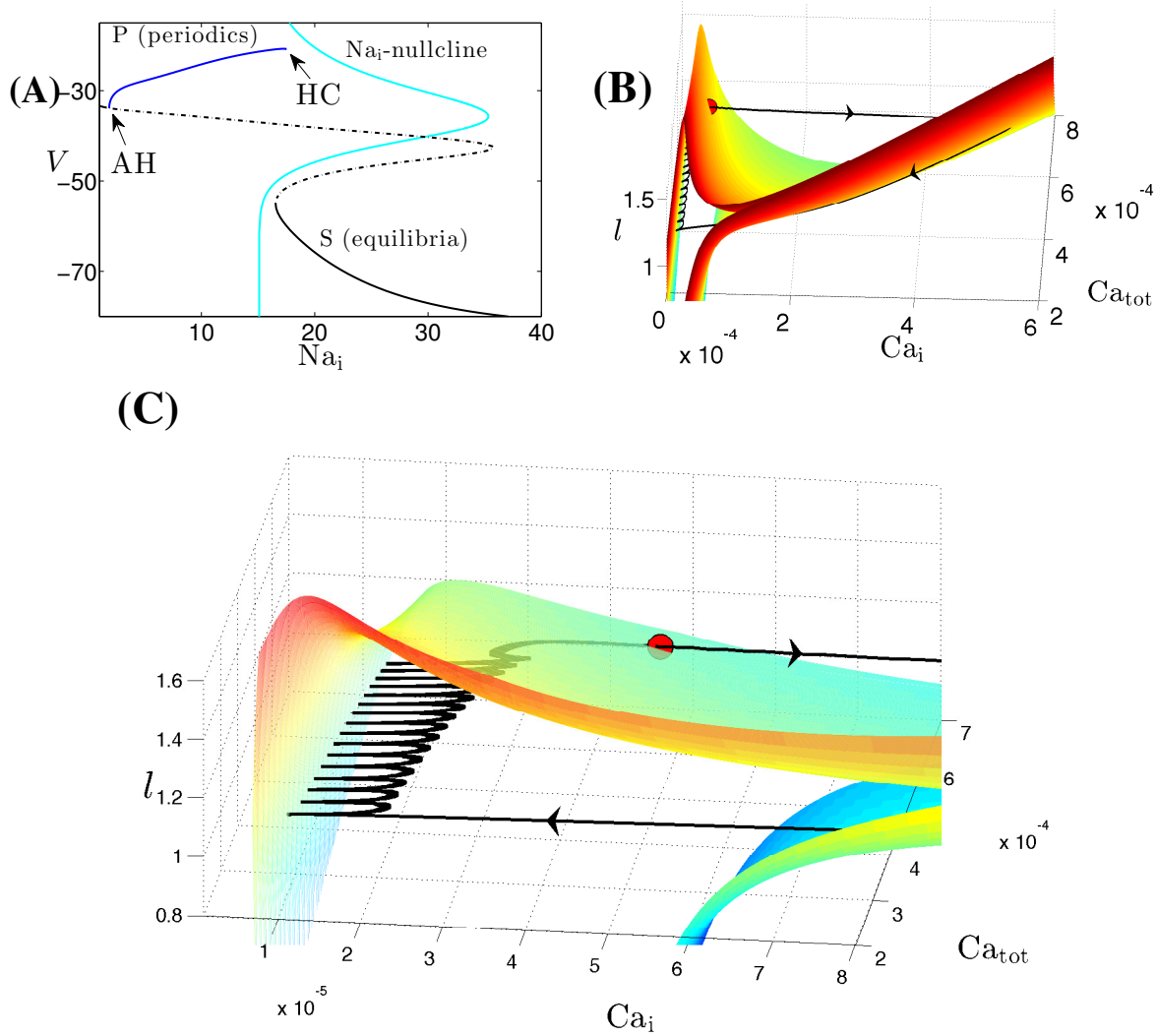


Figure 4.3: Basic structures of the voltage subsystem (4.1a)-(4.1d) and the calcium subsystem (4.1e)-(4.1g). The first subsystem decouples from the calcium subsystem (Ca_i, Ca_{tot}, l) by setting $g_{Ca} = g_{CAN} = 0$. (A): Projection onto (Na_i, V) -space of the bifurcation diagram for the first subsystem along with the Na_i -nullcline shown in cyan. The black solid (resp., dashed) curve S denotes the stable (resp., unstable) fixed points of the Fast system with Na_i taken as a constant parameter, and the blue curve shows the maximum V along the family of periodics (P). (B): Nullsurfaces of Ca_i for the calcium subsystem with V at their minimum (upper surface) and maximum (lower surface), in (Ca_i, Ca_{tot}, l) -space. The black curve denotes the SB solution trajectory of the Jasiniski model. The right branches of these two nullsurfaces lie close to each other. (C): An enlarged view of (B). The trajectory jumps up to the right branch of the nullsurface of Ca_i near the red dot.

no longer be through the saddle-node bifurcation of the calcium subsystem as before.

With the choice of $g_{Ca} = 0.00065$ and $g_{CAN} = 3$, the coupling from calcium dynamics to the voltage has been resumed and as a result, the Jasinski model generates a SB solution. An example the coupling effect can be seen in Figure 4.4A: the increase of Ca_i will shift the bifurcation diagram to the right.

In the following, we will first explain the mechanism underlying the small bursts in the SB solution and then elucidate how the transition to a sigh-like burst occurs, from the perspective of how the I_{Pump} -based burster is driven by the calcium subsystem (Ca^{2+}, Ca_{tot}, I) .

4.1.1 Mechanisms underlying regular bursting

In Figure 4.4B, we project the first regular burst solution and the bifurcation diagram of the fast subsystem for Ca_i fixed at $8e - 6$, corresponding to its value at the beginning of this first small burst, onto (Na_i, V) -space. Also shown is the green (resp. blue) dashed line representing the Na_i values at which the homoclinic (resp. lower fold of equilibria) bifurcation occurs. Starting from the yellow star, the trajectory moves on the slow timescale associated with Na_i along the stable lower branch of the bifurcation diagram until it reaches the lower fold. After that, the trajectory jumps up to the stable periodic orbit branch and then moves to the right, since the trajectory stays above the Na_i -nullcline. After crossing the homoclinic bifurcation at the Na_i value indicated by the green dashed line, the trajectory will jump down to the lower branch of equilibria, completing a small burst. Notice that several more spikes happen after passing the green dashed line, which is because during the first regular burst period, Ca_i progressively increases on a slow timescale. As a result, the bifurcation diagram will also move rightward on a slow timescale associated with the increase of Ca_i . Hence at the end of the burst, the homoclinic bifurcation occurs at some larger Na_i value to the right of the green dashed line in Figure 4.4B. Therefore several more spikes are yielded after the green dashed line. Such square-wave bursting solutions will repeat until roughly when Ca_i starts jumping up to larger values as indicated in Figure 4.2.

Understanding of the persistence of the regular bursts and the mechanism by which a transition to the sigh-like burst occurs requires us to consider the effect of Ca_i on the I_{Pump} -based burster. To do so, we use Ca_i as the second bifurcation parameter and allow both Ca_i and Na_i to vary in

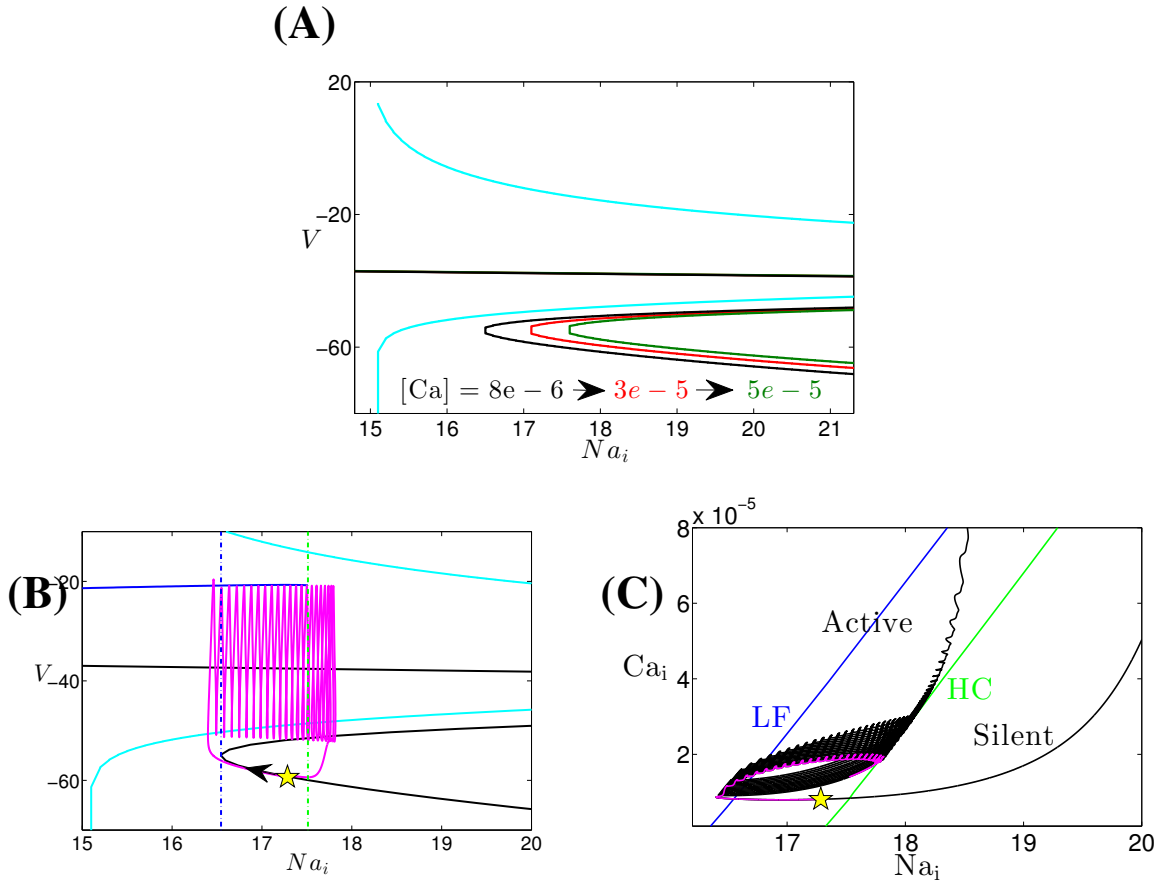


Figure 4.4: Bifurcation diagrams of the Fast system (4.1a)-(4.1c) with the slow variables Na_i and Ca_i taken as static parameters. The yellow symbol marks the start point of the SB solution. (A): The effect of Ca_i on the bifurcation diagram for the Fast system, projected into (Na_i, V) -space, along with the Na_i -nullcline (cyan). Increasing Ca_i from $8e-6$ to $3e-5$ to $5e-5$ results in a shift of the bifurcation diagram to the right (black to blue to green). (B): Projection of the first small burst in the SB solution from (A) onto the bifurcation diagram (with $Ca_i = 8e-6$) in (Na_i, l) -space, along with the Na_i -nullcline (cyan). The blue and green dashed lines indicate the Na_i values where the lower fold and homoclinic bifurcations occur, respectively. (C): The curve of saddle-node bifurcations corresponding to the lower fold of the bifurcation diagram (blue), homoclinic bifurcation curve (green) and part of the trajectory (black) from (A) in (Na_i, Ca_i) -space. The green curve acts as the boundary of the oscillation region for the Fast system.

order to find the two-parameter bifurcation curves of the fast subsystem (V, y) in the (N_{a_i}, C_{a_i}) parameter plane that unify the results in Figure 4.4A, as illustrated in Figure 4.4C. The blue (resp. green) curve in this plane is the curve of lower fold (LF) (resp. homoclinic (HC)) bifurcations, which initiates (resp. terminates) each burst, as noted previously. Since the increase of C_{a_i} moves the bifurcation diagram to the direction of increasing N_{a_i} , both curves of LF and HC are positively sloped in the (N_{a_i}, C_{a_i}) -space. Within the same projection, the trajectory evolves leftward from the yellow star and it starts oscillating as it passes the LF curve (see Figure 4.4C). These oscillations terminate when the trajectory reaches the HC bifurcation curve, which completes the first regular burst. Similarly, a sequence of subsequent regular bursts occurs, with the local maximum of N_{a_i} progressively increasing due to the right drift of LF as C_{a_i} accumulates. The fact that the trajectory in (N_{a_i}, C_{a_i}) -space crosses the LF and HC 15 times corresponds to the existence of the 15 regular bursts (see Figure 4.2). After that, bursting solutions give way to continuous spiking.

Based on the fast subsystem bifurcation structures in this section, we demonstrate that regular bursts occur as the slow variables C_{a_i} and N_{a_i} traverse the phase space back and forth between the LF and HC curves. The reason why regular bursts switch to the sigh-like burst, however, remain unknown. To figure this out, we notice that after multiple crossings with the HC curve in Figure 4.4C, the trajectory projected to (N_{a_i}, C_{a_i}) space starts oscillating near the HC curve, instead of going back to quiescence state. Moreover, this transition happens before C_{a_i} jumps up. Hence, the switch from regular bursts to the long burst in the full system seems to correspond to the transition from bursting to tonic spiking in the fast-slow subsystem (V, y, N_{a_i}, C_{a_i}) , rather than the jumping up of C_{a_i} as in the mixed bursting model.

4.1.2 Mechanisms underlying the transition from regular bursts to the sigh-like burst

In the analysis up to this point, superslow variables have not been considered yet. It is natural to expect that the superslow evolution of these two variables may contribute to the switch from bursting to the tonic spiking. A numerical simulation of the fast-slow subsystem over a range of $C_{a_{tot}}$ and l values (Figure 4.5) suggests that superslow variables do play an important role in inducing a transition from bursting to tonic spiking in the fast-slow subsystem. In Figure 4.5 (top panel), representative time traces for bursting and tonic spiking solutions are shown for a fixed

value of l . For small $C_{a_{tot}}$, the fast-slow system is in a bursting state (Figure 4.5, top left). When $C_{a_{tot}}$ is increased, tonic spiking solutions arise (Figure 4.5, top middle). A further increase in $C_{a_{tot}}$ does not change the tonic spiking in V (Figure 4.5, top right), but both C_{a_i} and N_{a_i} oscillate at higher values than in (A) and (B). A graphical summary of the effect of $C_{a_{tot}}$ variations on the trajectories is provided in panel (D), where the bifurcation structure of the fast-slow subsystem with respect to $C_{a_{tot}}$ for $l = 0.94$ was computed. We plot $C_{a_{tot}}$ against the standard Euclidean norm of the solution. As $C_{a_{tot}}$ is increased, the behavior switches from bursting to tonic spiking. The fast-slow system exhibits tristability between the bursting (red solid) and tonic spiking (blue solid) for the small $C_{a_{tot}}$ values. Both branches become unstable at saddle-node bifurcations. The initial conditions are chosen such that the trajectory will be attracted by the stable bursting branch for $C_{a_{tot}} = 0.0006$ (red diamond). As the tristability is lost for bigger $C_{a_{tot}}$ values (e.g., 0.0007 and 0.00074 denoted by the blue diamonds on the upper and lower branches of the spiking solutions, respectively), the behavior switches to tonic spiking. Note that the lower L_2 norm corresponds to larger C_{a_i} and N_{a_i} values, hence as the trajectory gets attracted by the lower branch of spiking after the saddle node bifurcation, the tonic spiking solution occurs at larger C_{a_i} , N_{a_i} values.

To understand the mechanisms underlying the switch from bursting to tonic spiking, we use slow averaged dynamics in the oscillation (bursting or spiking) region to analyze activity states. For convenience, we refer to the two regions of (N_{a_i}, C_{a_i}) space separated by the curve of HC bifurcations which terminates each burst as the silent and active regions (Figure 4.4C).

During the interburst interval of the regular burst cycle, the full model dynamically collapses to a lower-order system governed by the slow variables C_{a_i} and N_{a_i} restricted to the manifold of equilibrium points of the fast subsystem. This interburst interval corresponds to the silent region of (N_{a_i}, C_{a_i}) space. During the spiking phase of each regular burst, the solution trajectory is still largely determined by the slow variables C_{a_i} and N_{a_i} , but these variables are perturbed by the voltage spike and Ca^{2+} -influx associated with each action potential. This spiking phase corresponds to the active region of (N_{a_i}, C_{a_i}) space. In this region we employ the method of average nullclines, a numerical technique in which the derivatives of the slow variables are averaged over one cycle of the action potential, while the superslow variables $C_{a_{tot}}$ and l are treated as the static parameters. By doing so, we reduce the fast-slow subsystem to two equations for just the slow variables. For g_1 and g_2 defined as the right hand sides of (4.1f) and (4.1d), respectively, the reduced system can

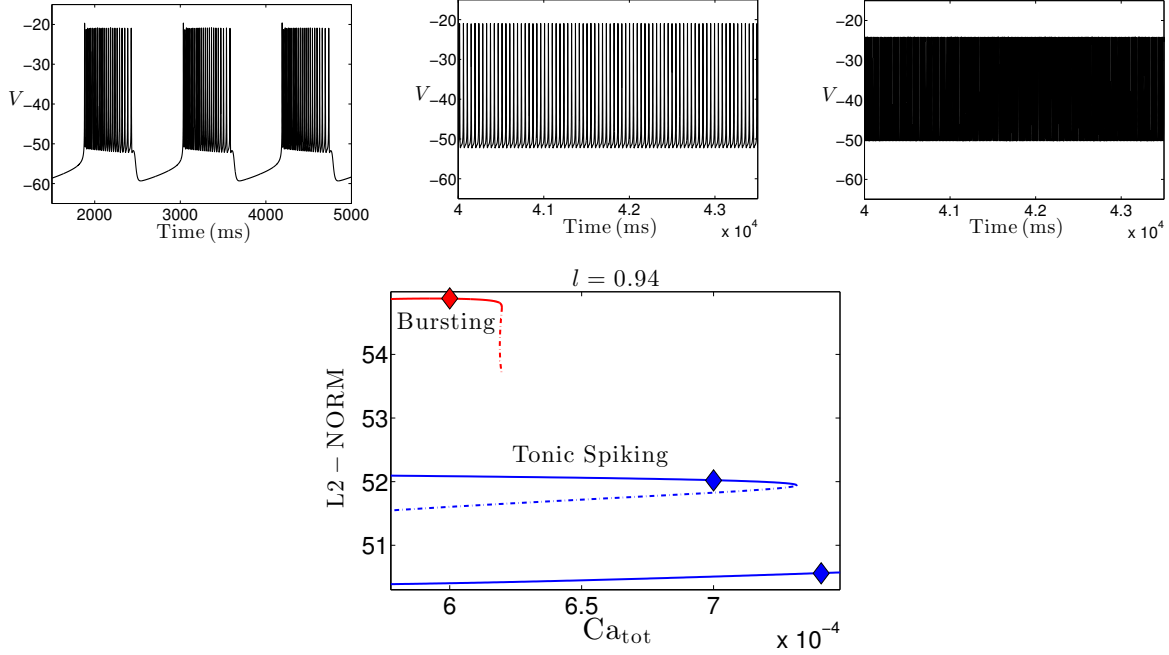


Figure 4.5: Effect of variations in Ca_{tot} on the trajectories of the fast-slow subsystem (V, y, Ca_i, Na_i) for $l = 0.94$. Top row, from left to right: $Ca_{tot} = 0.0006$ (bursting), $Ca_{tot} = 0.0007$ (tonic spiking at low Ca_i and Na_i : $Ca_i \approx 2.5 \times 10^{-5}$, $Na_i \approx 18$) and $Ca_{tot} = 0.00074$ (tonic spiking at high Ca_i and Na_i : $Ca_i \approx 5.7 \times 10^{-4}$ and $Na_i \approx 25.5$). The bifurcation diagram for the fast-slow subsystem with respect to the Ca_{tot} in the bottom row summaries all possible behaviours as Ca_{tot} varies: bursting (red curves) and tonic spiking (blue curves) in which solid means stable, while dashed means unstable. The three diamonds from top to bottom indicate Ca_{tot} values used by the top three panels from left to right, respectively.

be written as

$$(4.2a) \quad \langle \dot{Ca}_i \rangle = \frac{1}{T(Ca_i, Na_i)} \int_0^{T(Ca_i, Na_i)} g_1(V(Ca_i, Na_i; t), Ca_i, Ca_{tot}, l),$$

$$(4.2b) \quad \langle \dot{Na}_i \rangle = \frac{1}{T(Ca_i, Na_i)} \int_0^{T(Ca_i, Na_i)} g_2(V(Ca_i, Na_i; t), Ca_i, Ca_{tot}, l)$$

We refer to the reduced problem (4.2) as the *averaged slow system*. The average Na_i and Ca_i nullclines are steady-state periodic solutions (with period T) of the fast-slow subsystem along with the additional constraint of either $\langle \dot{Ca}_i \rangle = 0$ or $\langle \dot{Na}_i \rangle = 0$. In future discussions of the dynamics of the averaged slow system, we will refer to the Ca_i and Na_i average nullclines as Ca_{av} and Na_{av} , respectively. The intersection of Ca_{av} and Na_{av} , a quasi-steady-state fixed point representing a tonic spiking solution, will be referred to as F_{av} .

Figure 4.6 illustrates phase planes of the average slow system (4.2) for $l = 0.94$ and $Ca_{tot} = 0.0006, 0.0007, 0.00074$ as in Figure 4.5. In each panel of Figure 4.6, the green curve represents the HC bifurcation of the fast subsystem, the boundary of the oscillation region. When a bursting solution crosses HC, it falls back to the silent phase, and spiking activity stops until a subsequent burst cycle begins (Figure 4.4C). Above HC, averaged nullclines Ca_{av} (blue curve) and Na_{av} (green curve) are shown. As noted before, fixed points of (4.2), F_{eq} (yellow diamond), are given by the intersections of these nullclines, and one can usually determine the stability of the fixed points by considering the nullcline configuration.

In Figure 4.6A when $Ca_{tot} = 0.0006$, the two average nullclines intersect at a stable fixed point F_{av1} (yellow diamond), which corresponds to the upper spiking branch in Figure 4.5 (bottom). Despite the existence of stable fixed point (corresponding to stable tonic spiking), the fast-slow subsystem exhibits bursting since our chosen initial values lie in the basin of attraction of the bursting branch. For $Ca_{tot} = 0.0007$, the stability of bursting is lost and hence the trajectory is now attracted by F_{av1} (Figure 4.6B, yellow diamond). Besides the saddle node F_{av2} in the middle, the third fixed point of (4.2) that lies in larger Ca_i and Na_i values corresponding to the lower spiking branch in Figure 4.5 (bottom) is not visible here. As a result, the fast-slow subsystem converging to the lower stable fixed point F_{av1} exhibits tonic spiking. As Ca_{tot} increases further to 0.00074, the lower two fixed points F_{av1} and F_{av2} collide and annihilate each other through a saddle-node bifurcation (Figure 4.6C) and we are only left with the upper stable fixed point F_{av3} (Figure 4.6D, yellow diamond), which corresponds to the lower spiking branch in Figure 4.5 (bottom) as noted before. Therefore, the trajectory jumps up to large Ca_i value on the slow timescale until reaching the average Ca_i nullcline (blue curve). Once there, the trajectory starts moving rightward to the fixed point F_{av3} since $\langle \dot{Ca}_i \rangle$ is nearly 0 while $\langle \dot{Na}_i \rangle$ remains positive. As the trajectory eventually arrives at F_{av3} , a tonic spiking solution results at large Ca_i and Na_i values.

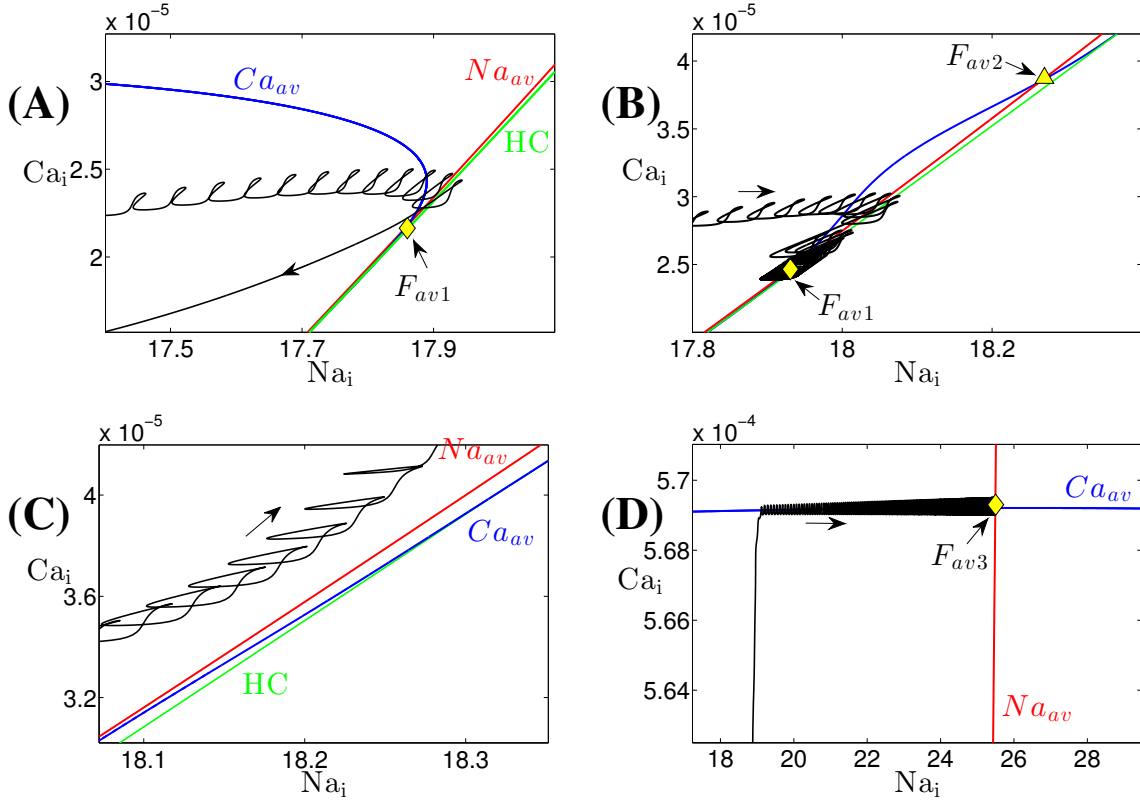


Figure 4.6: Averaged phase planes, corresponding to (4.2), with superimposed trajectories of the Fast-Slow system, for $l = 0.94$ and three different values of Ca_{tot} as in Figure 4.5. Throughout this figure, the curve of HC bifurcations is green, the nullclines Ca_{av} , Na_{av} are blue and red, respectively and the yellow symbols mark the fixed point of the average slow system. The oscillatory trajectories (black) from the top panel of Figure 4.5 are projected to (Na_i, Ca_i) -space in (A), (B) and the lower panel (C, D) in this figure, respectively. For (A) $Ca_{tot} = 0.0006$ and (B) $Ca_{tot} = 0.0007$, there are three fixed points F_{av} above HC where the average nullclines intersect, namely, F_{av1} , F_{av3} which are stable, and F_{av2} , which is unstable. Here not all three fixed points are visible in (A) as well as (B) since some of them lie at larger (Na_i, Ca_i) values than those shown in these two plots. (C) and (D): Enlarged views of phase plane for $Ca_{tot} = 0.00074$ showing that both F_{av1} and F_{av2} vanish and the only average fixed point left (F_{av3} , with high Na_i and Ca_i) is stable. Specifically, panel (C) (resp. (D)) shows the enlarged lower left (resp. upper right) region of the phase plane.

Using slow averaged dynamics, we have elucidated how the transition from bursting to tonic spiking occurs and why Ca_i jump ups to larger values as Ca_{tot} increase for l fixed. Similarly, we summarize the effects of Ca_{tot} on the average slow system by using bifurcation analysis as shown in Figure 4.7. Again, the upper (resp. lower) branch of the bifurcation diagram in L_2 norm corresponds to the lower (resp. upper) branch in Ca_i as well as Na_i and hence solutions in this branch denote F_{av1} (resp. F_{av3}). The middle branch represents the unstable saddle F_{av2} (see Figure 4.6B). Notice that Figure 4.7 looks qualitatively the same as the tonic spiking branch shown by the blue curve in Figure 4.5 (bottom), hence both can be used to illustrate the influence of Ca_{tot} on the oscillatory trajectories for fixed value of l . As Ca_{tot} is increased, calcium jumps up at a saddle-node (SN) of either the tonic spiking branch in Figure 4.5 (bottom) or the branch of average fixed points in Figure 4.7. On the other hand, the onset of spiking happens at a SN of the bursting branch (Figure 4.5 (bottom), red curve). Next we extend this bifurcation analysis and examine the dependence of the solution patterns of the fast-slow system on both Ca_{tot} and l . To do this, we compute two-parameter bifurcation diagrams in (Ca_{tot}, l) -space.

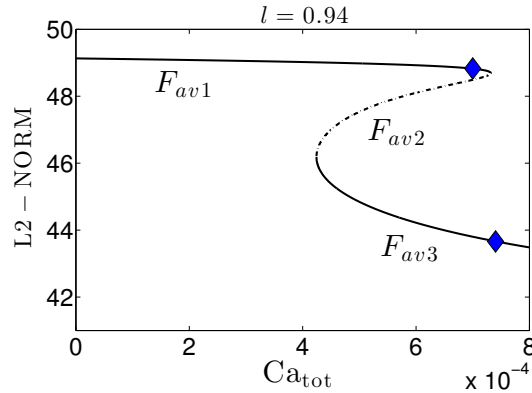


Figure 4.7: Bifurcation diagram of the average slow system (4.2) with respect to Ca_{tot} with l fixed at 0.94. The Ca_{tot} values for the blue diamond marker points from upper to lower are $Ca_{tot} = 0.0007$ (as in Figure 4.6B) and 0.00074 (as in Figure 4.6C, D), respectively.

In Figure 4.8C, the spiking/bursting boundary (solid red, SN_1) was calculated by following in 2 parameters the SN point where the bursting branch loses stability (Figure 4.5 (bottom), the SN of the red curve). Also shown is the boundary (solid blue, SN_2) denoting the onset of jump-

ing up of Ca_i (also computed by following in (Ca_{tot}, l) the upper fold point of the tonic spiking branch in Figure 4.5 (bottom)). We can also use direct simulation of the fast-slow subsystem (e.g., fixing Ca_{tot} , varying l systematically, and then repeating for a different Ca_{tot}), to estimate the bursting/spiking boundary curve and the onset of the jump up in calcium (shown in dashed red and blue). The distance between the solid red (resp. blue) and the dashed red (resp. blue) will be shortened as we exaggerate the timescale separation between the fast-slow subsystem and the superslow variables.

Together with fast subsystem bifurcation structures as illustrated in Figure 4.4B, and reproduced in Figure 4.8B, we are now able to fully understand the SB solution. Starting from the yellow star at low Ca_{tot} and l (Figure 4.8C), a sequence of small bursts is produced as the trajectory in (Ca_i, Na_i) -space reaches the LF and HC curves multiple times (Figure 4.8B). This process should be terminated as the increases of Ca_{tot} and l push the trajectory in (Ca_{tot}, l) -space across the SN_1 , entering the tonic spiking regime, as we discussed before. Nonetheless, several more small bursts actually occur after passing the SN_1 and are followed by the start of tonic spiking at the triangle. In the singular limit, however, this additional bursting will be lost and the tonic spiking occurs after passing SN_1 . In (Ca_{tot}, l) -space, the trajectory evolves rightward from the triangle and eventually passes the SN_2 curve at some point close to the yellow circle which initiates the jump up of Ca_i (Figure 4.8C). The slow increase in Ca_i as well as in Na_i can be seen in panel (B) showing the trajectory in (Na_i, Ca_i) -space jumps to the upper right from the yellow circle, corresponding to the trajectory projected into (Ca_i, Ca_{tot}, l) -space converging to the right branch of the Ca_i -nullsurface and reaching the maximum of Ca_i (Figure 4.3B). For Ca_i big, the trajectory in (Ca_i, Ca_{tot}, l) -space is bounded by two nearly overlapping surfaces (see Figure 4.3B) and lies above the l -nullsurface (not shown here), consequently, l will decrease, leading to the reduction of Ca_i . Therefore, the trajectory in (Na_i, Ca_i) -space falls back from the peak in Ca_i direction and moves towards HC. Once crossing the HC bifurcation curve at the yellow square, the long burst will be terminated and the trajectory enters the silent phase. As the solution finally returns to the starting point, one cycle of the SB solution is completed.

Remark 4. *Just as the MB solution, after Ca_i jumps up at the yellow circle, there exists a sudden decrease in the amplitude of the V spikes, followed by spikes with incrementing amplitudes (Figure 4.8A). This feature arises because the voltage subsystem in the Jasiniski model share a similar*

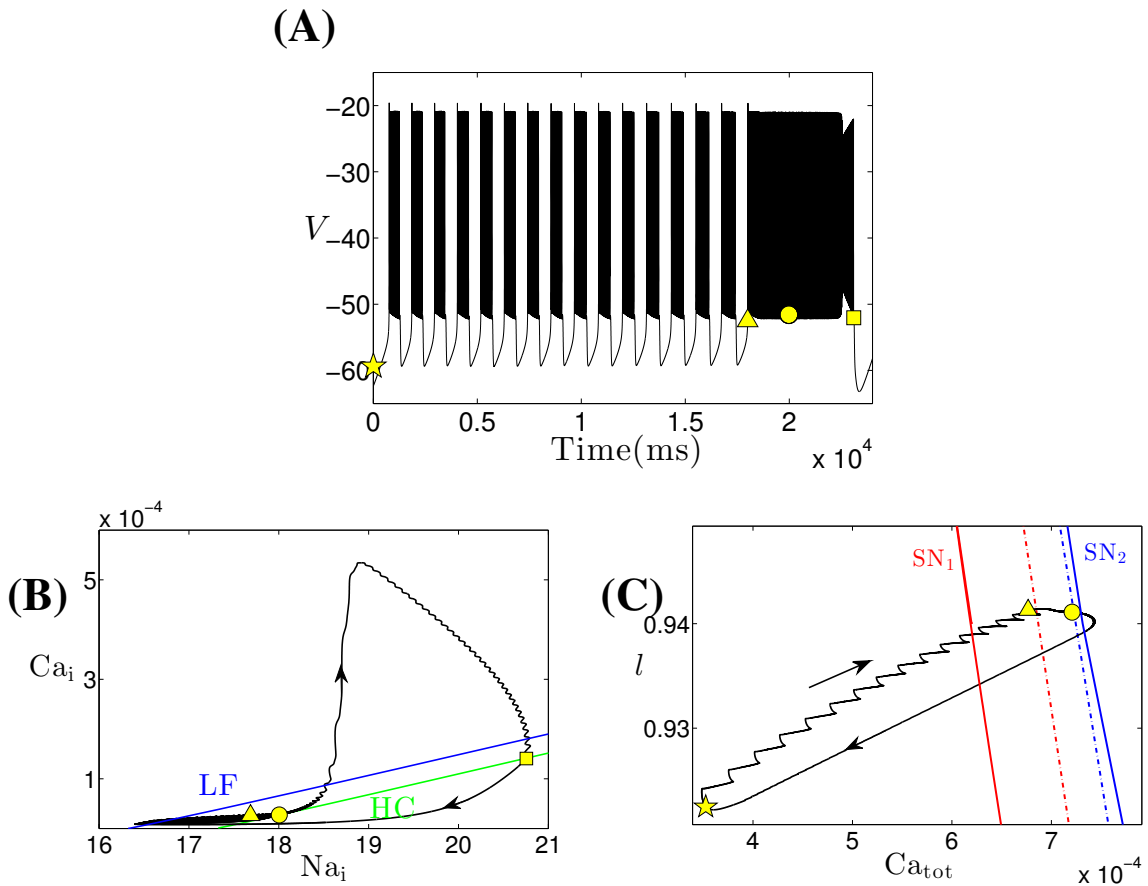


Figure 4.8: Simulation of the SB solution generated by the Jasinski model (4.1), together with the bifurcation diagrams. (A): Temporal evolution of V . (B): Two parameter bifurcation diagrams showing LF (blue) and HC (green) curves together with the trajectory from panel (A) in (Na_i, Ca_i) -space, the enlarged view of the lower left part of which is given by Figure 4.4C. (C): The curves of saddle-node bifurcations corresponding to the upper folds of the bursting branch and the spiking branch in Figure 4.5 (bottom), respectively. We use SN_1 (solid red) to approximate the bursting/spiking boundary (dashed red) and use SN_2 (solid blue) to approximate the onset of jumping up of Ca_i (dashed blue), respectively.

bifurcation structure: periodic orbit amplitudes initiate small at the AH bifurcation and increase as N_{a_i} gets closer to the HC bifurcation (Figure 4.3A). This is qualitatively similar to the bifurcation structure of the somatic subsystem in Chapter 3. Hence following the same argument as discussed in Chapter 3, the amplitude of spikes near the end of the sigh-like burst is increasing.

4.2 IDENTIFYING TIMESCALES

We obtain a non-intuitive result in Chapter 3 that genesis of MB solution does not require a third timescale, a natural question would be: how many timescales are involved in the SB solution? These two solutions appear to be quite similar based on their time courses, yet the underlying mechanisms are different. Moreover, through our analysis on the SB solution in Section 4.1, both slow and superslow variables seem to play important roles in determining generation of regular bursting and the transition to the last long burst. To figure this out, we adopt the approach used in Section 2.3 by transforming our original system into certain two-time-scale systems by adjusting system parameters (see Table 6.1 in Appendix 6.4). Then we consider whether these systems can generate solutions that are similar to SB solution considered in this Chapter. Firstly, we choose $A = 1$ so that l evolves on a comparable timescale as $C_{a_{tot}}$. Since parameters that control the timescale for C_{a_i} will also affect the timescale for $C_{a_{tot}}$, we introduce a new parameter, β , with default value 1, as the scaling factor for right hand side of (4.1f), such that we can increase or decrease β to make C_{a_i} faster or slower. To change the timescale for N_{a_i} , we vary α_{Na} . Originally the Jasinski model has 7 fast, 2 slow, and 2 superslow (7F, 2S, 2SS) variables. As noted before, there are many ways to regroup these timescales to be a two-time-scale system. Here we speed up C_{a_i} and N_{a_i} by increasing both β and α_{Na} by a factor of 100 to produce a system with 9 fast and 2 superslow (9F, 2SS) variables. Another rescaling that we choose to use is slowing the two slow variables by reducing both β and α_{Na} by a factor of 10, respectively, to constitute a (7F, 4SS)-system.

With original scaling, (4.1) generates a SB solution, as shown in Figure 4.2. The modification on the timescale of l does not change this solution qualitatively, except the number of small bursts is less. This is because as l becomes faster, the trajectory projected into $(C_{a_{tot}}, l)$ -space will reach the

spiking/bursting boundary curve (SN_1) earlier and hence small bursts transit to long burst earlier (Figure 4.8C). We first compare the SB solution to solutions from the (9F, 2SS) version of the system (4.1) described above (compare Figure 4.2 with Figure 4.9A). The fast/slow decomposition method (between (V, y) and N_{a_i}, Ca_i) for understanding the mechanisms underlying the regular bursts within the SB solution no longer applies to the (9F, 2SS) case, because Ca_i and N_{a_i} are now evolving fast. In contrast to the original (7F, 2S, 2SS) case where the (7F, 2S)-subsystem generates bursting solutions for relatively small Ca_{tot} and l values (see Figure 4.5 and 4.8C), the new 9-dimensional fast subsystem for (9F, 2SS) case exhibits tonic spiking for all Ca_{tot} and l values within a complete bursting cycle. A graphical summary of the effect of Ca_{tot} on the trajectories is provided in panel (B), where the bifurcation diagram of the fast subsystem (9F) with respect to Ca_{tot} for $l = 0.94$ was computed. The tonic spiking solutions persist for all Ca_{tot} values, while bursting branch that was found in the original system no longer exists in this case. Therefore, the spiking persists throughout the full period, failing to yield a SB solution.

Under the alternative rescaling to a (7F, 4SS) system, the bursting solution is as shown in Figure 4.10A. The square-wave bursting properties have been restored, In fact, the (7F, 2S, 2SS) and (7F, 4SS) systems have the same fast subsystem with all other slow/superslow variables fixed. Similar bifurcation analysis of this fast subsystem as illustrated before can be used to explain the bursting solution in this rescaled system (see Figure 4.10B). Within the projection into the (N_{a_i}, Ca_i) -space, the oscillations begin as the trajectory reaches the LF curve, where it turns around and evolves rightward. Notice that Ca_i and N_{a_i} are now evolving on a superslow timescale, the drift of the trajectory in the direction of increasing Ca_i and N_{a_i} after passing the curve of LF bifurcations is too slow for the solution to reach the curve of HC bifurcations. As a result, bursting continue until the transition to tonic spiking (due to the increase of Ca_{tot} and l) happens. While oscillations continue, all four superslow variables are increasing superslowly and eventually Ca_i jumps up to a relatively larger value, from which Ca_i starts decreasing (Figure 4.10C). Again similarly as before, this reduction in Ca_i is fundamental in terminating the burst as it brings the trajectory across the curve of HC bifurcations. Afterwards, the solution enters the silent phase and goes back to the starting point, completing one cycle of one single long burst. The mechanisms underlying the switch from bursting to tonic spiking and the onset of the jump up of calcium can be understood using a similar averaging method as used in Section 4.1.2 and hence details are omitted here.

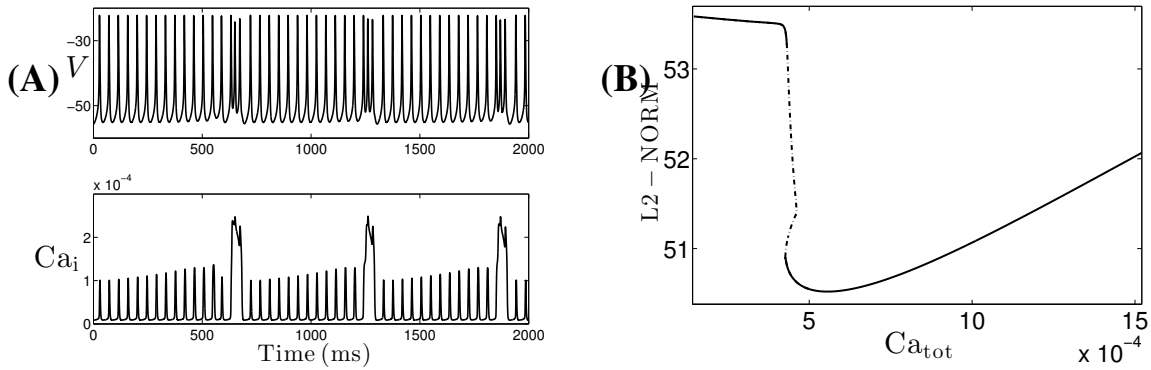


Figure 4.9: Rescaled version of (4.1): (9F, 2SS) case, with $\beta = 100$, $\alpha_{Na} = 5 \times 10^{-3}$. (A): Time series of V and Ca_i . (B): The tonic spiking branch for the 9-dimensional layer problem of the (9F, 2SS) system, with $l = 0.94$. Solid curve denotes stable tonic spiking solutions while dashed denotes unstable. Within the small interval in Ca_{tot} where dashed curve appear, there exists bistability between the upper and lower solid curves.

In summary, neither of these two-time-scale systems captures the full features of the SB solution shown in Figure 4.2. We then conclude that presence of three timescales are necessary for SB solutions, which differs from what we obtain in the Mixed bursting model.

4.3 DISCUSSION

We considered a self-coupled neuron model featuring both I_{CAN} and the Na^+/K^+ -pump current. In contrast to previous models studied in Chapter 2 and 3, the Jasinski model has bidirectional coupling between voltage and calcium. The sigh-like bursts will be eliminated when $\bar{g}_{Ca} = 0$ (i.e., $I_{Ca} = 0$) such that the bidirectional coupling becomes unidirectional as considered in Chapter 2 and 3: the dynamics of voltage affects calcium but not vice versa. Therefore, the consideration of bidirectional coupling in the Jasinski model is particularly important for understanding the dynamics of the SB solution. Such bidirectional coupling also arises in many other model systems and

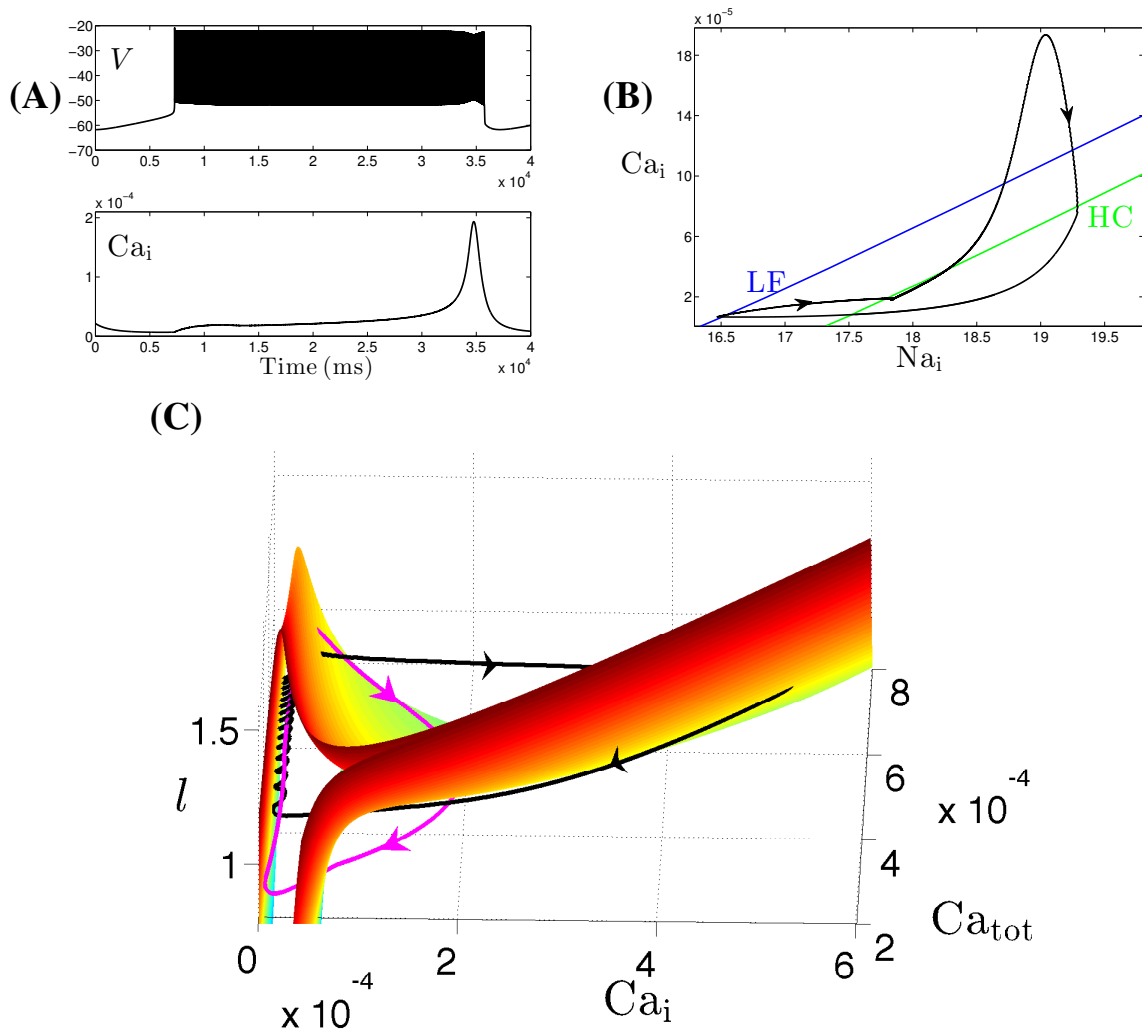


Figure 4.10: Rescaled version of (4.1): (7F, 4SS) case, with $\beta = 0.1$, $\alpha_{Na} = 5 \times 10^{-6}$. (A): Time series of V and Ca_i . (B): The projection of the trajectory from (A) onto the two parameter bifurcation diagram for the 7-dimensional layer problem of the (7F, 4SS) system. (C) Ca_i -nullsurfaces and trajectory (black) are the same as illustrated in Figure 4.3B and C, together with the trajectory (magenta) of the (7F, 4SS) system from (A).

is more biologically relevant. In this Chapter, we have extended and applied methods and analysis from previous chapters to the Jasinski model and explained the mechanisms underlying the SB solution. While the bidirectional coupling between V and Ca_i as well as more detailed Ca^{2+} dynamics make the implementation of the decomposition method more difficult, we applied fast-slow averaging to help explain the mysterious parts which cannot be done using the approach in Chapter 3 for MB solution. Besides describing specific details of SB solution features, we have also investigated whether this solution is truly three timescale phenomena or not. Different from the MB solution, our analysis shows that SB solution features are lost under grouping to two timescales and hence can be said to require at least three timescales.

As in Chapter 3, several conditions for supporting the SB solution can also be implied from our analysis in this Chapter. In order to obtain SB solutions, we require relatively small g_{Ca} since large g_{Ca} will remove SB patterns in the Jasinski model. Notice that the increase of g_{Ca} will speed up Ca_i (see Table 6.1) such that the time allowing for generating small bursts becomes shorter and as a result, the number of small bursts decreases. If we keep increasing g_{Ca} , the small bursts will completely disappear and the SB solution will be lost. This suggests that it is necessary that the V subsystem acts as a square-wave burster for Ca_i values arising during regular bursts, so that there exist small burst solutions before Ca_i jumps up to its active phase. Second, the time before Ca_i jumps up should be long enough to allow for multiple crossings between the LF and HC curves in the (Na_i, Ca_i) -space. As suggested by the (9F, 2SS) case shown in Figure 4.9, each crossing between the LF and HC should be slow enough for the full system to generate bursts instead of tonic spiking solutions. More rigorous analysis on what conditions on the timescales that together support SB solutions will need to be done in the future, which may provide useful information for building minimum model for SB solutions as well as how can we make the solution more robust by tuning the model, as we did Chapter 3.

Another future work is to understand why the self-excitation plays such an essential role that without it, SB solution no longer exists. In our setting, we have chosen $g_{SynE} = 20$ to obtain the SB solutions. Decrease of g_{SynE} will eliminate the SB dynamics, which agrees with the findings from [30] that the SB is an emergent, network interaction-dependent bursting solution. A numerical simulation shows that decrease of g_{SynE} will result in a transition from bursting to spiking in the voltage subsystem. Hence, for g_{SynE} small such that the voltage subsystem is at tonic spiking

regime, which violates the first condition that the voltage subsystem needs to be burst-capable at low calcium. As a result, SB solution is lost via a decrease in the self-coupling strength. Again, more detailed analysis will be done in the near future.

5.0 CONCLUSIONS

5.1 SUMMARY

Several varieties of a novel mixed bursting (MB) solution arise from the interaction of the somatic membrane properties and Ca^{2+} oscillations in pre-BötC neurons [47, 80]. Models that consist of oscillations in both membrane potential and intracellular Ca^{2+} typically involve three or more timescales since each oscillation has at least two timescales. Determining the mathematical mechanisms underlying such complicated solutions can be challenging. To address this issue, in Chapter 2, we constructed a three timescale minimal model by coupling two copies of Morris-Lecar (ML) equations, each representing membrane potential oscillations and calcium dynamics, respectively. We demonstrated that approach previously developed in the context of GSPT for the analysis of two timescale systems extend naturally to the three timescale setting. Our analysis explained the dynamic mechanisms underlying solution features in this three timescale minimum model. By comparison with certain two timescale versions of the same system, we identified some solution properties that truly require three timescales and thus can be viewed as indicators that the presence of three timescales in a system is functionally relevant. The investigation of which solution features are truly three timescale phenomena provides useful information for modeling studies, where a determination needs to be made about how many timescales to include in a model to represent some given experimental data. This finding also suggests that grouping timescales into just two classes should no longer be a default choice in modeling work.

With the GSPT extended to three timescale problems [41], in Chapter 3, we used it to explain the mechanisms underlying the MB solution, produced by a single-compartment model of a pre-BötC inspiratory neuron that can exhibit both I_{NaP} and Ca^{2+} oscillations. In the course of our analysis, rather surprisingly, we discovered that a third timescale is not actually required to gener-

ate MB solutions. In addition to the previous analysis, we have also demonstrated how to obtain more robust MB solution by tuning the full model. Notice that the transitions between regimes of different activity patterns yielded by varying system parameters (e.g. $[IP_3]$, g_{NaP} , g_{CAN}) have been studied in past works [14, 73, 47], in all of which the MB solution only exists in a very small range of parameters. In Chapter 3, we have investigated why the new combination of timescales that we have found can support more robust MB solutions and hence have determined how to obtain a larger MB region in $([IP_3], g_{NaP})$ parameter space by changing timescales. This analysis would also carry over similarly to the robustness analysis of the MB solution with respect to other parameters, such as g_{CAN} , that are known to vary across pre-BötC neurons. Based on this model, we predicted that MB is likely to arise for pre-BötC neurons for which dendritic calcium oscillations contribute significantly to somatic membrane dynamics, such as through activation of a CAN current, over an intermediate range of g_{NaP} values for which the somatic compartment is itself burst-capable at low Ca^{2+} .

As in other earlier work [35], we have considered only one-directional coupling in both Chapter 2 and 3, from the calcium to the membrane potential dynamics, such that our models can be thought of as one oscillator forcing another. In Chapter 4, we considered a more detailed model for neurons in the pre-BötC [30], where each of membrane potential and cytoplasmic Ca^{2+} concentration can influence the evolution of the other. In addition to I_{NaP} and I_{CAN} , the Na^+/K^+ pump also plays an important role in the generation of the SB solution, yet this was not considered in the mixed bursting model from Chapter 3. A heterogeneous population of these neurons can generate SB solution that look similar to MB solutions. To facilitate our analysis, we have only considered the self-coupling case. We generalized the methodology developed in Chapter 2 and Chapter 3 to this more complicated Jasinski model, including additional bursting terminating mechanisms seen in respiratory neurons and synaptic coupling as well. Despite the similarities in voltage dynamics shared with MB solution, SB dynamics is resulting from the presence of three timescales.

5.2 WHEN DO WE NEED THREE TIMESCALES?

One intuitive way to study timescales in data is using Fourier analysis. It comprises three steps: first, we de-trend the input data or signal, by subtracting the linearly fitted data from it; second, apply the discrete Fourier transformation and third, compute the power spectral density from the output. See Figure 5.1 for the frequency-power plot of V in both MB and SB solutions, notice the frequency axis is only shown with the zoom in at left half since the remainder of the points are symmetric. The timescales in the signal can be observed by figuring out its dominant frequencies. From Figure 5.1A, we can notice that the two peaks in the spectral density clearly appear near 1 Hz and 50 Hz for the MB solution, which seems to agree with our conclusion in Chapter 3 that MB is not specifically a three timescale phenomenon. In Figure 5.1B, however, besides the two peaks observed near 0.1 Hz and 5 Hz, a third and much lower peak also emerges between them near 2 Hz. This suggests that there may be 3 scales in the SB solution, consistent with our analysis in Chapter 4 that at least three timescales are involved in the SB solution. While Fourier analysis helps detect certain timescales as illustrated above, we are not able to identify which variable evolves on which timescale, how the timescales should be grouped, or how can we make certain solution more robust as we have done using our methods and analysis in this thesis.

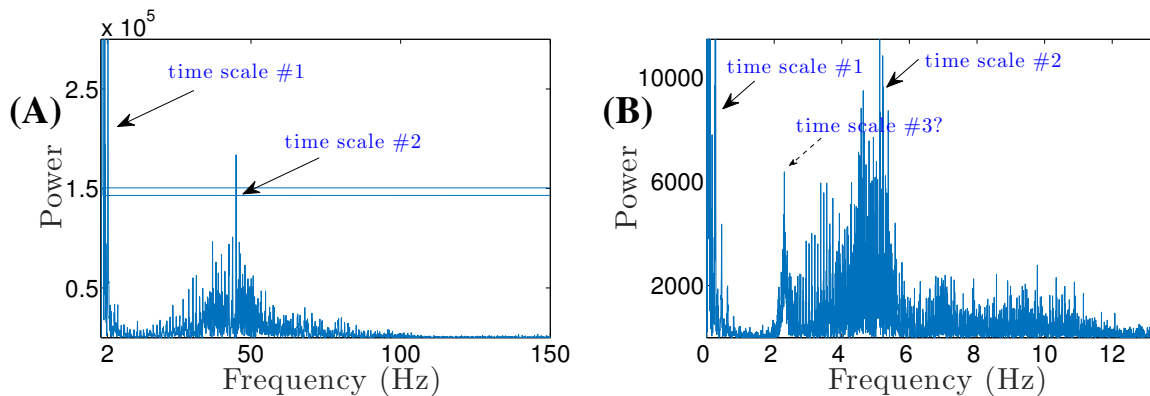


Figure 5.1: Frequency-power plot for V in the MB solution (A) and the SB solution (B).

Three timescale systems have received little attention (discussed in Section 2.4) and are typically treated as two timescale problems, which is the natural setting for GSPT. However, the presence of three timescales means that there are various ways in which the theory can be im-

plemented. One particular implementation ignores the timescale difference between the slow and superslow variables and group them as one class [23, 77]. Alternatively, another viewpoint considers only the superslow variables as the parameters for the subsystem consisting of equations for all others [59, 78]. Through our analysis in the thesis, however, we demonstrated that neither of these two techniques provides a complete view of the oscillating solution dynamics that we discussed. For instance, one of the main characteristics of the SB solution of the Jasinski model is the transition from the regular burst to the long burst, which corresponds to a SN bifurcation of periodic solutions to the fast-slow subsystem with the superslow variables treated as parameters, which emphasizes the importance of having superslow variables in the full system. Similarly, the existence of fast/slow decomposition explains the mechanisms underlying the regular bursts within the SB solution. Hence, without considering the presence of all three timescales, we are not able to fully characterize full features of the SB solution.

5.3 ANALYSIS OF 3 TIMESCALE SYSTEMS

The proposed workflow of studying rhythmic dynamics in multiple timescale system using GSPT is as follows: First, nondimensionalize to find the presence of different timescale; Second, determine how to group timescales (whether to use two or three classes); Third, use GSPT to do timescale separation between classes and derive subsystems; Fourth, explain mechanisms underlying certain dynamics by analyzing lower dimensional subsystems; Fifth, determine which timescale can be recombined without losing qualitative features.

In this thesis, we studied irregular bursting activity produced by models featuring multiple timescale structure. Based on the nondimensionalization results, they generally take the following form

$$(5.1a) \quad \varepsilon_1 \frac{dx}{dt_s} = f(x, y, \varepsilon_1, \varepsilon_2)$$

$$(5.1b) \quad \frac{dy}{dt_s} = g(x, y, z, \varepsilon_1, \varepsilon_2)$$

$$(5.1c) \quad \frac{dz}{dt_s} = \varepsilon_2 h(x, y, z, \varepsilon_1, \varepsilon_2),$$

where $0 < \varepsilon_1, \varepsilon_2 \ll 1$ are small, independent perturbation parameters, $x \in \mathbb{R}^n$ is fast, $y = (y_1, y_2) \in \mathbb{R}^2$ is slow and $z \in \mathbb{R}^2$ is superslow. t_s denotes the slow time.

As discussed in Chapter 2, GSPT can be implemented to yield an array of subsystems as illustrated in Table 2.2, some of which are reproduced in Table 5.1 for convenience. t_f and t_{ss} denote the fast and superslow time, respectively. Notice that the slow reduced system includes two distinct timescales (fast and slow), so we also called it the fast-slow subsystem in Chapter 4.

Table 5.1: Subsystems for 3 timescale system.

equation	system name	frozen variables	domain
$\frac{dx}{dt_f} = f$	fast layer	y, z	\mathbb{R}^{n+4}
$\varepsilon_1 \frac{dx}{dt_s} = f$ $\frac{dy}{dt_s} = g$	slow layer	z	\mathbb{R}^{n+4}
$\frac{dy}{dt_s} = g$	slow reduced layer	z	$\mathcal{M}_s := \{(x, y, z) : f = 0\}$
$\frac{dz}{dt_{ss}} = h$	superslow reduced	none	$\mathcal{M}_{ss} := \{(x, y, z) : f = g = 0\} \subset \mathcal{M}_s$

We elucidated the mechanisms underlying the multiple timescale dynamics from the perspective based on the ideas of fast-slow decomposition, in which we consider the interaction of two potentially oscillating or bursting systems. For example, in Chapter 2 (resp., 3), we considered how one potentially oscillating (resp., bursting) subsystem is driven by another intrinsically oscillating subsystem. In Chapter 4, bidirectional coupling between oscillating and bursting subsystems has also been investigated.

Our analysis starts with a bifurcation analysis of the fast layer problem. Changes in superslow variables z affect x indirectly, through the coupling between y and z and the coupling of y to x , but not directly. Thus, if we treat all frozen variables in the fast layer problem as bifurcation parameters, it is sufficient to consider only $y = \{y_1, y_2\}$. With these two parameters, we treat y_1 as a bifurcation parameter for the geometric analysis of the (x, y_1) subsystem and to consider the effect of y_2 on the resulting bifurcation diagram, as illustrated in Figure 2.12, 3.5B and 4.4A. To do this, we computed 2-parameter bifurcation diagrams for the fast layer problem in (y_1, y_2) -space, as illustrated in Figure 2.13, 3.5D, 4.4C. A detailed geometric analysis of this two parameter

bifurcation structures revealed the mathematical mechanism of solutions to our problem as the two slow variables traverse (y_1, y_2) -space: e.g., we used the two parameter bifurcation structures to understand the mechanisms underlying the regular bursts within both MB and SB solutions in Chapter 3 and 4, respectively.

Notice that the superslow variable hasn't come into play, the presence of which determines on which timescale (slow or superslow) y_2 evolves. Understanding this is crucial in explaining how the transition from the regular burst to the long burst within MB and SB solutions happens. The mechanism underlying the jump up of y_2 in Chapter 3 is easy to understand, since (y_2, z) subsystem (i.e. the (c, l) subsystem) acts as a relaxation oscillator and hence the jumps occur at a saddle-node bifurcation of this subsystem. However, in the Jasiniski model, instead of slaving to z and evolving on a superslow timescale during the silent phase, y_1 exhibits slow drift throughout the spiking phase of each burst. Hence, we used slow averaged nullcline method, a numerical technique commonly used in two timescale context when solutions combine fast oscillations and slow drift [2, 6]. Implementation of the averaging method enabled us to detect the bifurcation corresponding to the transition from the regular burst to the long burst. Combining with the bifurcation analysis of the fast layer problem, our methods provided us a full explanation of the SB solution dynamics.

While our study is motivated by the bursting patterns observed in the pre-BötC, it may as well be applicable to other brain areas exhibiting rhythmic activity. In other mammalian CPGs and rhythmic neural circuits, the NaP current and CAN current have been identified as playing critical roles in pattern generation [79, 68, 82, 69, 83, 64, 5, 75]. Given that NaP and CAN currents are widespread and can be essential for the generation of bursts [56, 14, 73, 47, 30], it seems likely that the interaction of these currents is a fundamental component of the genesis of bursting solutions in other areas as well. Therefore, it is likely that our analysis of MB or SB patterns can be extended and applied to these other rhythmic neuronal systems, both to explain the underlying dynamics and to assess its timescale requirements.

6.0 APPENDIX

6.1 NONDIMENSIONALIZATION OF THE COUPLED MORRIS-LECAR SYSTEM

Here we present details of the nondimensionalization of (2.1). From numerical simulations of this system, we find that the membrane potential for the uncoupled ML oscillators typically lies between -70 mV and 60 mV. Correspondingly, we define $T_w = \max(1/\tau_w(V_i))$ over the range $V_i \in [-70, 60]$ and then define $t_w(V_i)$, a rescaled version of $\tau_w(V_i)$, by $t_w(V_i) = T_w \tau_w(V_i)$. We also define g_{\max} to be the maximum of the three conductances g_{Ca} , g_K , and g_L . Substituting these expressions into (2.1a-2.1d) and rearranging, we obtain the following dimensionless system:

$$(6.1a) \quad \frac{C_1}{Q_t \cdot g_{\max}} \frac{dv_1}{d\tau} = \bar{I}_1 - \bar{g}_{Ca} m_\infty(v_1)(v_1 - \bar{V}_{Ca}) - \bar{g}_K w_1(v_1 - \bar{V}_K) \\ - \bar{g}_L(v_1 - \bar{V}_L) - \bar{g}_{syn} S(v_2)(v_1 - \bar{V}_{syn})$$

$$(6.1b) \quad \frac{1}{\phi_1 Q_t T_{w_1}} \frac{dw_1}{d\tau} = \frac{1}{t_w(v_1)} (w_\infty(v_1) - w_1)$$

$$(6.1c) \quad \frac{C_2}{Q_t \cdot g_{\max}} \frac{dv_2}{d\tau} = \bar{I}_2 - \bar{g}_{Ca} m_\infty(v_2)(v_2 - \bar{V}_{Ca}) - \bar{g}_K w_2(v_2 - \bar{V}_K) \\ - \bar{g}_L(v_2 - \bar{V}_L)$$

$$(6.1d) \quad \frac{1}{\phi_2 Q_t T_{w_2}} \frac{dw_2}{d\tau} = \frac{1}{t_w(v_2)} (w_\infty(v_2) - w_2),$$

with dimensionless parameters $\bar{I}_x = I_x/(Q_v \cdot g_{\max})$, $\bar{g}_x = g_x/g_{\max}$, and $\bar{V}_x = V_x/Q_v$.

Since we expect $V_i \in [-70, 60]$, a suitable choice for the voltage scale is $Q_V = 100$ mV. We also see that values of $m_\infty(V_i)$, $w_\infty(V_i)$ and w_i all lie in the range $[0, 1]$. For the choice of parameters specified in Table 2.1, the maximum conductance is g_K , so we have $g_{\max} = g_K$. Numerical evaluation of $1/\tau_w(V_i)$ for $V_i \in [-70, 60]$ shows that $T_w \approx 5.3 \text{ ms}^{-1} = O(10) \text{ ms}^{-1}$. Using these values we see that all terms in the right hand sides of (6.1a)–(6.1d) are bounded (in absolute value) by one.

The coefficients of the derivatives in the left hand sides of (6.1a)–(6.1d) now reveal the relative rates of evolution of the variables. We find that $C_1/g_{\max} = O(1) \text{ ms}^{-1}$, $1/(\phi_1 T_w) \approx C_2/g_{\max} = O(10) \text{ ms}^{-1}$ and $1/(\phi_2 T_w) = O(100) \text{ ms}^{-1}$, from which we conclude that v_1 evolves on a fast timescale, w_1 and v_2 evolve on a slow timescale, and w_2 evolves on a superslow timescale. We choose the slow timescale as our reference time, i.e., pick $Q_t = 10 \text{ ms}$, and set

$$(6.2a) \quad \varepsilon_1 := \frac{C_1}{Q_t \cdot g_{\max}} \ll 1, \quad \varepsilon_2 := \phi_2 Q_t T_w \ll 1,$$

$$(6.2b) \quad R_{w_1} := \phi_1 Q_t T_w, \quad R_{v_2} := \frac{Q_t \cdot g_{\max}}{C_2}.$$

As a result, the dimensionless system (6.1) becomes the system (2.4) given in Section 3.1.1, namely

$$(6.3a) \quad \varepsilon_1 \frac{dv_1}{d\tau} = \bar{I}_1 - \bar{g}_{\text{Ca}} m_\infty(v_1)(v_1 - \bar{V}_{\text{Ca}}) - \bar{g}_{\text{K}} w_1(v_1 - \bar{V}_{\text{K}}) - \bar{g}_{\text{L}}(v_1 - \bar{V}_{\text{L}}) - \bar{g}_{\text{syn}} S(v_2)(v_1 - \bar{V}_{\text{syn}}) := f_1(v_1, v_2, w_1)$$

$$(6.3b) \quad \frac{dw_1}{d\tau} = R_{w_1} \frac{1}{t_w(v_1)} (w_\infty(v_1) - w_1) := g_1(v_1, w_1)$$

$$(6.3c) \quad \frac{dv_2}{d\tau} = R_{v_2} (\bar{I}_2 - \bar{g}_{\text{Ca}} m_\infty(v_2)(v_2 - \bar{V}_{\text{Ca}}) - \bar{g}_{\text{K}} w_2(v_2 - \bar{V}_{\text{K}}) - \bar{g}_{\text{L}}(v_2 - \bar{V}_{\text{L}})) := f_2(v_2, w_2)$$

$$(6.3d) \quad \frac{dw_2}{d\tau} = \varepsilon_2 \frac{1}{t_w(v_2)} (w_\infty(v_2) - w_2) := \varepsilon_2 g_2(v_2, w_2),$$

with small parameters ε_1 and ε_2 , where R_{w_1} and R_{v_2} are dimensionless parameters bounded by one.

6.2 ADJUSTING TIMESCALES IN THE DENDRITIC SUBSYSTEM

The full model (3.1) is capable of generating an MB solution (Figure 6.1A) with original parameter values as given in Table 3.1. From the phase plane for the dendritic subsystem as shown in Figure 3.1B, we find that $([\text{Ca}], l)$ acts as a relaxation oscillator. However, since the l -nullcline lies extremely close to the left knee of $[\text{Ca}]$ -nullcline (Figure 6.1A), the trajectory projected to $([\text{Ca}], l)$ -space does not jump up to large $[\text{Ca}]$ values and transition to the long burst (LB) phase immediately after passing the left knee (yellow circle). Instead, it slowly moves along the l -nullcline

for a transient period before jumping up to the right branch (Figure 6.1B and C: from the yellow circle to the green circle); this effect can be interpreted as the influence of the bifurcation in the dendritic subsystem initiating the (c, l) oscillation that occurs at a value of $[IP_3]$ just below 0.95 [47]. Numerically, we observe that small bursts occur during this period (Figure 6.1A). Therefore, the existence of such MB solution relies heavily on the nullcline interactions, which can be tuned by changing $[IP_3]$. To clarify the identification of the timescales involved in the MB behavior and the assessment of how to group timescales, and to eliminate the sensitivity of MB solutions to the precise value of $[IP_3]$, we increase $[IP_3]$ to be 1. As a result, the $[Ca]$ -nullcline moves downward and hence further from the l -nullcline. Furthermore, we also slow down l by decreasing A from 0.005 to 0.001 so that $l \sim O(1000)$ ms becomes more separated from $[Ca]$, the delay time of the jump up of $[Ca]$ at the left knee is significantly decreased, and the dendritic subsystem takes on a stronger relaxation character.

Remark 5. *Although the dendritic subsystem acts as a more standard relaxation oscillator with new parameter values ($[IP_3] = 1$, $A = 0.001$), $[IP_3]$ is not far enough from the bifurcation value for the influence of the bifurcation mentioned above to completely vanish. Hence, there is still a transient delay before $[Ca]$ jumps up at the left knee, but it is much shorter than that with original parameter values.*

6.3 NONDIMENSIONALIZATION OF THE MIXED BURSTING MODEL

From numerical simulations, we find that the membrane potential V typically lies between -60 mV and 20 mV. Correspondingly, for $x \in \{n, h\}$, we define $T_x = \max(1/\tau_x(V))$ over the range $V \in [-60, 20]$ and then define $t_x(V)$, a rescaled version of $\tau_x(V)$, by $t_x(V) = T_x \tau_x(V)$. We also define g_{\max} to be the maximum of the five conductances g_L , g_K , g_{Na} , g_{NaP} and g_{CAN} . Furthermore, we let $G([Ca]) = \frac{[IP_3][Ca]}{([IP_3]+K_I)([Ca]+K_a)}$ and $g_{SERCA}([Ca]) = V_{SERCA} \frac{[Ca]}{K_{SERCA}^2 + [Ca]^2}$. Substituting these expressions into equations (3.1) and rearranging, we obtain the following system:

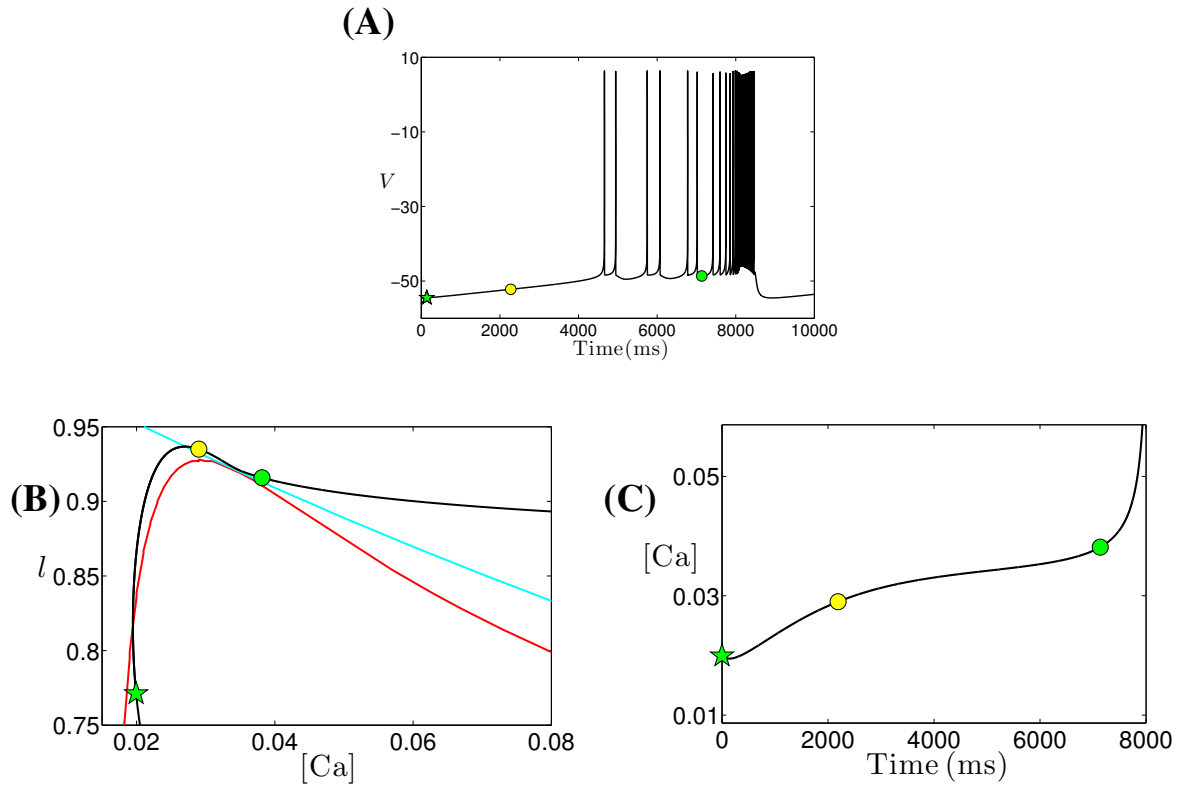


Figure 6.1: Time series for attracting solutions of the full model (3.1) as well as the bifurcation structure of the dendritic subsystem with parameter values as in Table 3.1. Green and yellow symbols mark key points along the solution trajectory (green star: the point with minimum $g_{CAN_{Tot}}$; yellow circle: the point when the trajectory passes the left knee of the $[Ca]$ -nullcline; green circle: beginning of the long burst (LB).) (A): Time series for V . (B): Enlarged view of part of Figure 3.1B showing the nullclines for $[Ca]$ (red) and l (cyan) for the dendritic subsystem, together with the MB solution from the upper row. (C): Part of time series of $[Ca]$.

$$(6.4a) \quad \frac{C_m}{Q_t \cdot g_{\max}} \frac{dv}{d\tau} = -\bar{g}_L(v - \bar{V}_L) - \bar{g}_K n^4(v - \bar{V}_K) - \bar{g}_{Na} m_\infty^3(v)(1-n)(v - \bar{V}_{Na}) \\ - \bar{g}_{NaP} m p_\infty(v) h(v - \bar{V}_{Na}) - \bar{g}_{CAN} f(c)(v - \bar{V}_{Na})$$

$$(6.4b) \quad \frac{1}{Q_t \cdot T_n} \frac{dn}{d\tau} = (n_\infty(v) - n)/t_n(v)$$

$$(6.4c) \quad \frac{1}{Q_t \cdot T_h} \frac{dh}{d\tau} = (h_\infty(v) - h)/t_h(v)$$

$$(6.4d) \quad \frac{d[Ca]}{d\tau} = K_{Ca} \cdot (L_{IP_3} + P_{IP_3} G^3([Ca]) l^3) \left(\frac{[Ca]_{\text{Tot}} - [Ca]}{\sigma} - [Ca] \right) \\ - K_{Ca} \cdot g_{SERCA}([Ca]) \cdot [Ca]$$

$$(6.4e) \quad \frac{dl}{d\tau} = AK_d(1-l) - A[Ca]l$$

with dimensionless parameters $\bar{g}_x = g_x/g_{\max}$ and $\bar{V}_x = V_x/Q_v$. Note that we have now nondimensionalized the somatic subsystem (3.1a)-(3.1c).

Next we deal with equations (3.1d)-(3.1e) by nondimensionalizing $[Ca]$, which typically lies between $0 \mu\text{M}$ and $1 \mu\text{M}$, based on numerical simulations. We define $G_c = \max(G^3([Ca]))$ and $G_S = \max(g_{SERCA}(Ca))$ over the range $[Ca] \in [0, 1]$ and then define P_{\max} to be the maximum of $\{L_{IP_3}, P_{IP_3} G_c, G_S\}$. From system (6.4), we get the following dimensionless system:

$$(6.5a) \quad \frac{C_m}{Q_t \cdot g_{\max}} \frac{dv}{d\tau} = -\bar{g}_L(v - \bar{V}_L) - \bar{g}_K n^4(v - \bar{V}_K) - \bar{g}_{Na} m_\infty^3(v)(1-n)(v - \bar{V}_{Na}) \\ - \bar{g}_{NaP} m p_\infty(v) h(v - \bar{V}_{Na}) - \bar{g}_{CAN} f(c)(v - \bar{V}_{Na})$$

$$(6.5b) \quad \frac{1}{Q_t \cdot T_n} \frac{dn}{d\tau} = (n_\infty(v) - n)/t_n(v)$$

$$(6.5c) \quad \frac{1}{Q_t \cdot T_h} \frac{dh}{d\tau} = (h_\infty(v) - h)/t_h(v)$$

$$(6.5d) \quad \frac{\sigma}{Q_t \cdot P_{\max} \cdot K_{Ca}} \frac{dc}{d\tau} = (\bar{L}_{IP_3} + \bar{P}_{IP_3} G^3(c) l^3) ([\bar{Ca}]_{\text{Tot}} - c - \sigma \cdot c) - \bar{g}_{SERCA}(c) \cdot c$$

$$(6.5e) \quad \frac{1}{Q_t \cdot Q_c \cdot A} \frac{dl}{d\tau} = \bar{K}_d(1-l) - cl$$

with dimensionless parameters $\bar{L}_{IP_3} = L_{IP_3}/P_{\max}$, $\bar{P}_{IP_3}(c) = P_{IP_3}/P_{\max}$, $\bar{K}_d = K_d/Q_c$ and $\bar{g}_{SERCA}(c) = g_{SERCA}([Ca])/P_{\max}$.

Since we expect $V \in [-60, 20]$ and $[Ca] \in [0, 1]$, suitable choices for the voltage and calcium scales are $Q_v = 100 \text{ mV}$ and $Q_c = 1 \mu\text{M}$, respectively. We also see that values of $m_\infty(V)$, $m p_\infty(V)$, $f([Ca])$, $n_\infty(V)$, $h_\infty(V)$, $G([Ca])$, $\bar{g}_{SERCA}([Ca])$, n , h and l all lie in the range $[0, 1]$.

For the choice of parameters specified in Table 3.1, the maximum conductance is $g_{\text{Na}} = 28 \text{ nS}$, so we have $g_{\text{max}} = g_{\text{Na}}$. Numerical evaluations of $1/\tau_n(V)$ and $1/\tau_h(V)$ for $V \in [-60, 20]$ show that $T_n \approx 20 \text{ ms}^{-1}$ and $T_h \approx 0.04 \text{ ms}^{-1}$. Similarly, we obtain $G_c \approx 0.0421$ and $G_S \approx 1000 \text{ pL} \cdot \text{ms}^{-1}$, so we have $P_{\text{max}} \approx 1305 \text{ pL} \cdot \text{ms}^{-1}$. Using these values we see that all terms in the right hand sides of equations (6.5a)-(6.5e) are bounded (in absolute value) by one.

The coefficients of the derivatives in the left hand sides of equations (6.5a) - (6.5e) now reveal the relative rates of evolution of the variables. We find that $C_m/g_{\text{max}} = 0.75 \text{ ms} \sim \text{O}(1) \text{ ms}$, $1/T_n = 0.05 \text{ ms} \sim \text{O}(0.1) \text{ ms}$, $1/T_h = 25 \text{ ms} \sim \text{O}(10) \text{ ms}$, $\frac{\sigma}{P_{\text{max}} \cdot K_{Ca}} = 5.67 \text{ ms} \sim \text{O}(10) \text{ ms}$ and $\frac{1}{Q_c \cdot A} = 200 \text{ ms} \sim \text{O}(100) \text{ ms}$. We choose the fast timescale as our reference time, i.e., pick $Q_t = 1 \text{ ms}$, and set

$$(6.6a) \quad R_v := \frac{C_m}{Q_t \cdot g_{\text{max}}}, \quad R_x := \frac{1}{Q_t \cdot T_x}, \quad x \in \{n, h\},$$

$$(6.6b) \quad R_c := \frac{\sigma}{Q_t \cdot P_{\text{max}} \cdot K_{Ca}}, \quad R_l := \frac{1}{Q_t \cdot Q_c \cdot A}.$$

As a result, the dimensionless system (6.5) becomes the system (3.4) given in Section 3.1, namely

$$(6.7a) \quad R_v \frac{dv}{d\tau} = -\bar{g}_L(v - \bar{V}_L) - \bar{g}_K n^4(v - \bar{V}_K) - \bar{g}_{\text{Na}} m_\infty^3(v)(1 - n)(v - \bar{V}_{\text{Na}}) \\ - \bar{g}_{\text{NaP}} m p_\infty(v) h(v - \bar{V}_{\text{Na}}) - \bar{g}_{\text{CAN}} f(c)(v - \bar{V}_{\text{Na}}) := f_1(v, n, h, c)$$

$$(6.7b) \quad R_n \frac{dn}{d\tau} = (n_\infty(v) - n)/t_n(v) := g_1(v, n)/t_n(v)$$

$$(6.7c) \quad R_h \frac{dh}{d\tau} = (h_\infty(v) - h)/t_h(v) := h_1(v, h)/t_h(v)$$

$$(6.7d) \quad R_c \frac{dc}{d\tau} = (\bar{L}_{\text{IP}_3} + \bar{P}_{\text{IP}_3} G^3(c) l^3)([\bar{C}a]_{\text{Tot}} - c - \sigma \cdot c) - \bar{g}_{\text{SERCA}}(c) \cdot c := f_2(c, l)$$

$$(6.7e) \quad R_l \frac{dl}{d\tau} = \bar{K}_d(1 - l) - cl := g_2(c, l)$$

where R_v, R_n, R_h, R_c and R_l are dimensionless parameters given in (6.6).

6.4 NONDIMENSIONALIZATION OF THE JASINSKI MODEL

To rescale the variables so that the important timescales can be explicitly identified, we define typical voltage, calcium, sodium and timescales Q_v , Q_c , Q_{na} , and Q_t , respectively, such that

$$V = Q_v \cdot v, \text{Ca}_i = Q_c \cdot ca_i, \text{Ca}_{\text{tot}} = Q_c \cdot c_{\text{tot}}, \text{Na}_i = Q_{na} \cdot na_i, t = Q_t \cdot \tau.$$

Numerical simulations (Figure 4.2) show that the membrane potential V lies between -60 mV and 20 mV. Similarly as in Section 6.3, T_y is defined to be $\max(1/\tau_y(V))$ over the range $V \in [-60, 20]$. and hence we obtain $T_{m_{\text{Na}}} \approx 190.64 \text{ ms}^{-1}$, $T_{h_{\text{Na}}} \approx 55 \text{ ms}^{-1}$, $T_{m_{\text{Ca}}} \approx 2 \text{ ms}^{-1}$, $T_{h_{\text{Ca}}} \approx 0.056 \text{ ms}^{-1}$, $T_{m_{\text{K}}} \approx 0.67 \text{ ms}^{-1}$ and $T_s \approx 0.2 \text{ ms}^{-1}$, respectively. g_{max} , the maximum of all conductances, is 160 nS. Substituting these expressions into system (4.1) and rearranging, we obtain the dimensionless version of the 11-dimensional neuron model:

$$(6.8a) \quad \frac{C}{Q_t \cdot g_{\text{max}}} \frac{dv}{dt} = -\bar{I}_{\text{Na}} - \bar{I}_{\text{NaP}} - \bar{I}_{\text{K}} - \bar{I}_{\text{Ca}} - \bar{I}_{\text{CAN}} - \bar{I}_{\text{Pump}} - \bar{I}_{\text{L}} - \bar{I}_{\text{SynE}}$$

$$(6.8b) \quad \frac{1}{Q_t \cdot T_y} \frac{dy}{d\tau} = (y_{\infty}(v) - y)/t_y(v),$$

$$(6.8c) \quad \frac{Q_c}{Q_t \cdot \alpha_{\text{Ca}} \cdot g_{\text{Ca}} \cdot Q_v} \frac{dc_{\text{tot}}}{d\tau} = -\frac{I_{\text{Ca}}}{g_{\text{Ca}} \cdot Q_v} - \frac{ca_i}{K_{c_{\text{tot}}}}$$

$$(6.8d) \quad \frac{Q_c}{Q_t \cdot \alpha_{\text{Ca}} \cdot g_{\text{Ca}} \cdot Q_v} \frac{dca_i}{d\tau} = -\frac{I_{\text{Ca}}}{g_{\text{Ca}} \cdot Q_v} - \frac{ca_i}{K_{c_{\text{tot}}}} + K_c \cdot (\bar{J}_{\text{ERIN}} - \bar{J}_{\text{EROUT}})$$

$$(6.8e) \quad \frac{1}{Q_t \cdot Q_c \cdot A} \frac{dl}{dt} = \bar{K}_d(1 - l) - ca_i \cdot l$$

$$(6.8f) \quad \frac{Q_{na}}{Q_t \cdot \alpha_{\text{Na}} \cdot g_{\text{max}} \cdot Q_v} \frac{dna_i}{d\tau} = -(\bar{I}_{\text{Na}} + \bar{I}_{\text{NaP}} + \bar{I}_{\text{CAN}} + 3\bar{I}_{\text{pump}})$$

$$(6.8g) \quad \frac{1}{Q_t \cdot T_s} \frac{ds}{dt} = ((1 - s) \cdot s_{\infty}(V) - s)/t_s(V)$$

where $y = \{m_{\text{Na}}, h_{\text{Na}}, m_{\text{Ca}}, h_{\text{Ca}}, m_{\text{K}}\}$.

Dimensionless currents \bar{I}_x appearing in (6.8a) and (6.8f) are given by $\frac{I_x}{g_{\text{max}} \cdot Q_v}$ and dimensionless calcium fluxes are $\bar{J}_{\text{ERIN}} = J_{\text{ERIN}} \cdot \sigma / P_{\text{max}}$ and $\bar{J}_{\text{EROUT}} = J_{\text{EROUT}} \cdot \sigma / P_{\text{max}}$, where P_{max} , as defined in Section 6.3, takes the value 1148 according to numerical results. In equations (6.8c) and (6.8d), $K_{c_{\text{tot}}} = \tau_{\text{Ca}} \cdot \alpha_{\text{Ca}} \cdot g_{\text{Ca}} \cdot Q_v / Q_c$ and $K_c = \frac{K_{\text{Ca}} \cdot P_{\text{max}}}{\alpha_{\text{Ca}} \cdot \sigma \cdot g_{\text{Ca}} \cdot Q_v}$.

Since we expect $V \in [-60, 20]$, a suitable choice for the voltage scale is $Q_v = 100$ mV. Similarly, we choose $Q_{na} = 30$ mM since $N_{a_i} \in [16, 21]$. Q_c , the scale for C_{a_i} and $C_{a_{tot}}$, should be determined by magnitudes of both variables. Numerical simulations show that the magnitude of C_{a_i} varies from $O(10^{-5})$ to $O(10^{-3})$ as C_{a_i} jumps up to larger C_{a_i} values, while $C_{a_{tot}}$ is roughly $O(10^{-3})$ (Figure 4.3B and C). Therefore, we choose $Q_c = 10^{-3}$ mM. Using these scales, we see that all terms in the right hand sides of equations (6.8) are bounded (in absolute value) by one except the last term in (6.8d) is roughly $O(10)$. To resolve this issue, we divide both sides of (6.8d) by 10 and obtain the following:

$$(6.9a) \quad \frac{Q_c}{10 \cdot Q_t \cdot \alpha_{Ca} \cdot g_{Ca} \cdot Q_v} \frac{dc_{a_i}}{d\tau} = -\frac{I_{Ca}}{10 \cdot g_{Ca} \cdot Q_v} - \frac{ca_i}{10 \cdot K_{ctot}} + (\bar{J}_{ERIN} - \bar{J}_{EROUT})$$

the right hand side of which is now $O(1)$, as required by nondimensionalization.

The coefficients of the derivatives in the left hand sides of equations (6.8) with (6.8d) replaced by (6.9a) now reveal the relative speeds of evolution of the variables. We find that

Table 6.1: The timescales for the Jasinski model.

variable	coefficient of the derivative	
V	C/g_{\max}	≈ 0.225 ms
m_{Na}	$\frac{1}{T_y}$	≈ 0.0053 ms
h_{Na}		≈ 0.0182 ms
m_{Ca}		≈ 0.5 ms
h_{Ca}		≈ 18 ms
m_K		≈ 1.4925 ms
s		≈ 5 ms
C_{a_i}		$Q_c/(10 \cdot \alpha_{Ca} \cdot g_{Ca} \cdot Q_v)$
N_{a_i}	$Q_{na}/(\alpha_{Na} \cdot g_{\max} \cdot Q_v)$	≈ 37.5 ms
$C_{a_{tot}}$	$Q_c/(\alpha_{Ca} \cdot g_{Ca} \cdot Q_v)$	≈ 615.3846 ms
l	$1/(Q_c \cdot A)$	≈ 10000 ms

Comparing the values of these coefficients indicates how fast each corresponding variable is; the larger the value, the slower the corresponding variable. According to our nondimensionalization results summarized in Table 6.1, we choose to group V , gating variables and s and conclude they evolve on a fast timescale, (C_{a_i}, N_{a_i}) evolve on a slow timescale, and $(C_{a_{tot}}, l)$ evolve on a superslow timescale.

BIBLIOGRAPHY

- [1] G. F. Alheid, W. K. Milsom, and D. R. McCrimmon. Pontine influences on breathing: an overview. *Respir. Physiol. Neurobiol.*, 143(2):105–114, 2004.
- [2] J. Best, A. Borisyuk, J. Rubin, D. Terman, and M. Wechselberger. The dynamic range of bursting in a model respiratory pacemaker network. *SIAM J. Appl. Dyn. Syst.*, 4:1107–1139, 2005.
- [3] C. Beurrier, P. Congar, B. Bioulac, and C. Hammond. Subthalamic nucleus neurons switch from single-spike activity to burst-firing mode. *J. Neurosci.*, 19(2):599–609, 1999.
- [4] A. Bose, Y. Manor, and F. Nadim. Bistable oscillations arising from synaptic depression. *SIAM J. Appl. Math.*, 62(2):706–727, 2001.
- [5] F. Brocard, N. Shevtsova, M. Bouhadfane, S. Tazerart, U. Heinemann, I. Rybak, and L. Vinay. Activity-dependent changes in extracellular Ca^{2+} and K^{+} reveal pacemakers in the spinal locomotor-related network. *Neuron*, 77(6):1047–1054, 2013.
- [6] R.J. Butera, J.W. Clark, and J.H. Byrne. Transient responses of a modeled bursting neuron: analysis with equilibrium and averaged nullclines. *Biol. Cybern.*, 77:307–322, 1997.
- [7] R.J. Butera, J. Rinzel, and J.C. Smith. Models of respiratory rhythm generation in the pre-Bötzinger complex. i. bursting pacemaker neurons. *J. Neurophysiol.*, 82:382–397, 1999.
- [8] R.J. Butera, J. Rinzel, and J.C. Smith. Models of respiratory rhythm generation in the pre-Bötzinger complex. ii. populations of coupled pacemaker neurons. *J. Neurophysiol.*, 80:398–415, 1999.
- [9] F. Clément and J. Françoise. Mathematical modeling of the gnRH pulse and surge generator. *SIAM J. Appl. Dyn. Syst.*, 6(2):441–456, 2007.
- [10] S. Coombes and P.C. Bressloff. Bursting: the genesis of rhythm in the nervous system.
- [11] K. Cowley and B. Schmidt. Effects of inhibitory amino acid antagonists on reciprocal inhibitory interactions during rhythmic motor activity in the in vitro neonatal rat spinal cord. *J. Neurophysiol.*, 74(3):1109–1117, 1995.

- [12] S. Daun, J. Rubin, and I. Rybak. Control of oscillation periods and phase durations in half-center central pattern generators: a comparative mechanistic analysis. *J. Comp. Neurosci.*, 27:3–36, 2009.
- [13] M. Desroches, J. Guckenheimer, B. Krauskopf, C. Kuehn, H.M. Osinga, and M. Wechselberger. Mixed-mode oscillations with multiple time scales. *SIAM Review*, 54:211–288, 2012.
- [14] J. Dunmyre, C. Del Negro, and J. Rubin. Interactions of persistent sodium and calcium-activated nonspecific cationic currents yield dynamically distinct bursting regimes in a model of respiratory neurons. volume 31(2), pages 305–328. 2011.
- [15] B. Ermentrout and D. Terman. *Mathematical Foundations of Neuroscience*. Springer, 2010.
- [16] J. Feldman and C. Del Negro. Looking for inspiration: new perspectives on respiratory rhythm. *Nature Reviews Neuroscience*, 7(3):232–241, 2006.
- [17] J. Feldman and J. Smith. Cellular mechanisms underlying modulation of breathing pattern in mammals. *Ann. NY Acad. Sci.*, 563:114–130, 1989.
- [18] N. Fenichel. Persistence and smoothness of invariant manifolds for flows. *Indiana Univ. Math. J.*, 21:193–225, 1971.
- [19] N. Fenichel. Geometric singular perturbation theory for ordinary differential equations. volume 31, pages 53–98. 1979.
- [20] H. Forster, J. Bonis, K. Krause, J. Wenninger, S. Neumueller, M. Hodges, and L. Pan. Contributions of the pre-Bötzing complex and the Kölliker-Fuse nuclei to respiratory rhythm and pattern generation in awake and sleeping goats. *Progress in Brain Research*, 209:73–89, 2014.
- [21] A. Franci, G. Drion, and R. Sepulchre. Modeling the modulation of neuronal bursting: A singularity theory approach. *SIAM J. Appl. Dyn. Syst.*, 13(2):798–829, 2014.
- [22] H. Koizumi H and J.C. Smith. Persistent Na⁺ and K⁺-dominated leak currents contribute to respiratory rhythm generation in the pre-Botzinger complex in vitro. *J. Neurosci.*, 28:1773–1785, 2008.
- [23] J. Ha and A. Kuznetsov. Frequency switching in a two-compartmental model of the dopaminergic neuron. *J. Comp. Neurosci.*, 30:241–254, 2011.
- [24] E. Harvey, V. Kirk, H.M. Osinga, J. Sneyd, and M. Wechselberger. Understanding anomalous delays in a model of intracellular calcium dynamics. *Chaos*, 20:045104, 2010.
- [25] E. Harvey, V. Kirk, J. Sneyd, and M. Wechselberger. Multiple timescales, mixed mode oscillations and canards in models of intracellular calcium dynamics. *J. Nonlin. Sci.*, 21:639–683, 2011.

- [26] E. Izhikevich. Neural excitability, spiking, and bursting. *International Journal of Bifurcation and Chaos*, 10:1171–1266, 2000.
- [27] E. Izhikevich. *Dynamical Systems in Neuroscience: The Geometry of Excitability and Bursting*. MIT Press, Cambridge, MA, 2006.
- [28] E. Izhikevich. *Dynamical Systems in Neuroscience*. MIT Press, 2007.
- [29] J. Jalics, M. Krupa, and H. Rotstein. Mixed-mode oscillations in a three time-scale system of odes motivated by a neuronal model. *Dynamical Systems*, 25(4):445–482, 2010.
- [30] P. Jasinski, Y. Molkov, N. Shevtsova, J. Smith, and I. Rybak. Sodium and calcium mechanisms of rhythmic bursting in excitatory neural networks of the pre-Bötzinger complex: a computational modelling study. volume 37, pages 212–230. 2013.
- [31] C.K.R.T. Jones. Geometric singular perturbation theory. In *Dynamical systems (Montecatini Terme, 1994)*, pages 44–118. Springer-Verlag, Berlin, New York, 1995.
- [32] T. J. Kaper. An introduction to geometric methods and dynamical systems theory for singular perturbation problems. In *Analyzing Multiscale Phenomena Using Singular Perturbation Methods*, volume 56 of *Proceedings of Symposia in Applied Mathematics*, pages 85–131. American Mathematical Society, Providence, RI, 1999.
- [33] J. Keener and J. Sneyd. *Mathematical Physiology*. Springer, 2008.
- [34] M. Krupa, N. Popović, and N. Kopell. Mixed-mode oscillations in three time-scale systems: A prototypical example. *SIAM J. Appl. Dyn. Syst.*, 7(2):361–420, 2008.
- [35] M. Krupa, A. Vidal, M. Desroches, and F. Clément. Mixed-mode oscillations in a multiple time scale phantom bursting system. *SIAM J. Appl. Dyn. Syst.*, 11:1458–1498, 2012.
- [36] K. Lee, W. Duan, J. Sneyd, and A.E. Herbison. Two slow calcium-activated afterhyperpolarization currents control burst firing dynamics in gonadotropin-releasing hormone neurons. *J. Neurosci.*, 30:6214–6224, 2010.
- [37] J. J.C. LeGallois. Experiences sur le Principe de la Vie, notamment sur celui des mouvemens du coeur, et sur le siege de ce principe. *A Paris: Chez D’Hautel*, 1812.
- [38] T. Lumsden. Observations on the respiratory centres in the cat. *J. Physiol.*, 57:153–160, 1923.
- [39] P. De Maesschalck, E. Kutafina, and N. Popović. Three time-scales in an extended Bonhoeffer-Van der Pol oscillator. *J. Dyn. Diff. Equat.*, 26:955–987, 2014.
- [40] C. Morris and H. Lecar. Voltage oscillations in the barnacle giant muscle fiber. *Biophys. J.*, 35(1):193–213, 1981.

- [41] P. Nan, Y. Wang, V. Kirk, and J. Rubin. Understanding and distinguishing three-time-scale oscillations: case study in a coupled morris-lecar system. *SIAM J. Appl. Dyn. Syst.*, 14:1518–1557, 2015.
- [42] C. Del Negro, J. Hayes, and J. Rekling. Dendritic calcium activity precedes inspiratory bursts in pre-Bötzinger complex neurons. *J. Neurosci.*, 31(3):1017–1022, 2011.
- [43] C. Del Negro, C. Morgado-Valle, and J. Feldman. Respiratory rhythm: an emergent network property? *Neuron*, 34:821–830, 2002.
- [44] C.A. Del Negro, J.A. Hayes, R.W. Pace, B.R. Brush, R. Teruyama, and J.L. Feldman. *Synaptically activated burst-generating conductances may underlie a group-pacemaker mechanism for respiratory rhythm generation in mammals*. In: Gossard J-P, Progress in Brain Research. Amsterdam The Netherlands, 2010.
- [45] C.A. Del Negro, N. Koshiya, R.J. Butera, and J.C. Smith. Persistent sodium current, membrane properties and bursting behavior of pre-Botzinger complex inspiratory neurons in vitro. *J. Neurophysiol.*, 88:2242–2250, 2002.
- [46] C.A. Del Negro, C. Morgado-Valle, J.A. Hayes, D.D. Mackay, R.W. Pace, E.A. Crowder, and J.L. Feldman. Sodium and calcium current-mediated pacemaker neurons and respiratory rhythm generation. *J. Neurosci.*, 25:446–453, 2005.
- [47] C. Park and J. Rubin. Cooperation of intrinsic bursting and calcium oscillations underlying activity patterns of model pre-Bötzinger complex neurons. *J. Comp. Neurosci.*, 34:345–366, 2013.
- [48] N. Popović. Mixed-mode dynamics and the canard phenomenon: Towards a classification. In *Journal of Physics: Conference Series*, volume 138, page 012020. IOP Publishing, 2008.
- [49] L.K. Purvis, J.C. Smith, H. Koizumi, , and R.J. Butera. Intrinsic bursters increase the robustness of rhythm generation in an excitatory network. *J. Neurophysiol*, 97:1515–1526, 2007.
- [50] J. Ramirez and D. Richter. The neuronal mechanisms of respiratory rhythm generation. *Curr. Opin. Neurobiol.*, 6(6):817–825, 1996.
- [51] J. Rekling and J. Feldman. Prebotzinger complex and pacemaker neurons: hypothesized site and kernel for respiratory rhythm generation. *Annual review of physiology*, 60(1):385–405, 1998.
- [52] J. Rinzel. Bursting oscillations in an excitable mebrane model. In *Ordinary and partial differential equations*, volume 1151, pages 304–316. Springer, 1985.
- [53] J. Rinzel. A formal classification of bursting mechanisms in excitable systems. In *In A.M. Gleason, edtiro*, Proceedings of the International Congress of Mathematicians, pages 1578–1594. American Mathematical Society, Providence, RI, 1987.

- [54] J. Rinzel and B. Ermentrout. Analysis of neural excitability and oscillations. pages 251–291, 1998.
- [55] J. Rubin. Bursting induced by excitatory synaptic coupling in non-identical conditional relaxation oscillators or square-wave bursters. *Phys. Rev. E*, 74:021917, 2006.
- [56] J. Rubin, J. Hayes, J. Mendenhall, and C. Del Negro. Calcium-activated nonspecific cation current and synaptic depression promote network-dependent burst oscillations. *Proc. Natl. Acad. Sci. USA*, 106:2939–2944, 2009.
- [57] J. Rubin and D. Terman. Geometric singular perturbation analysis of neuronal dynamics. *Handbook of dynamical systems*, 2:93–146, 2002.
- [58] J. Rubin and D. Terman. Synchronized activity and loss of synchrony among heterogeneous conditional oscillators. *SIAM J. Appl. Dyn. Syst.*, 1:146–174, 2002.
- [59] J. Rubin and M. Wechselberger. Giant squid-hidden canard: the 3d geometry of the hodgkin-huxley model. *Biol. Cybern.*, 97:5–32, 2007.
- [60] I. A. Rybak, R. O’connor, A. Ross, N. A. Shevtsova, S. C. Nuding, L. S. Segers, ..., and I. C. Solomon. Reconfiguration of the pontomedullary respiratory network: A computational modeling study with coordinated in vivo experiments. *J. Neurophysiol.*, 100(4):1770–1799, 2008.
- [61] I.A. Rybak, K. Ptak, N.A. Shevtsova, and D.R. McCrimmon. Sodium currents in neurons from the rostroventrolateral medulla of the rat. *J. Neurophysiol.*, 90:1635–1642, 2003.
- [62] L. S. Segers, S. C. Nuding, T. E. Dick, R. Shannon, D. M. Baekey, I. C. Solomon, K.F. Morris, and B. G. Lindsey. Functional connectivity in the pontomedullary respiratory network. *J. Neurophysiol.*, 100(4):1749–1769, 2008.
- [63] X. Shao and J. Feldman. Respiratory rhythm generation and synaptic inhibition of expiratory neurons in pre-botzinger complex: differential roles of glycinergic and gabaergic neural transmission. *J. Neurophysiol.*, 77:1853–1860, 1997.
- [64] M. Sheroziya, O. von Bohlen, K. Unsicker, and A.V. Egorov. Spontaneous bursting activity in the developing entorhinal cortex. *J. Neurosci.*, 29:12131–12144, 2009.
- [65] J. Smith, H. Ellenberger, K. Ballanyi, D. Richter, and J. Feldman. Pre-botzinger complex: a brainstem region that may generate respiratory rhythm in mammals. *Science*, 254:726–729, 1991.
- [66] J.C. Smith, A.P. Abdala, H. Koizumi, I.A. Rybak, and J.F. Paton. Spatial and functional architecture of the mammalian brain stem respiratory network: a hierarchy of three oscillatory mechanisms. *J. Neurophysiol.*, 98:3370–3387, 2007.
- [67] D. Somers and N. Kopell. Rapid synchronization through fast threshold modulation. *Biol. Cybern.*, 68:393–407, 1993.

- [68] S. Tazerart, J. Viemari, P. Darbon, L. Vinay, and F. Brocard. Contribution of persistent sodium current to locomotor pattern generation in neonatal rats. *J. Neurophysiol.*, 98(2):613, 2007.
- [69] S. Tazerart, L. Vinay, and F. Brocard. The persistent sodium current generates pacemaker activities in the central pattern generator for locomotion and regulates the locomotor rhythm. *J. Neurosci.*, 28:8577–8589, 2008.
- [70] D. Terman, N. Kopell, and A. Bose. Dynamics of two mutually coupled inhibitory neurons. *Physica D*, 117:241–275, 1998.
- [71] D. Terman and D. Wang. Global competition and local cooperations in a network of neural oscillators. *Physica D*, 81:148–176, 1995.
- [72] M. Thoby-Brisson and J.M. Ramirez. Identification of two types of inspiratory pacemaker neurons in the isolated respiratory neural network of mice. *J. Neurophysiol.*, 86:104–112, 2001.
- [73] N. Toporikova and R.J. Butera. Two types of independent bursting mechanisms in inspiratory neurons: an integrative model. *J. Comp. Neurosci.*, 30(3):515–528, 2011.
- [74] K. Tsumoto, H. Kitajima, T. Yoshinaga, K. Aihara, and H. Kawakami. Bifucations in Morris-Lecar model. *Neurocomputing*, 69:293–316, 2006.
- [75] K. Tsuruyama, C.-F. Hsiao, and S. Chandler. Participation of a persistent sodium current and calcium-activated nonspecific cationic current to burst generation in trigeminal principal sensory neurons. *J. Neurophysiol.*, 110(8):1903–1914, 2013.
- [76] A. Vidal and F. Clément. A dynamical model for the control of the gonadotrophin-releasing hormone neurosecretory system. *J. Neuroendocrinology*, 22(12):1251–1266, 2010.
- [77] T. Vo, R. Bertram, and M. Wechselberger. Multiple geometric viewpoints of mixed mode dynamics associated with pseudo-plateau bursting. *SIAM J. Appl. Dyn. Syst.*, 12(2):789–830, 2013.
- [78] T. Vo, J. Tabak, R. Bertram, and M. Wechselberger. A geometric understanding of how fast activating potassium channels promote bursting in pituitary cells. *J. Comp. Neurosci.*, 36(2):259–278, 2014.
- [79] D. Wang, S. Grillner, and P. Wallen. Effects of flufenamic acid on fictive locomotion, plateau potentials, calcium channels and NMDA receptors in the lamprey spinal cord. *Neuropharmacology*, 51:1038–1046, 2006.
- [80] Y. Wang and J. Rubin. Multiple time scale mixed bursting dynamics in a respiratory neuron model. *J. Comp. Neurosci.*, pages 1–24, 2016.
- [81] M. Wechselberger. A propos de canards (apropos canards). *Trans. Am. Math. Soc.*, 364:3289–3309, 2012.

- [82] G. Zhong, M. Masino, and R. Harris-Warrick. Persistent sodium currents participate in fictive locomotion generation in neonatal mouse spinal cord. *J. Neurosci.*, 27(17):4507–4518, 2007.
- [83] L. Ziskind-Conhaim, L. Wu, and E.P. Wiesner. Persistent sodium current contributes to induced voltage oscillations in locomotor-related hb9 interneurons in the mouse spinal cord. *J. Neurophysiol.*, 100(4):2254–2264, 2008.